The "Hidden-Order" Phase Transition of URu_2Si_2

Investigated by Angle-Resolved Photoelectron Spectroscopy

Dissertation

zur Erlangung des wissenschaftlichen Doktorgrades
der Julius-Maximilians-Universität Würzburg

vorgelegt von

Florin Loredan Boariu
aus Baia Mare, Rumänien

Würzburg 2014

Eingereicht am: 27. Januar 2014
bei der Fakultät für Physik und Astronomie

Gutachter der Dissertation:
Prof. Dr. Friedrich Theodor Reinert
Prof. Dr. Matthias Bode

Prüfer im Promotionskolloquium:
Vorsitzender: Prof. Dr. Ronny Thomale
Prof. Dr. Friedrich Theodor Reinert
Prof. Dr. Matthias Bode
Prof. Dr. Fakher Assaad

Tag des Promotionskolloquiums: 6. Mai 2014

Doktorurkunde ausgehändigt am: .....

Contents

Abstract

In 1985, an enigmatic second order phase transition was discovered in the actinide compound URu_2Si_2. Evading a microscopic description for nearly three decades in spite of numerous experimental and theoretical attempts, the name "hidden order transition" was adopted for the effect.

Specific heat, resistivity and Hall effect measurements indicate that a gap encompassing 40% of the Fermi surface occurs at the transition temperature of $T_{\mathrm{HO}} = 17.5$ K. Inelastic neutron scattering experiments demonstrate gapped magnetic excitations at commensurate and incommensurate lattice points, but the magnetic moment in the HO state is too small to account for the large entropy loss detected. Approaches to describe the phase transition as conventional spin or charge density waves have failed. The question of whether localized or itinerant Uranium $5f$ moments are responsible was answered in 2008, when a Fermi surface reconstruction involving heavy, coherent quasi-particles was observed across the HO transition. In spite of a lattice coherence temperature of $T \approx 75$ K inferred from electrical transport, interpretations of far infrared optical data associate the new order with the onset of lattice coherence below 20 K. Some of them propose a type of an "arrested" Kondo effect developing at the transition temperature.

In this thesis, the onset of lattice coherence is demonstrated already at temperatures as high as 70 K using high-resolution angle-resolved photoelectron spectroscopy (ARPES). Previously undetected heavy quasi-particles, existing already above T_{HO} as elements of a coherent lattice, are shown to hybridize with heavy electron bands and participate in the Fermi surface reconstruction at 17.5 K. These results pave the way for a detailed understanding of the gaps, symmetries and entropy loss of the HO elaborated in an associated research project, outlined in the final part of this manuscript.

Chapter 1

Introduction

1.1 Motivation

Properties of physical systems often amount to more than the sum of their individual constituents. Complex behavior evolves suddenly from the competition between simple interactions and properties, well understood in their individual form. Research fields dedicated to *"emergent phenomena"* seek to describe how [80]. This kind of behavior is often observed in the form of phase transitions, which are characterized by the abrupt change in macroscopic properties of a system in spite of smooth, gradual changing of an external control parameter. Phase transitions occur within a broad range of energies, from the GeV-scale Higgs mechanism to meV interactions between electrons in molecules and solids, and may result in exotic behavior such as superconductivity.

One particular element offering the opportunity to study phase transitions and emergent phenomena is Uranium. Although formally radioactive, in its depleted form it is safe to use in a standard laboratory if the usual precautions for working with chemically poisonous heavy metals are taken. The properties of Uranium compounds, such as the rare-earth metal URu_2Si_2 studied here, are derived from the open Uranium $5f$ shell. A number of energy quantities influencing the electronic structure are on the same scale (exchange interaction, $5f$ bandwidth, spin-orbit interaction, Coulomb interactions [69]), placing U-based materials at the border between itinerant and localized $5f$ systems.

In URu_2Si_2, heat capacity, magnetization, and electrical transport up to very high magnetic fields help to establish a rich and complex phase diagram, suggesting the existence of a quantum critical point. The subtle interplay between microscopic interactions around an anomaly at $T_{\mathrm{HO}} = 17.5$ K still poses a riddle to the scientific community even after 30 years of intense research. The name "hidden-order" was subsequently assigned to this anomaly because the order parameter of the 2^{nd} order phase transition associated with it still remains unknown.

1.2 History of the "Hidden-Order" Transition

1.2.1 The URu_2Si_2 Crystal

URu_2Si_2 exists in a body-centered tetragonal lattice. Literature states the microscopic dimensions of the single-crystals [5, 6, 11] as $a = b = 4.12$ Å for the base plane edge

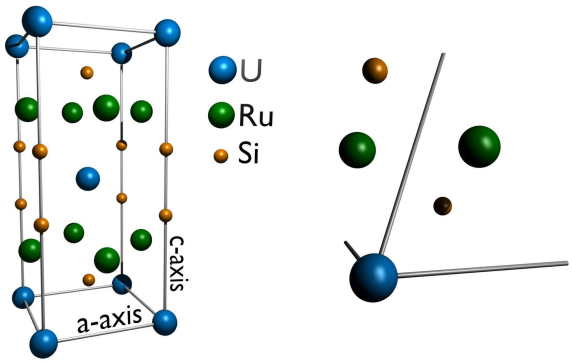

Figure 1.1: **Schematic representation of URu_2Si_2 crystal.** Left image shows a cartoon of the body-centered tetragonal lattice within the elementary cell boundaries of the simple-tetragonal lattice. Right image shows the basis with lattice vector of a elementary cell and the lattice vectors of a body-centered tetragonal lattice.

lengths, and $c = 9.58$ Å as the height of the tetragonal cell, double the size of a primitive elementary cell. Cartoons of the crystal stucture are displayed in figure 1.1.

1.2.2 Priorities in the Research History of URu_2Si_2

In the following, the experimental scientific history of URu_2Si_2 will be recalled. There have existed several phases during the past decades of research, each with the emphasis on a particular set of aspects of the "hidden-order" phase transition. To attempt a pedagogic approach, these aspects will be grouped together into "generations of research". Each generation will be a phase in the experimental URu_2Si_2 investigations determined by the prevalent ideas, and, loosely, by the time at which the corresponding experiments were conducted.

However, this separation is not to be taken very strictly, being just a personal preference of dealing with the vast amount of literature available. Differing methods may prove valid or more expedient for other purposes than this thesis. In this sense, the following partitioning will be used in what follows:

1st generation: Discovery of HO, supporting thermodynamic and electrical transport measurements surrounding it.

2nd generation: The low-pressure HO and high-pressure large-moment antiferromagnetic (LMAF) order as two spatially separated phases, and their relation to the momentum exchange vectors Q_0 and Q_1.

3rd generation: HO in *"adiabatic continuity"* [47] with LMAF, as a single thermodynamic phase with two intrinsic order parameters.

Momentum-resolved investigations of the gaps and symmetries of the HO phase may be interpreted as the passage to a 4^{th} generation, as briefly outlined in section 4.

1.2.3 Discovery of the "Hidden-Order"

Thermodynamic and transport anomalies in URu_2Si_2 First Palstra, then Maple and Schlabitz published [5, 6, 9] with their co-workers more than 28 years ago two anomalies in the transport properties of URu_2Si_2. One was a large Λ-shaped peak around $T_{HO} = 17.5$ K in the specific heat (figure 1.2), associated with a jump in the resistivity of

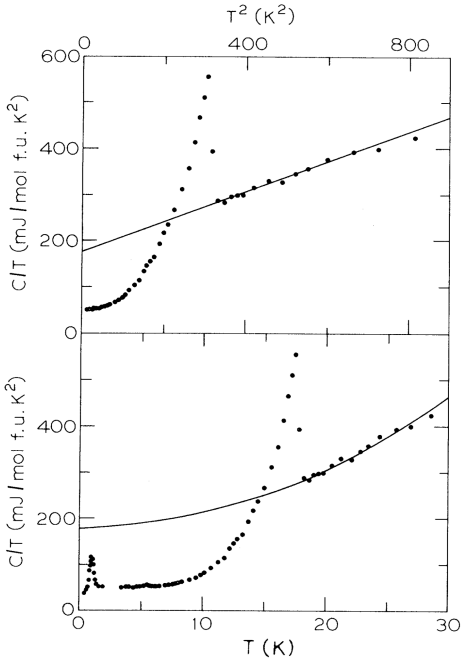

Figure 1.2: **Specific heat of URu_2Si_2 against temperature.** Specific heat is plotted against T^2 (above) and T (below), showing a Λ-shaped peak attributed to a 2nd order phase transition, the "hidden-order", at 17.5 K. The transition to a superconducting state occurs at 1 K. The difference in the extrapolations of the Sommerfeld coefficient above and below 17.5 K is an indication of a gap spanning 40% of the Fermi surface. *Image from reference [5].*

the material (figure 1.3). Because even today the order parameter behind what turns out to be a 2nd-order phase transition still remains unknown, it eventually became referenced in the literature as the "hidden-order" (HO). The other anomaly was a sudden drop in resistivity close to 1 K, corresponding to a superconducting (SC) phase.

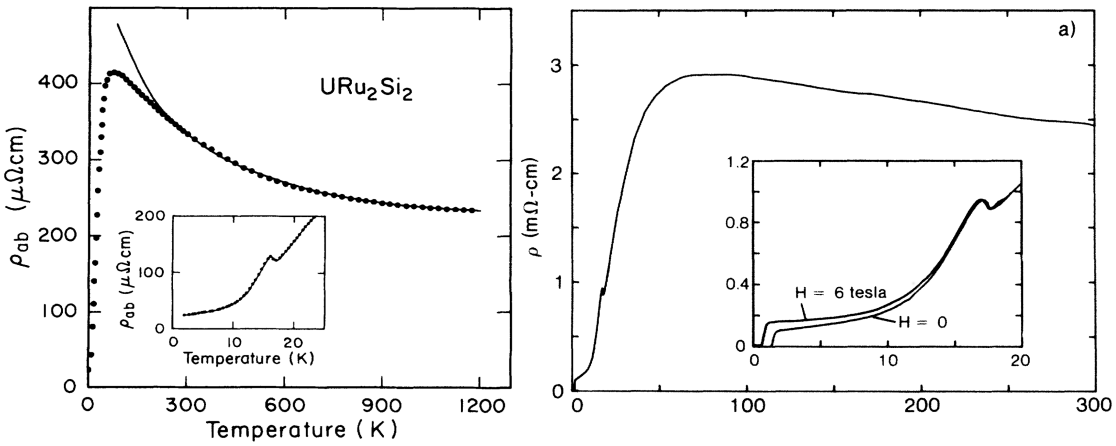

Figure 1.3: **Temperature-dependent resistivity in URu_2Si_2.** At high temperatures, the resitivity rises as temperature decreases, showing *"Kondo-like"* [8, 17] behavior. Around 75 K, a peak associated with coherent behavior of magnetic impurities is visible, at 17.5 K the "hidden-order" anomaly, and below 2 K a superconducting transition. *Panels from references citeschoenes87 (left) and [6] (right).*

Details of the SC phase Concerning the nature of the superconducting phase at 1 K, agreement prevailed from the beginning [5, 6, 9]. The transition temperature T_{SC} is less stable than for the HO order, varying between 0.8 K and 1.5 K throughout the literature, in dependence on sample quality. Neutron scattering experiments show that signatures of the HO transition (momentum exchange vectors Q_0 and Q_1 discussed later) do not change across the transition to the SC state, suggesting a microscopic co-existence with HO [11, 18].

Details of the HO phase Opinions about the HO phase differed: Palstra, Maple and others [5, 6, 11, 17, 22] proposed a weak, antiferromagnetic (AF) transition, suggesting the formation of static charge or spin density waves (CDW / SDW). On the other hand, Schlabitz *et al.* [9] saw evidence for interactions between small, local AF moments of the uranium f-electrons.

Subsequently all early interpretations would be rendered obsolete: neither long-range magnetic interactions nor electronic lattice modulation were reported in modern STM experiments [59, 63], ruling out the formation of conventional density waves. The localized-itinerant duality of the experimental data would prevail through more than two decades of research, posing a major challenge in the theoretical formulation of the transition.

At high temperatures the anisotropic resistivity of URu_2Si_2 rises as temperature decreases (figure 1.3). It starts deviating from power law below $T \approx 150$ K with a maximum around $T \approx 75$ K indicating the onset of coherence [5, 6, 8, 17, 24]. In this context the term *"Kondo-like"* was used to describe the single magnetic moments of Uranium f electrons. In the same range, magnetic susceptibility shows a gradual deviation from the $1/T$ Curie-Weiss law, forming a large peak at 75 K, and a smaller anomaly around the HO transition temperature of 17.5 K (figure 1.4).

Across the transition temperature specific heat and resistivity show sharp peaks (figures 1.2 and 1.3) followed by a steep decrease. Fitting the thermodynamic data to a mean-field shape of the form $C_\nu(T) \propto \exp(-\Delta/k_B T)$, yields the formation of a gap $\Delta = 11$ meV, also confirmed by resistivity measurements [6, 12, 22]. Consistently with transport and thermodynamical data, a drastic increase of the Hall effect (figure 1.4) indicates that a large number of carriers is disappearing. As quantitative estimates, 40% of the Fermi surface are named in early publications [6, 13, 17], extending to 55% or even up to 90% during following generations of thermal transport and Shubnikov–de Haas experiments [40, 62].

A large-moment antiferromagnetic phase connected to HO Magnetic moments appear to be strongly anisotropic, Ising-like, oriented along the c axis. But at less than $0.04\mu_B$ per site, they are too small to account for the large entropy change in the HO phase [8, 11, 65]. At hydrostatic pressures above 0.5 GPa, magnetic moments one order of magnitude larger suggest the transition to a large-moment antiferromagnetic (LMAF) phase. Together with the dependency of the Fermi surface gap of applied pressure [12], a connection between the LMAF and the HO phase is suggested.

1st generation in a nutshell Interconnections between the three phases emerging from thermodynamic and transport data at low temperatures—HO, LMAF and SC—are apparent, but the exact nature of those remains elusive. First scenarii proposing

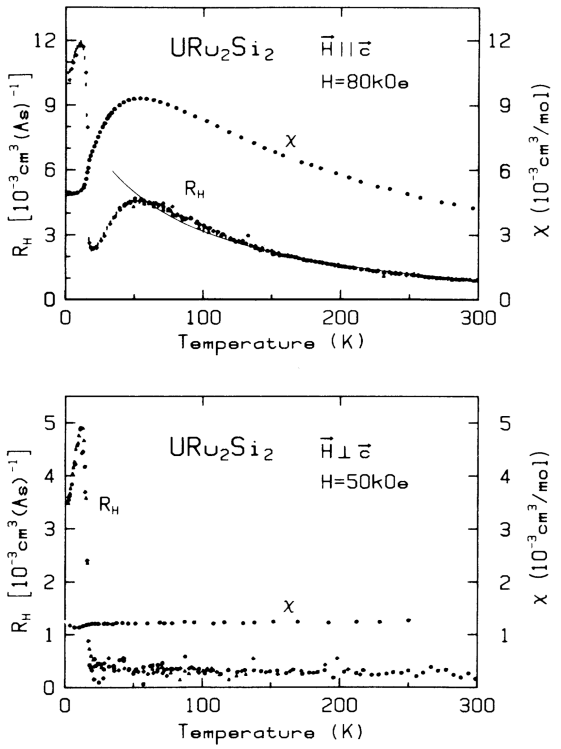

Figure 1.4: **Hall effect in URu_2Si_2 parallel and perpendicular to the c axis.** The data suggests a massive reorganization of the Fermi surface, during which large parts of the carriers become gapped. *Image from reference [13].*

conventional magnetic order / disorder transitions for the HO and LMAF phases involve the formation of spin or charge density waves. However, they will increasingly turn out as too optimistic with experiments to follow.

1.2.4 The HO as a Small-Moment Antiferromagnetic Order

The HO/LMAF connection was predominantly inferred during the 2nd generation from two types of experiments. First, using inelastic neutron scattering, links and differences between the magnetic excitations in URu_2Si_2 in the HO, LMAF, and the paramagnetic state were investigated [10, 11, 18, 19, 48, 53]. Then methods like nuclear magnetic resonance (NMR) and muon spin resonance (μSR) provided differentiated information about the bulk of the crystal and the nature of the separation between HO and LMAF [16, 23, 34, 35].

Antiferromagnetic scattering and the momentum exchange vectors The antiferromagnetic stacking along the c crystal direction is longitudinal, rather than transversal, as would be expected for low energy CDW / SDW excitation [11, 18, 19]. Small magnetic moments in the HO phase led to the assumption of conventional density waves as the ordering mechanism. In subsequent experiments, the moments turned out to be strongly dependent on the sample quality, diminishing with increased purity. Recently it is commonly accepted that the HO magnetic moment is in fact of extrinsic origin, and not an intrinsic property of the transition [34, 43, 51].

An important contribution of neutron-scattering experiments is the identification of two momentum exchange vectors, throughout URu_2Si_2 literature quoted as Q_0 and

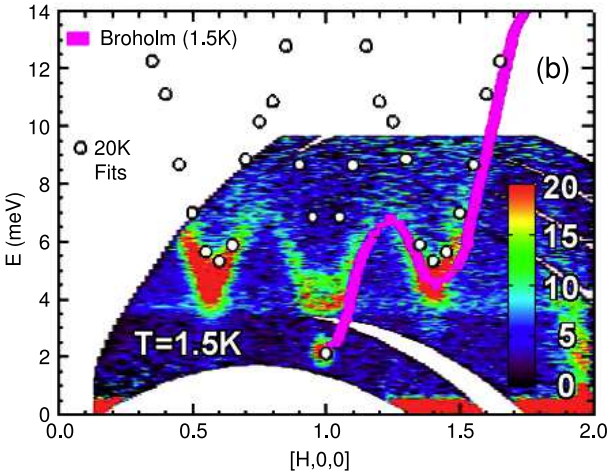

Figure 1.5: **Magnetic excitations in the HO phase of URu_2Si_2.** The exciations at commensurate momentum exchange vectors Q_0 and incommensurate Q_1 are gapped below 2, respectively 4.5 meV. *Image from reference [69], showing data from [11, 53].*

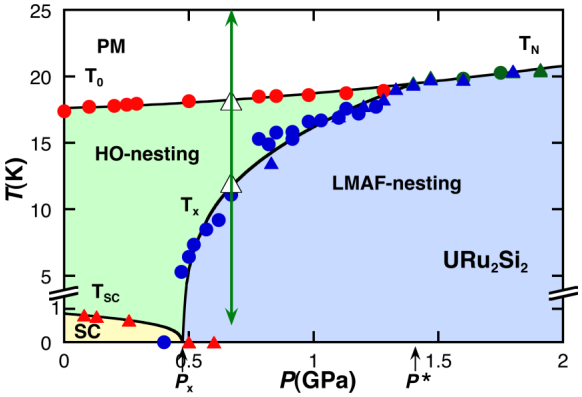

Figure 1.6: **Pressure-temperature phase diagram of URu_2Si_2.** The diagram was first proposed by Amitsuka*et al.* [43], and shows the SC phase emerging from HO, but not from LMAF. T-dependent studies at high pressure, performed along the green arrow, investigate the LMAF/HO phase boundary. *Image from [50].*

Q_1. $Q_0 = (1, 0, 0)$, equivalent to $(0, 0, 1)$, connects neighboring Brillouin zones, i.e. the alternating Γ and Z points. $Q_1 = (1 \pm 0.4, 0, 0)$, equivalent to $(1, \pm 0.4, 0)$, connects incommensurate points within the plane.

The excitations in the HO phase are depicted in figure 1.5, based on experiments from references [19, 48, 53]. At both Q_0 and Q_1 damped magnetic excitation become sharp below 17.5 K, and are gapped at energies below 2 meV, respectively 4.5 meV. Although they appear in clear correlation with the HO and LMAF phases, it was long unclear whether and how they are responsible for the reordering, i.e. how they relate to the order parameter: *"Are they the elementary excitations that cause this spin gapping?"* [69]. Subsequently, Q_0 would be proposed as signature of HO, with *"persistence of nesting"* [50] throughout both phases, but with an inelastic component only in HO. However, momentum-resolved evidence for their implication in the ordered state has been offered only very recently, in the context of this thesis and closely related research [76].

Spatial co-existence of LMAF and HO μSR and NMR experiments suggest the coexistence of LMAF and HO in a pressure-dependent percolation relation [16, 34, 35]. Existing simultaneously below the transition temperature as two spatially separated phases, the former would grow at the expense of the latter with pressure. The p-T phase diagram was proposed as in figure 1.6 [34, 50]. A distinct property of the HO phase is that it, unlike LMAF, also coexists with the SC phase at lower temperature [43].

2nd generation in a nutshell Although the existence of the Q_0 and Q_1 spin excitations is discovered and fully documented in a momentum-integrated manner, its implication is still not fully understood: Is there a nesting of the Fermi surface involved? What is the link between the excitations and the energy gaps? How do they relate to the HO ordering parameter? In other words, momentum-resolved information of Q_0 and Q_1 and how they relate to the reconstruction and gapping of the Fermi surface across the HO transition is sparse.

1.2.5 Adiabatic Continuity Between HO and Large-Moment AF Phase

The 3rd generation of URu_2Si_2 research has its focus on understanding the Fermi surface and electronic structure changes relevant for the HO transition. Roughly, experiments may be divided in two types: strongly bulk-sensitive methods, like transport, thermodynamics, Shubnikov–de Haas (SdH), de Haas–van Alphen (dHvA); and surface-sensitive methods, like scanning tunneling microscopy / spectroscopy (STM / STS), and angle-resolved photoelectron spectroscopy (ARPES). The former trade in the momentum resolution for the advantage of being able to reliably poll the bulk of the crystal. The latter promises to provide microscopic data of the highly anisotropic material, spatially and / or momentum-resolved to varying degrees, provided that unwanted surface effects can be properly dealt with.

Momentum-resolved experiments A vast amount of essential ground laying work was performed by Denlinger and coworkers, published as references [29, 32]. The idea of a coherent lattice in systems like URu_2Si_2 was systematically investigated in the normal (paramagnetic) state. The k-space map to be presented in section 1.3.3 in its particular 2D representation was inspired by [32]. Electronic structure and Fermi surface calculations used throughout recent URu_2Si_2 literature, as well as essential experimental aids, like the inner potential of the crystal were, too, extracted from this source.

First modern high-resolution ARPES of the PM $\leftrightarrow$ HO transition was performed at Würzburg and published as reference [57]. Results will be reviewed in more detail in section 2.3.2. Here it suffices to state the main finding: the direct observation of a Fermi surface instability close to the Γ point as a band with effective mass $m/m_e > 20$, crossing the Fermi level at the transition temperature. Evidencing for the first time the direct participation of itinerant, heavy quasi-particles in the HO phase transition, the work was followed by a cascade of other momentum resolved ARPES and STM/STS experiments.

Laser ARPES close to Z confirmed the FS instability at another high-symmetry point, visible as a heavy "M"-shaped dispersion appearing during the transition [64, 74]. Unlike Γ, at Z the heavy dispersion appears not to shift, but simply vanishes upon entering the PM state, indicating the three-dimensional electronic structure of the material. Such behavior would be expected, for example, if the lattice symmetry changed from body-centered to simple tetragonal (ST) during the HO transition. This would result in folding of the spectra at Γ and Z.

The ARPES picture is essentially confirmed by STS using quasi-particle interference: a heavy dispersion is splitting at E_F and hybridizing with a light hole-like band [63]. A particularity of this experimental technique is that it probes the lattice with full momentum resolution along $k_{\parallel}$, but only momentum-integrated along $k_{\perp}$. Spatially resolved STM data showed lack of an electronic superstructure, directly excluding conventional

SDWs or CDWs from the probable mechanisms behind the HO transition [59, 63]. This is a conclusion also supported by optical transport [68].

In consequence, a coherent picture of the changes induced by the HO is still not available. However, direct evidence of itinerant, heavy quasi-particles participating in a Fermi surface reconstruction is delivered.

Momentum-integrated experiments Because no clean surface is needed, predominantly bulk-sensitive methods usually don't have to be performed in ultra-high vacuum. This loosens the experimental constrains, such that additional parameters like pressure and external magnetic fields can be covered. The transition between the HO and LMAF phase becomes more easily explorable.

Efforts emerged initially independently of the momentum-resolved experiments, later to evolve in tandem with those. Transport and SdH data suggest that the HO is ultimately destroyed at a field strength of 35 Tesla, being followed by a cascade of phase transitions in higher magnetic fields [55, 65].

In the paramagnetic state, Kondo-like behavior and the onset of lattice coherence, around $T \approx 100$ K can already be inferred from 1st and 2nd generation data [13, 14, 17, 24]. This was confirmed in various optical conductivity experiments, aswell as by STM/STS [14, 15, 59, 68, 73]. A novelty is the formation of a hybridization gap of size 10-12 meV already in the PM phase, starting at temperatures below 30 K. Topographic STM scans even show a spatial correlation between the gap and Kondo lattice elements in the vicinity of U atoms. However, most interpretations evolve around the formation of an only partially coherent lattice with *"pseudo-gaps"* in the PM phase, with the full coherence believed to set in only below the HO transition temperature [73].

In the HO phase, several gaps were detected by optical spectroscopy [72]. Some of them had been previously discovered by inelastic neutron scattering, others are new. In total, the following gaps have been identified:

- a 3.2 meV gap (associated with Q_1 INS data, there of the size 4-4.5 meV),
- a 2 meV gap (associated with Q_0 from INS),
- another 2.7 meV gap measured along the c axis of the crystal, not detected by INS.

With the 10 meV gap below 30 K from optical transport, this gives a total of 4 gaps indirectly measured or predicted. They appear within 5 relevant Fermi sheets with various masses ($10 < m/m_e < 70$). Of these, 4 were indirectly measured by SdH and dHvA [27, 62]:

- α, with a band mass $m/m_e \approx 12.4$,
- β, with a band mass $m/m_e \approx 23.8$, corresponding to an in-plane 4-pocket sheet,
- γ, band masses $m/me \approx 10$
- η, with $m/m_e \approx 20.5$, previously postulated by band calculations [51].

These can already account for more than 55% of the Sommerfeld coefficient. Another branch, ν, was postulated with an effective mass $m/m_e > 70$ but not yet observed experimentally [51, 62].

Fermi surface similarity between HO and LMAF The legacy of 3rd generation momentum-integrated methods is the reinterpretation of the HO and LMAF phases based on the structure of their Fermi surfaces. NMR and μSR experiments of the 2nd generation suggested two distinct, spatially-separated phases in a pressure-dependent relation [23, 34, 35]. But the smooth evolution of the SdH oscillation frequencies from the HO to the LMAF phase implies that the Fermi surface does not change significantly, and in any case not abruptly [27, 38, 47, 62]. A similarity between the two phases is therefore suggested *"strongly"* [62]. The state below T_{HO} is thus reinterpreted: instead of being separated by a 1st-order transition, HO and LMAF form a single thermodynamic phase with two intrinsic order parameters.[1] The term *"adiabatic continuity"* was coined to describe this duality [47]. The order parameter common to both phases is related to a strongly anisotropic, Ising-like magnetic moment [65]. In this context Q_0 was proposed as the essential HO / LMAF ordering vector [62], implying symmetry change of the electronic structure from body-centered to simple tetragonal below 17.5 K.

Focus of this work The thermodynamic interpretation of the HO and LMAF as a single phase, developing in correlation with a coherent Kondo lattice in URu_2Si_2, defines the scientific context of this thesis. At this point, significant details about the development of the Kondo lattice in URu_2Si_2 are still unclear [68, 73]: When does the coherence set in? How does it interact with the HO? None of the gaps of the Fermi surface has actually been identified by momentum-resolved methods, the loss of entropy is not understood, symmetries of the HO still remain without a precise identification in k-space. In particular, the interplay between Q_0 and Q_1, and between them both and the HO phase, remains elusive. Although Q_0 has been repeatedly proposed as the relevant symmetry vector behind the HO / LMAF order, momentum-resolved data to back up the claim, e.g. in form of Fermi surface sheets suitable for nesting, are not available.

The main contribution of this thesis will be momentum-resolved spectroscopic evidence that the formation of the Kondo lattice is not related to the HO transition and the subsequent gapping of the Fermi surface. Instead, the HO state evolves on a coherent lattice already fully developed at much higher temperatures. A simple phenomenological model will also be offered to explain the reorganization of the electronic structure and Fermi surface of URu_2Si_2 at several high-symmetry points. Insight about the interaction between the pre-existent coherent lattice and the "hidden" mechanisms behind the transition at 17.5 K will lay ground for subsequent, closely related work on momentum-resolved measurement of gaps and symmetries of the HO. The latter topic was pursued by C. Bareille in his PhD thesis [75] and will be briefly outlined here in section 4.

1.3 Experimental Considerations

1.3.1 Introduction to Angle-Resolved Photoelectron Spectroscopy

What is ARPES When photons are directed towards a material, electrons are emitted from the material into vacuum. This is known as the *photoelectric effect*. Physical quantities of the electron, like its kinetic energy and the angle between its momentum direction

[1] Instead of "two order parameters", the equivalent description of a single "multi-component" order parameter is also found in literature.

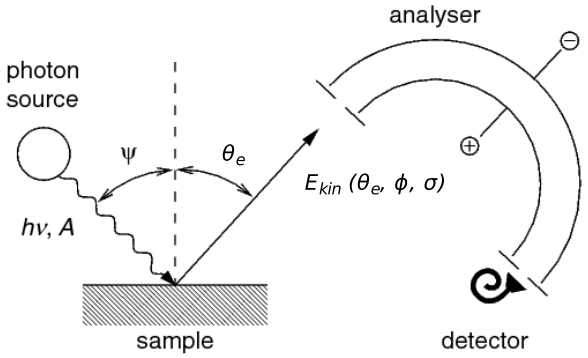

Figure 1.7: **Sketch of a typical experimental setup for ARPES.** A photon with energy $\hbar\omega$ excites an electron inside a solid. The electron is detected with the kinetic energy E_{kin} at an angle θ_e, which may permit partial or full reconstruction of the electronic structure of the crystal. *Image source: Prof. Dr Friedrich Reinert, EP7, Uni Würzburg.*

and the surface normal of the sample, can be detected. Together with experimental parameters like the energy and incident angle of the excitation beam, information about the electronic structure of the material can be extracted. This experimental technique is known as Angle-Resolved Photo-Electron Spectroscopy (ARPES).

A successful phenomenological approach for describing the escape of an electron into vacuum is the *three step model*. It divides the process of photoemission in three distinct steps: (**i**) photoexcitation of the electron, (**ii**) transport to the surface, (**iii**) penetration through the surface. In step (**i**), the ejected electron can be related to the spectral function, carrying full information about quasi-particle physics. Photoelectron spectroscopy (PES), in particular angle-resolved PES (ARPES), is thus a very good tool for momentum-resolved investigations of the low-energy physics and quantum phase transitions in heavy fermion systems. Step (**ii**) turns out to be a strong limiting factor. The short mean free path of the excited electron through the bulk of a crystal means that photoemission is usually only possible for the first very few monolayers close to a microscopically clean surface. Step (**iii**) is a process associated with the loss of a material dependent energy quantity $\phi \approx 5$ eV, called the *work function*.

Energy considerations Formally, the photoemission process is viewed as a transition between an initial state within the solid, with energy E_{init}, and a final state in the unoccupied region, with energy E_{final} with respect to the Fermi level $E_F = 0$, defined as:

$$E_{\text{final}} = E_{\text{init}} + \hbar\omega \tag{1.1}$$

The transition is facilitated by the radiation field of the excitation beam, and is thus subject to optical transition restrictions and Fermi's golden rule. Corresponding matrix elements will strongly influence the signal intensity in the experimental data. The kinetic energy of electrons is related to the excitation energy by $E_{\text{kin}} = \hbar\omega - \phi - |E_B|$, with E_B as the binding energy of the electron in the crystal, as summarized in figure 1.8. It is related to the final-state energy through $E_{\text{final}} = E_{\text{kin}} + \phi$. Thus, E_{final} represents the same physical quantity as E_{kin}, only with respect to the vacuum level E_{vac} instead of E_F. The binding energy E_B is specified with respect to the Fermi level. In this work, differing from usual convention, the binding energy has the same sign as the potential energy: it grows increasingly negative towards stronger bound states, is 0 at E_F, and becomes positive above the Fermi level.

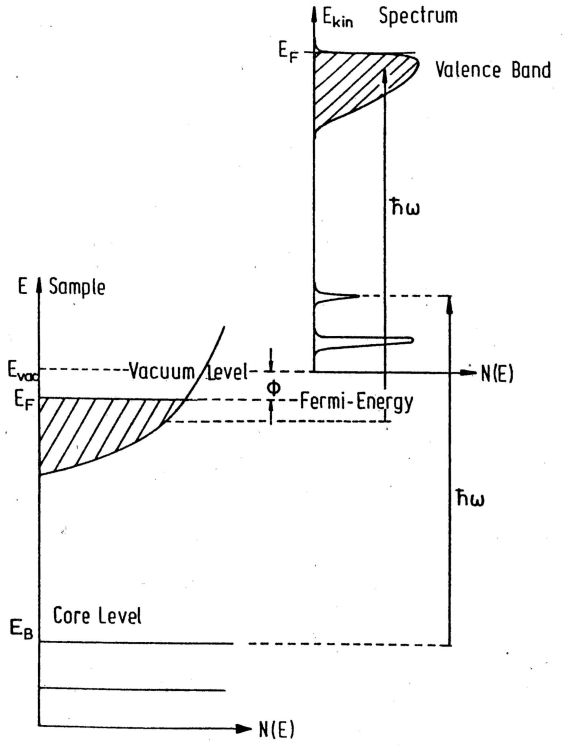

Figure 1.8: **Probing of the electronic density of states in a solid using photoelectron spectroscopy.** An electron bound at energy E_B with respect to the Fermi level $E_F = 0$ is excited by a photon with energy $\hbar\omega$. It is detected with kinetic energy $E_{\text{kin}} = \hbar\omega - \phi - |E_B|$ compared to the vacuum level E_{vac}. *Image source: Prof. Dr S. Hüfner, reference [37].*

The three-dimensional electronic structure

The free electron model For knowledge of the 3D band structure, information about the dispersion relation $E(\mathbf{k})$ is wanted. To this end, the *free electron model* serves as an essential tool. The final state of the electron is assumed to be a free electron valence band, bound at energy $E_0 < 0$ relative to the Fermi level, or at $-V_0 = -(|E_0| + \phi)$ with respect to the vacuum level:

$$E_{\text{final}} = E_{\text{kin}} + \phi = \frac{\hbar^2}{2m}(\mathbf{k})^2 - |E_0| \tag{1.2}$$

$$\Leftrightarrow E_{\text{kin}} = \frac{\hbar^2}{2m}(\mathbf{k})^2 - V_0 \tag{1.3}$$

Here, $\mathbf{k}$ is the crystal momentum of the electron composed as $\mathbf{k} = (k_x, k_y, k_z)^T$ or $\mathbf{k} = (k_\parallel, k_\perp)^T$, whichever turns out more fit for the calculations to follow. The crystal momentum is subject to Bloch theory, i.e. $\mathbf{k} = \mathbf{k} + \mathbf{G}$ with $\mathbf{G}$ as a reciprocal lattice vector.

Momentum information in-plane with the sample surface The $k_\parallel$ component of the crystal momentum $\mathbf{k}$ is conserved during the ejection process. It is thus directly related to the outside momentum as $\hbar k_\parallel = p_\parallel$. It can be calculated directly from the experimental parameters E_{kin} and θ_e using a free-electron parabola bound at

the vacuum level:

$$E_{\mathrm{kin}} = \frac{p_{\parallel}}{2m}(p)^2 \tag{1.4}$$

$$\Rightarrow k_{\parallel} = p_{\parallel}/\hbar = \sin\theta\sqrt{\frac{2m}{\hbar^2}E_{\mathrm{kin}}} \tag{1.5}$$

In the particular experimental setups used for this thesis (explained later), the in-plane momentum direction is obtained from two angles, θ and φ, defined as follows. The analyser detects electrons ejected within a narrow strip along a particular direction on the sample which is parallel to the direction of the detector slit, called the *detector direction*. The ejection angle of an electron along this strip is θ. The sample surface can be tilted with respect to the optical axis of the detector system in the direction perpendicular to the detector slit by the angle φ, thus obtaining complementary momentum information along the *tilt direction*. The crystal momentum directions corresponding to θ and φ are denoted as $k_x = k_{\parallel,\mathrm{det}}$ and $k_y = k_{\parallel,\mathrm{tilt}}$, respectively.

The momentum of an electron ejected at an arbitrary angle θ from a sample tilted by φ is:

$$|k_{\parallel,\mathrm{det}}| = \sqrt{(2m/\hbar^2)E_{\mathrm{kin}}}\sin\theta \tag{1.6}$$

$$|k_{\parallel,\mathrm{tilt}}| = \sqrt{(2m/\hbar^2)E_{\mathrm{kin}}}\sin\varphi\cos\theta \tag{1.7}$$

For practical reasons related to data processing, the momentum-dependent ARPES data is needed on a regular, rectangular grid. Therefore the reverse transformation $(k_{\parallel,\mathrm{det}}, k_{\parallel,\mathrm{tilt}}) \rightarrow (\theta', \varphi')$ is numerically more useful:

$$\theta' = \arcsin\left(\frac{k_{\parallel,\mathrm{det}}}{\sqrt{2mE_{\mathrm{kin}}/\hbar^2}}\right), \qquad \varphi' = \arcsin\left(\frac{k_{\parallel,\mathrm{tilt}}/\cos\theta'}{\sqrt{2mE_{\mathrm{kin}}/\hbar^2}}\right) \tag{1.8}$$

It provides the angular coordinates (θ', φ'), from which the value of a data point needs to be extracted to be placed onto the rectangular momentum grid point $(k_{\parallel,\mathrm{det}}, k_{\parallel,\mathrm{tilt}})$. Unlike (θ, φ), the coordinates (θ', φ') are not on a rectangular grid. This means in particular that they do *not* represent an exact 1:1 match to data points on the original grid of experimental data. The experimental photoelectron intensity at (θ', φ') is therefore interpolated from the closest neighboring points of the rectangular grid specified by (θ, φ).

Momentum perpendicular to the sample surface The perpendicular momentum component $k_{\perp}$ is not conserved, no direct relation to the outside momentum $p_{\perp}$ is available. Information must therefore be extracted directly from the free electron equation (1.2) above. Rearranging it gives the following for the case of an non-tilted sample with $k_{\parallel,\mathrm{tilt}} = 0$:

$$E_{\mathrm{kin}} + (|E_0| + \phi) = \frac{\hbar^2}{2m}(\mathbf{k})^2 \quad \Leftrightarrow \tag{1.9}$$

$$E_{\mathrm{kin}} \cdot (\sin^2\theta + \cos^2\theta) + V_0 = \frac{\hbar^2}{2m}(k_{\parallel,\mathrm{det}}^2 + k_{\perp}^2). \tag{1.10}$$

With $k_{\parallel,\mathrm{det}}$ quantified as in eq. (1.6), this leaves for $k_{\perp}$:

$$k_{\perp} = \sqrt{\frac{2m}{\hbar^2}(E_{\mathrm{kin}}\cos\theta^2 + V_0)} \tag{1.11}$$

The reverse transformation then is:

$$\hbar\omega' = \frac{\hbar^2}{2m}(k_{\parallel,\mathrm{det}}^2 + k_\perp^2) - V_0 - E_{\mathrm{kin}}, \tag{1.12}$$

$$\theta' = \arcsin\left(\mathrm{sgn}\left(k_{\parallel,\mathrm{det}}\right)\sqrt{\frac{\hbar^2}{2m}k_{\parallel,\mathrm{det}}^2/(E_{\mathrm{kin}} + \hbar'\omega)}\right), \tag{1.13}$$

which now depends on the experimentally available parameters E_{kin} and θ, the excitation beam energy $\hbar\omega$, and the binding energy E_0 (or V_0) of the final state valence band. Generally, the latter is not easily accessible. A discussion of the problem and its possible solutions is performed in literature, for instance chapter 7 of reference [37]. Fortunately for the URu_2Si_2 case, estimations for $V_0 \approx 13$ eV are readily available from band structure calculations fitted to experimental data [29, 49, 67]. Similarly to the $k_\parallel$ case, $(\hbar\omega', \theta')$ represent coordinates on a rectangular angle × energy grid with grid points different from the original experimental data, making an interpolation necessary.

1.3.2 Methods and Setups

Crystal growth The single crystals of average size $2 \times 2 \times 1$ mm^3 were obtained from Dr Pascal Lejay at Institut NEEL, Grenoble. They were synthesized by melting high-purity components under clean argon atmosphere with the correct stochiometry. From the resulting poly-crystalline URu_2Si_2, single-crystals were obtained using a tri-arc furnace equipped with a Czochralsky puller. The samples used for this thesis were then annealed at 900 °C for 10 days under ultra-high vacuum.

Spectroscopy setup Two different data sources were used for this thesis: the laboratory ARPES setup of the EP7 department at the University of Würzburg, and the synchrotron setup at the Berliner Elektronen-Synchrotron II (BESSY) beamline UE112-PGM-1b, dubbed "1^3". At both locations, the experiments were performed with a Gammadata R4000 spectroscopic analyzer. Differing details of the systems are discussed in the following.

The Würzburg system Experiments in Würzburg were performed in two batches: 2007–2008, and post-2008, with slightly differing light sources. For the first batch, a helium (He) discharge lamp monochromatized at the excitation energies $h\nu$ of 21.2 eV, 23.1 , and 40.8 eV (He-I$_\alpha$, He-I$_\beta$ and He-II$_\alpha$, respectively) was used. Relative intensities of these lines are 100 for He-I$_\alpha$ and 6 for both He-I$_\beta$ and He-II$_\alpha$. For all high-resolution experiments, a 0.3 mm straight slit was used in the analyzer. In combination with the He light source, the total energy and angular resolutions were 5.18 meV and 0.3° [41]. For the second batch, a MBS T-1 multi-gas discharge lamp was mounted to the installation. This allowed the use of xenon (Xe) light with a monochromatized energy of $h\nu = 8.4$ eV, resulting into an energy resolution of 4 meV (Appendix B.3). The typical base pressure in the measurement chamber during the experiments was 1×10^{-10} mbar, rising to 8×10^{-10} mbar only during He lamp measurements due to the ion leakage from the light source. The Xe lamp was separated from the measurement chamber by a MgF_2 window, allowing to maintain a good pressure while measuring.

The sample holder allows translation along 3 axes *in situ* by up to several cm. Additionally, rotation in the direction perpendicular to the analyzer slit is possible. The sample was cooled by a two-stage helium continuous flow cryostat. with a passive shielding of the sample. Temperature was regulated between approximately 7 K and room temperature by restricting the liquid helium flow through the cryo system. The capacity of the liquid helium tank is approximately 100 liters, allowing for continuous operation between 16 and 36 hours, depending on the helium flow and pumping settings. During different experimental sessions, different pumping systems were employed. Higher capacity pumps resulted in a more stable temperature at the expense of a larger helium consumption, but without significantly improving the lowest attainable temperature.

Laboratory light sources offer the advantage of high energy stability, effectively placing the Fermi level in all samples at the same energy. To locate the Fermi edge, spectra of poly-crystalline silver (Ag) or copper (Cu) reference samples in electrical and thermal contact with the sample holder were measured at the same temperature as the URu_2Si_2 sample. The angle-resolved scans were then numerically fitted with a Fermi-Dirac distribution (FDD) function. From the fit parameters E_F and k_BT, the exact location and temperature for each URu_2Si_2 scan was determined (Appendix B.1). Using the angle-resolved reference data, the non-uniform lateral intensity distribution of the detection system (channel plate, CCD camera, etc) was determined and corrected.

The 1^3 BESSY beamline Experiments requiring a tunable light source were performed at the BESSY beamline UE112-PGM-1b. Continuous excitation energies from the ultra-violet (UV) into the soft X-Ray regime were available. The polarization could be chosen between linear vertical (LV), horizontal (LH), or circular mode. Particularly for the URu_2Si_2 experiments, the excitation range between 17 and 50 eV was used consistently in LH polarization, with few comparison measurements at selected energies in LV mode.

The sample holder offers translation in three axes, and rotation along two (perpendicular to the analyzer slit, and around the optical axis), allowing the orientation of the sample *in situ* as described in section 1.3.3. The sample is cooled by a He^3 cryostat, shielded by an actively nitrogen-cooled installation. Coupled with an *in-situ* sample heating system, stable temperatures starting from 0.9 K and up to 30 K could be rapidly and reliably reached, as indicated by the thermo-couples attached to the manipulator. Temperature ranges above 30 K were available with delays of few hours owing to the large thermal mass of the sample holding system. Reference [76] estimated a real sample temperature of 3 K for thermocouple readings of 1 K. At 20 K and higher, thermocouples are assumed to represent the sample temperature within an accuracy of less than 1 K. The assumption is based on the exceptional heat shielding of the system and similar experiences with the Würzburg system. In this thesis, temperature labels for 1^3 data reflect the thermocouple readings.

For all experiments at the 1^3 beamline, a 0.2 mm curved slit was used. It was verified that it projects the Fermi level at the same position for all angles with an accuracy better than 0.5 meV. This particular setup results in an effective energy resolution of 3 meV as determined from the full-width at half-maximum (FWHM) of resolution-limited heavy-fermion bands at 1 K. Using line shape fits broadened by resolution and cut off by the FDD, reference [76] estimated the resolution of the same setup to $\Delta E \leq 5$ meV.

Reference spectra were difficult to obtain owing to the arduously reproducible translation properties of the sample holder. For this reason, series of several measurements on poly-crystalline gold (Au), evaporated on the sample holder in vacuum, were used to determine the work function of the system of $\phi = 4.3523 \pm 0.0015$ eV. The location of the Fermi level in reference spectra could be determined with a precision of $\Delta E_{\text{Fermi}} \approx 1.5$ meV across various samples.

The Fermi level of the samples was obtained from the photon energy used for the scans subtracting work function (section 1.3.1). This Fermi level location was subject to variations of up to 3 meV when excitation energy was changed, and occasionally to slow drifting when it was increased step-wise. As a reason, misconfiguration of the beamline hardware is suspected. To compensate, the Fermi level offset was manually adjusted in the data by observing the Fermi edge of the foremost EDC, where intensity at E_F could be reliably demonstrated (see spectra from section 3.4). For lateral intensity normalization, the higher-order intensity always present above E_F in beamline spectra was used.

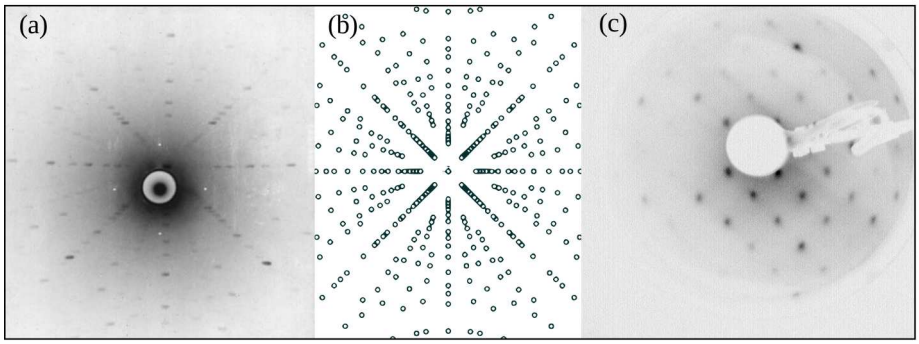

Figure 1.9: **Surface of URu_2Si_2 after cleaving.** (a) Laue and (c) LEED images of an URu_2Si_2 sample in inverse gray scale. The Laue was measured with the sample already mounted, before the ARPES measurement. The LEED was measured after cleaving and measuring, using an electron energy of 227 eV. Sharp peaks in the LEED confirm a clean and ordered surface. The sample was aligned with the (110) direction parallel to the detector slits (vertical in the image), as confirmed by the Laue and LEED. Panel (b) shows a simulation of the expected Laue scattering pattern, performed by Andres Santander [56].

Sample preparation, cleaving and measurement Measurements were performed along the (100) and (110) crystal directions. The samples were mounted on the sample holders with the (001) axis parallel to the normal emission direction. The orientation of the samples' rotation angle around this axis was performed using back-scattering Laue diffraction as in figure 1.9, panels (a) and (b). To align a selected $k_{\|}$ direction with the analyzer's slit direction, in Würzburg samples were rotated on the sample holder to match the desired orientation before finalizing the mounting. At 1^3, a distinguished direction was marked on the sample holder, and samples were subsequently rotated after cleaving using the available degrees of freedom of the manipulator. In both cases, the crystals were cleaved *in-situ* already at the measurement temperature. A highly ordered surface and the sample orientation were confirmed in Würzburg by sharp low-energy

electron diffraction (LEED) patterns on selected samples after cleaving and measuring, as illustrated in figure 1.9(c).

1.3.3 Guide to the Reciprocal Space of URu_2Si_2

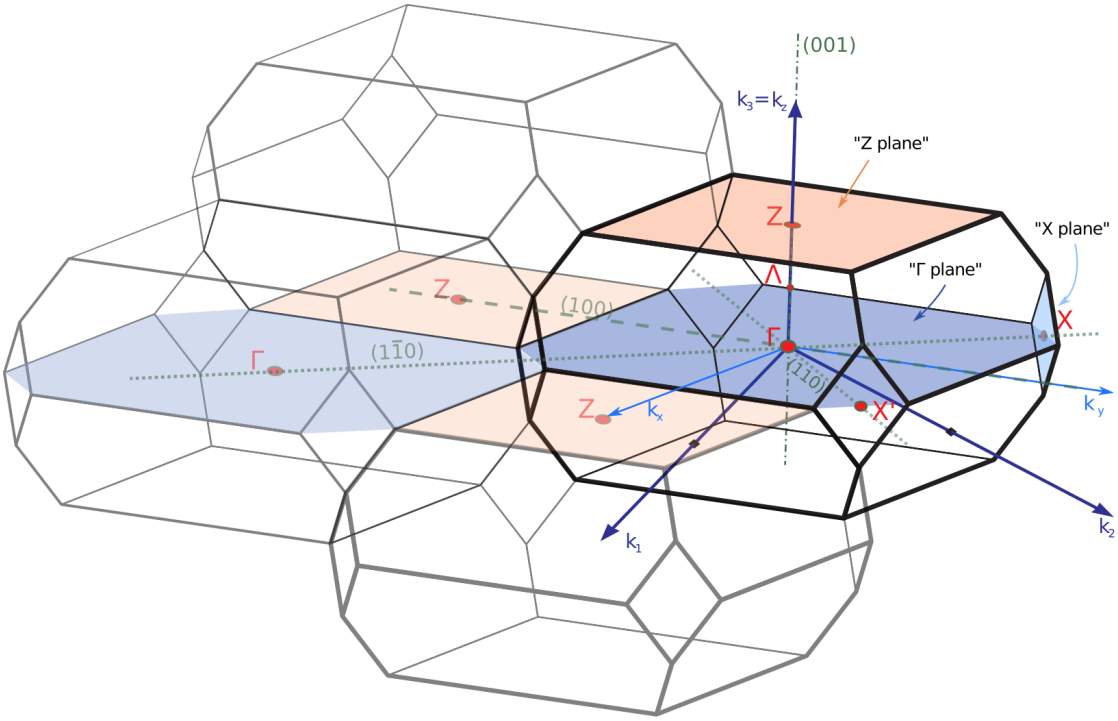

Figure 1.10: **URu_2Si_2 Brillouin zone of URu_2Si_2.** The Brillouin zone of the body-centered tetragonal URu_2Si_2 lattice, with its alternate stacking, is shown with directions and high-symmetry points relevant for this thesis. The reciprocal lattice vectors $k_{1,2,3}$ are drawn as blue arrows. The coordinate vectors k_x and k_y, used throughout this document for coordinates in the measurement plane perpendicular to (001) (parallel to the alternating red-blue area), are projections of the k_1 and k_2 vectors onto the plane.

The URu_2Si_2 Brillouin zone The URu_2Si_2 formally has a body-centered tetragonal a lattice, as shown in figure 1.1. The corresponding Brillouin zone is presented in figure 1.10. In the literature, the more convenient simple-tetragonal Brillouin zone is sometimes used, resulting from a crystal base encompassing two primitive cells (discussed in reference [49]). The Brillouin zones are alternately stacked in (100) direction. Neighboring cells of the reciprocal lattice are thus shifted by 1/2 height with respect to one another. This can be well observed in the alternative red and blue planes in figure 1.10. As a consequence, the (110) diagonal goes through a diamond-shaped BZ face of width 0.39 $Å^{-1}$ (corner to corner), which contains the X point, henceforth referred to as the X *plane*. The X point is thus 2-fold symmetric with respect to the X plane in a body-centered tetragonal lattice. Its symmetry would change to 4-fold, should the lattice become simple tetragonal.

The reciprocal space of the body-centered tetragonal lattice On the basis of equations (1.6) and (1.11), the reciprocal space of URu_2Si_2 can now be explored. Cuts through the Brillouin zone are shown in a unified graph in figure 1.11. They are tiled across the URu_2Si_2 reciprocal lattice along $k_x \times k_z$ [(100) direction], respectively $(k_x + k_y) \times k_z$ [(110) direction]. The graphic, inspired by reference [32], offers means for precise orientation in the 3D reciprocal space of URu_2Si_2 at a glance.

The excitation photon energies used in this thesis are drawn as colored arcs at their respective positions for $V_0 = 13$ eV (section 1.3.1). ARPES measurements are performed on hemispherical surfaces, which at normal emission are parallel to the ΓZ (red-blue) plane from figure 1.10. At higher angles, denoted by grey dashed lines, the measurement point disperses through k-space as indicated in figure 1.11. An overview over k-space points explored in the following is offered in table 1.1 to serve as a reference. Inevitably, some topics are mentioned, which will be formally introduced only in later chapters.

Table 1.1: **Overview over reciprocal space points discussed in this thesis.** Rows and columns enumerate high-symmetry points, respectively topics discussed in this thesis. Corresponding table cells contain section numbers at which the advertised information is found: the URu_2Si_2 surface state (SS), heat-up state (HS), coherent quasi-particles (QP_1 and QP_2), band hybridizations (Hybrd.) and gaps in energy or momentum.

Point (tilt angle)	**E** (eV)	**SS**	**HS**	**QP_1**	**QP_2**	**Hybrd.**	**Gaps**	**FS**
$\Gamma_{002} + 0.17$ Å^{-1}	21.2	3.1	3.2	2.3	3.2.3			2.3.3
				3.4.2	3.4.2			
$\Gamma_{002} + 0.18$ Å^{-1}	21.4			3.4	3.4	3.4	3.4.1, 4	4
Γ_{002}	17.0			3.4	3.4	3.4	3.4.1	
Γ_{003}	50.0			4	4		4	
$Z_{002} + 0.14$ Å^{-1}	8.4	3.1	3.2	3.2	3.2	3.2		
			3.4.1	3.4	3.4	3.4		
Z_{003}	31.0			3.4	3.4	3.4	3.4.1	4
Λ_{002} + 0.07 Å^{-1}	23.1	3.1						
Λ_{002}	24.0			3.4, 4	3.4, 4	4	3.4.1, 4	4
Λ_{003}	40.8	3.1				3.4		
X_{002} (30°)	21.2					3.3	3.3	3.3.1
X_{002} (20°)	21.4					4		
X'_{003} (21°)	40.8					3.3.2		

Reciprocal space points and directions nomenclature The directions (110) and $(1\bar{1}0)$ are perpendicular to one another. If a sample is oriented with the detector slit along (110), then the optical axis runs along $(1\bar{1}0)$ when the manipulator is rotated, and vice versa. However, as the directions are equivalent in URu_2Si_2, they will both be designated (110), indiscriminately, for the most part of this thesis. An exception to this rule will pose section 3.3 discussing data at the X point. This high-symmetry point is by definition 2-fold symmetric in a body-centered tetragonal lattice. Owing to the Brillouin zone stacking, it can be investigated in two ways by ARPES, determined

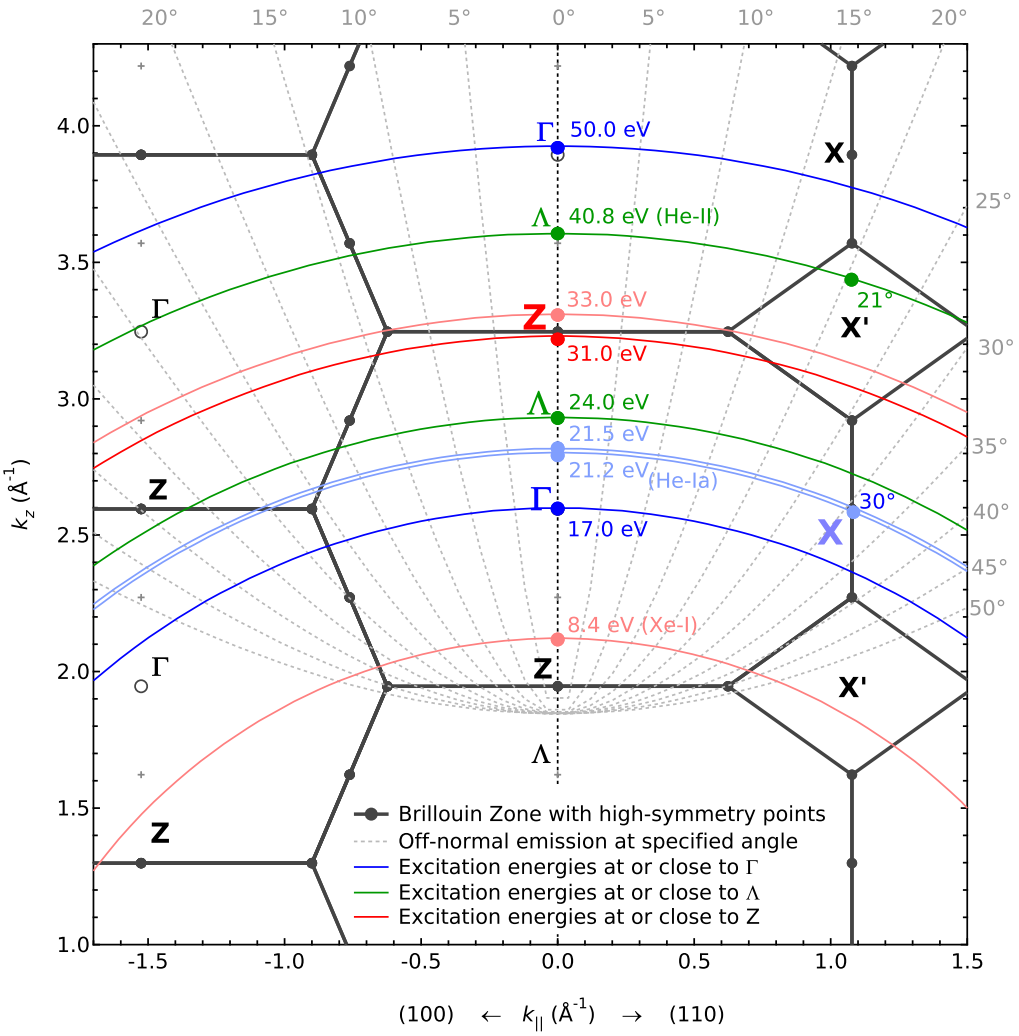

Figure 1.11: **Reciprocal space map of URu_2Si_2 with excitation energy arcs.** The map shows Brillouin zone (BZ) cuts along the $k_z = k_\perp$ direction of the reciprocal lattice of URu_2Si_2 along the vertical axis. The horizontal axis runs along the (100) direction, i.e. parallel to $k_x = k_{||}$ (equivalent to k_y) in the negative coordinate range. The (110) direction, parallel to $k_x + k_y$, is shown in the positive range. The radii of the colored circles correspond to the specified excitation energy in eV, assuming an inner potential $V_0 = 13$ eV. Dotted lines crossing the circles demark the photoemission angle with respect to the surface normal. The presentation method is inspired by reference [32].

by the combination of photon energy and tilt angle used: (**i**) with $k_{\parallel,\mathrm{det}}$ along the X plane, capturing band dispersions along the $(Z)-X-(Z)$ direction, or (**ii**) with $k_{\parallel,\mathrm{det}}$ perpendicular to the X plane, measuring dispersions along $(\Gamma)-X-(\Gamma)$. The labels X and X' will be assigned to the high-symmetry point for the cases (**i**), respectively (**ii**), as in figure 1.11. Also, the following direction conventions apply:

- For all scans at points *different* from X, if performed along (110), it will not be discriminated between (110) and $(1\bar{1}0)$. The momentum axis in the data will be labeled $k_{\parallel,\mathrm{det}}$ or $k_{\parallel,(110)}$.
- For scans at X using He-I$_\alpha$ excitation at 30° tilt angle, $k_{\parallel,\mathrm{det}}$ is parallel to (110), and $k_{\parallel,\mathrm{tilt}}$ is $(1\bar{1}0)$. Intrinsic momentum dimension in plots will therefore be labeled $k_{\parallel,(110)}$.
- For scans at X with He-II$_\alpha$ excitation at 31°, $k_{\parallel,\mathrm{det}}$ is along $(1\bar{1}0)$ and $k_{\parallel,\mathrm{tilt}}$ along (110). Momentum axis will be labeled $k_{\parallel,(1\bar{1}0)}$.

The label Λ, is used in figures 1.10 and 1.11 to designate the half-way point between Γ and Z. This is a deviation from the usual convention for the body-centered tetragonal lattice, but is in accordance with recent nomenclature in URu_2Si_2 literature (e.g. reference [51]). In an simple tetragonal lattice, with the Brillouin zone half the height of its body-centered tetragonal counterpart, Λ becomes a high-symmetry point.

To improve readability, for the remainder of this thesis, the usual notation of specifying a Brillouin zone counter in the index of a high-symmetry point will be abandoned. Instead, points in momentum space will be denoted by the Greek symbol of the closest high-symmetry point using *excitation energy* of the respective experiment as index. For example, $\Gamma_{21.2}$ and $\Lambda_{40.8}$ denote the points investigated by He-I and He-II along k_z, $Z_{8.4}$ will be the point reached by the Xe-lamp, Λ_{24} will be another point available by synchrotron radiation monochromatized at 24 eV, and so on.

Chapter 2

Previous Efforts

2.1 Research Context

2.1.1 Brief Project History

The project into which this thesis is embedded was born and led by Prof. Dr Andres Felipe Santander-Syro (A.F.S.S.) from CSNSM, Université Paris-Sud in 2007. At a time in URu_2Si_2 research history when the participation of heavy quasi-particles in the phase transition had not yet been proven experimentally, it had the stated goal of investigating Fermi surface instabilities across the HO transition. Prof. Dr Friedrich Reinert (F.R.) from Experimentelle Physik VII, Universität Würzburg, was able to contribute one of the few ARPES systems world wide capable of delivering the required resolution and temperature.

Findings of the cooperation in the period 2007–2008, of which the most prominent include a Fermi-surface instability reported in [57], were discussed as a part of the PhD work of Markus Klein (M.K.) and of my diploma thesis (references [49, 54]). The latter was made under direct supervision of M.K., with A.F.S.S. and F.R. as formal advisors. Those results will briefly be reviewed in the following. Research then continued through 2009 until present, posing at first the scientific basis for the MSc thesis of Cedric Bareille (C.B.), and later for his PhD thesis, together with the work of my own PhD thesis.

2.1.2 Structure of This Thesis

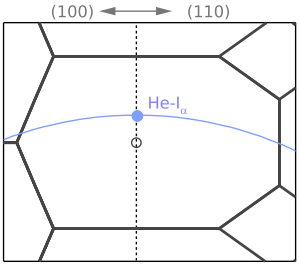

Previous efforts of the group The current chapter 2 of this manuscript aims to introduce the work of the Paris / Würzburg group from 2007–2008, and thus to provide the proper context for the following research. For this purpose, "old" results from this period will be reviewed in section 2.3. The data presented here was measured using He-I$_\alpha$ excitation energy at the reciprocal space location designated by the image to the right. After a brief overview of the electronic structure, results published in reference [57], will be recalled. Where appropriate, a limited amount of new data will be intermixed to complete the picture (sections 2.2 and 2.3.3).

Main theme of this thesis Chapter 3 will then present the main results of this thesis. Taking over from efforts of 2007–2008, it will improve on side aspects not fully covered by [57], with both new data and more in-depth analysis. Then new results will be presented, emerging from the following generation of experiments performed since 2009. The findings at the core of this thesis, concerning the surface state, the heat-up state, and the development of the "hidden-order" on a pre-formed Kondo lattice, are published as references [61, 77] or in preparation [83]. These represent roughly the "first half" of the 2009–2013 investigations.

Parallel efforts of the group Finally, in chapter 4, a short review of the "second half" will be offered. It exposes with momentum-resolved data the gapping of the Fermi surface, the symmetry, and the loss of entropy across the "hidden-order" transition. The work was performed with my full contribution to the experiments, and partial contributions to the data analysis and discussions. Although the more detailed presentation and discussion of those results poses one of the focal points C.B.'s PhD thesis. They are to be published as reference [76].

As with any collaboration on a topic this vast, a strict separation of the scientific merits is difficult. C.B. contributed crucially to the research for chapter 3, just as I did for chapter 4. Nonetheless, utmost care was taken to label alien contributions as such. Direct contributions of other persons to this thesis, in particular of C.B., were marked correspondingly. If in doubt, the following approximate formula is suggested: facts presented quoting figures from other works were researched predominantly by others, while those based on original figures represent my own work.

2.2 Wide Energy Range Scans at the Γ-point

To provide an overview over the electronic structure, figure 2.1 shows ARPES scans performed over a wide energy range with a nominal resolution of $\Delta E \geq 10$ meV using the He lamp. This kind of data—low-resolution wide-range scans—were always collected several hours after cleaving, when the sample surface had lost the ability to provide good high-resolution data (section 3.1). As a consequence, the surface was usually badly degraded, resulting in poor contrast and an effective resolution lower than 10 meV.

Panels (a) and (b) show the raw data in the PM and HO phase at the $\Gamma_{21.2}$ point. In (c) and (d), the same data is displayed as 2^{nd} derivative plots. This enhances the contrast of the ARPES intensity such that individual dispersions of intense bands can be well observed. To check for any HO induced changes in the band structure at higher binding energies, the dispersions were traced by hand as demonstrated by the overlaid dashed lines. This procedure was repeated for another pair of scans below/above the HO transition temperature, not shown here. Cumulative results are displayed in figure 2.2 (a,b). The same multitude of bands is visible in both the ordered and unordered phases. There is no difference across the HO transition detectable in the low-resolution band structure for binding energies as low as 1.5 eV below the Fermi level, as figure 2.2(c) demonstrates. As previous experiments, to be reviewed below, already demonstrated, electron-spectroscopical evidence is more likely to be found in high-resolution data close to the Fermi level.

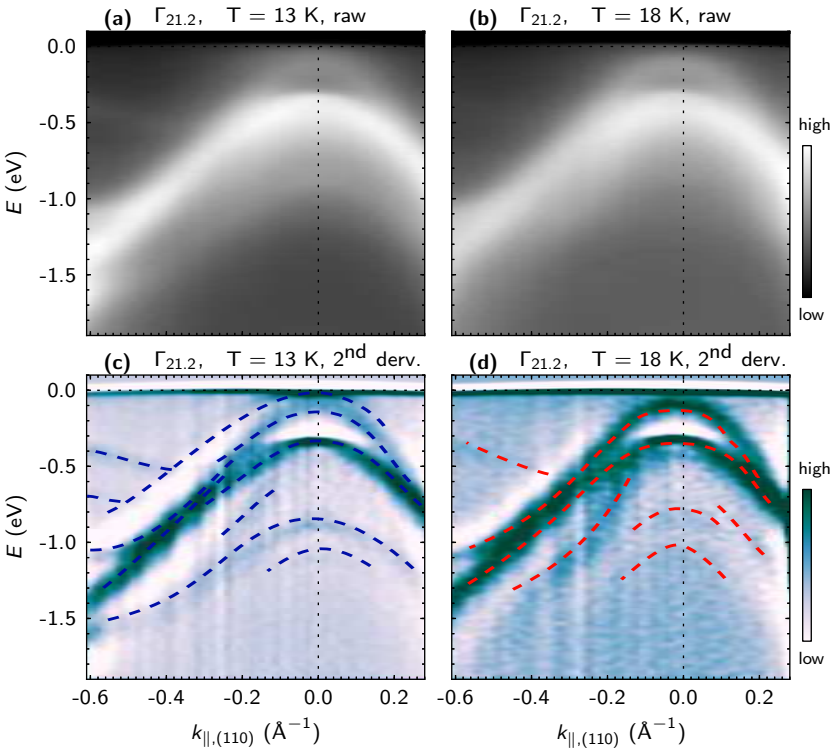

Figure 2.1: **ARPES scans over a wide energy range at the Γ point.** Scans at low resolution ($\Delta E \geq 10$ meV) in the HO phase ($T = 13$ K) and PM ($T = 18$ K) phase at the $\Gamma_{21.2}$ point of URu_2Si_2 as raw ARPES data (a-b), and convoluted with the 2^{nd} derivative of a 2D Gauss function (c-d). Dashed blue (red) lines on top of the 2^{nd} derivative plots guide the eyes to the visible bands in the HO (PM) phase. The light hole-like band crossing E_F visible in this particular data set only in the HO phase (a,c), is actually also detectable in the PM phase in different data sets (see figure 2.2 and following presentation of high-resolution data). Band structure changes across T_{HO} are not visible at this resolution.

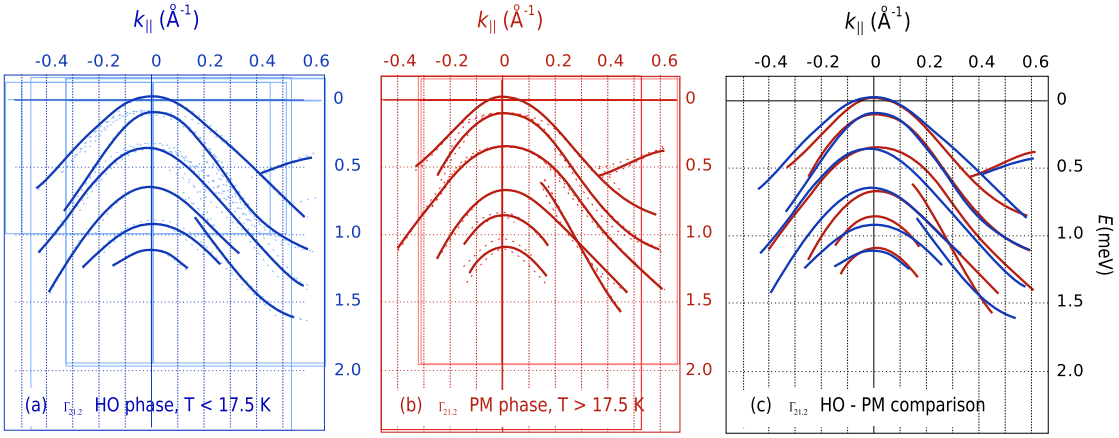

Figure 2.2: **Comparison of the HO and PM band structure at $\Gamma_{21.2}$.** Band locations from ARPES scans from figure 2.1 and similar in the HO [panel (a)] and PM [panel (b)] phase were cumulated and compared in panel (c). At this resolution, no detectable bands change across the HO transition.

2.3 High-Resolution ARPES at the Γ-point

2.3.1 The High-Resolution Features at the Fermi Level

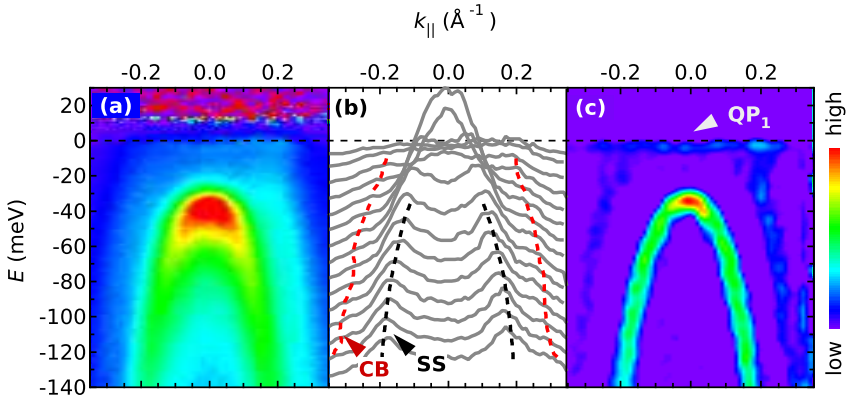

Figure 2.3: **High-resolution scans at $T = 10$ K along the (110) direction.** Panel (a): energy-momentum intensity-map normalized by the Fermi-Dirac distribution. Panel (b): MDCs of the same data. The features corresponding to the SS and CB dispersion are shown, respectively, by the black and red dashed lines. Panel (c): Second derivative in the $k_{||}$ and E-directions, normalized to the highest intensity point and averaged. Only negative values of the second derivative (representing band maxima) are shown.

Figure 2.3 shows typical high resolution He-I spectra of URu_2Si_2 along the (110) direction at 10 K. Here, the energy region -150 meV $\leq E \leq 30$ meV was chosen. E_F corresponds to zero energy. Panel 2.3(a) shows the energy-momentum intensity map normalized by the Fermi-Dirac distribution (FDD). The most prominent structure is an intense hole-like structure, bound at $E \approx -35$ meV. This is a surface-state (SS), which

will be discussed in detail in section 3.1.

Figure 2.3(b) shows the momentum distribution curves (MDCs) of the intensity map in panel (a). The MDC peaks corresponding to the surface state are traced by the black dashed lines. Along the flanks of the SS, the MDCs also present small but distinct shoulders dispersing parallel to the surface band and crossing the Fermi level at $k_{\|} \approx \pm 0.2$ Å^{-1}. They belong to a hole-like band (CB), traced by the red dashed lines. Slightly below the Fermi level, a narrow structure of coherent heavy quasi-particles is visible, referred to as QP_1 throughout this thesis. QP_1, SS and CB appear more clearly in figure 2.3(c), displayed as a 2$^{\text{nd}}$ derivative of the data from panel (a).

CB and QP_1 are related to HO and will be briefly introduced in the following. They represent the major findings from 2007–2008, and were extensively discussed in references [49, 54, 57].

2.3.2 Fermi Surface Instability Across the HO Transition

The temperature dependent behavior of QP_1 is displayed in figure 2.4. Panel (d) shows FDD-normalized ARPES intensity maps, in temperature succession across the HO transition from 26 K to 10 K. The heavy feature shifts from the thermally occupied part of the spectrum ($E > E_F$) to $E < E_F$ as the temperature falls below T_{HO}. In the normal state of URu_2Si_2, it is visible as non-dispersing spectral intensity spreading between $k_{\|} = \pm 0.2$ Å^{-1}. In this way it is clearly discernible from any artifacts that could have been created by the FDD normalization. Within experimental resolution, its dispersive nature is observed only at temperatures well below T_{HO}. Panels (a) and (b) show the ARPES data as raw, respectively FDD-normalized energy distribution curves (EDCs) integrated between ± 0.2 Å^{-1}. Findings are summarized in panel (c), which show the energy of the lowest point of QP_1 in dependence of the relative temperature T/T_{HO}.

A connection between QP_1 and CB is indicated by figures 2.5(b,d) and 2.6. ARPES intensity maps, EDCs, and MDCs of the HO phase are shown for the (110) and (100) directions. CB is seen to disperse through E_F at precisely the same momentum coordinates at which QP_1 bends obtaining its characteristic "M"-like shape. This corresponds to $k_{\|)} \approx 0.2$ Å^{-1} in (110) direction, and $k_{\|} \approx 0.15$ Å^{-1} along (100). A hybridization between QP_1 and CB appears likely, but could not be directly detected, e.g. by showing the formation of a band gap, under the given experimental conditions.

2.3.3 The HO Fermi Surface at the Γ-point

The first cut through the Fermi surface of the HO state of URu_2Si_2 was inferred from low-resolution ($\Delta E = 10$ meV) 2$^{\text{nd}}$ derivative data in M.K.'s PhD thesis [54]. The corresponding in-plane APRES data at 21.2 eV is shown in the upper panel of figure 2.7, with 2$^{\text{nd}}$ derivative in the lower panel. Black circles demark the probable points at which CB would disperse through E_F, extracted from the 2$^{\text{nd}}$ derivatives.

A high-resolution version of the Fermi surface ($\Delta E = 5.18$ meV) is shown in figure 2.8. The data was gathered in 2009 within 1/2 hour after the fresh cleave of a sample. This represents the limit of what is achievable with the He-I setup in terms of resolution and signal quality due to rapid surface degradation (section 3.1). Panel (a) shows the raw Fermi surface, obtained by integrating over 2 meV around E_F. In panel (b), it is displayed 4-fold symmetrized. The data from (a) was sliced in the $k_{\|,\text{det}} \times k_{\|,\text{tilt}}$ plane radially

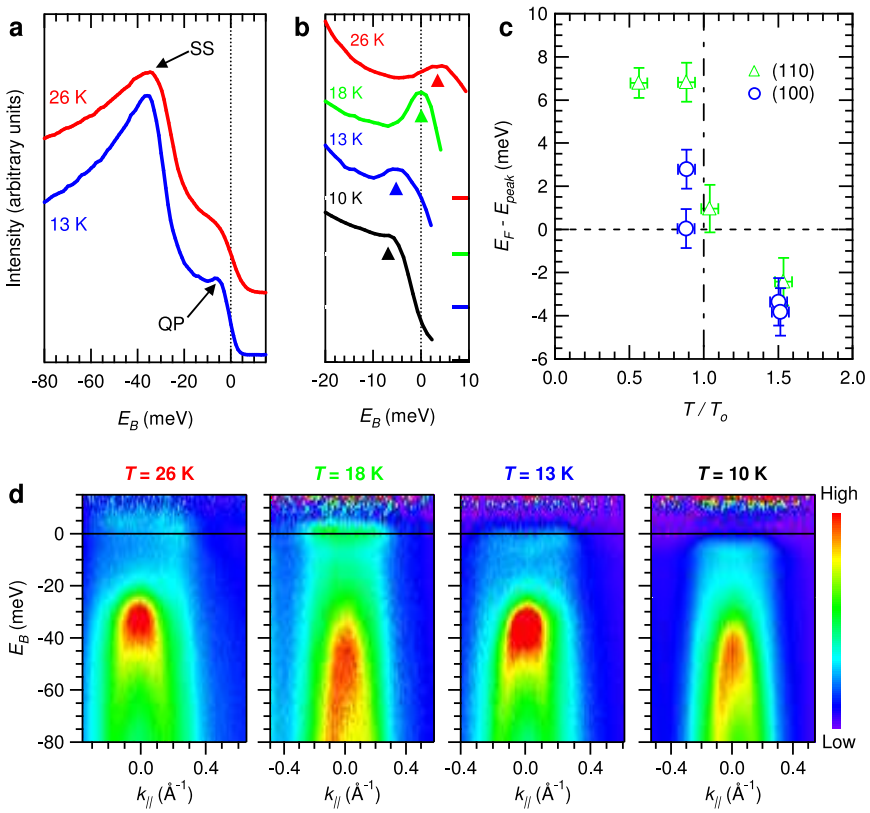

Figure 2.4: **Heavy fermion band at Γ evolving with temperature.** Panel (a): EDCs integrated within ±0.2 Å^{-1} along the (110) direction in the PM (red) and HO (blue) phase. Panel (b): EDCs integrated between ±0.2 Å^{-1} from the data presented in panel (d) and normalized by the FDD for various temperatures. The heavy band peaks are indicated by small triangles, small colored dashes at the right border denote the zero-intensity level for each spectrum. Panel (c): summary of the temperature evolution as binding energy of the QP_1 peak plotted against temperature. Higher points on the energy axis correspond to more strongly bound states. Panel (d): temperature evolution of the QP_1 peak presented by ARPES intensity color plots. *Image from reference [57].*

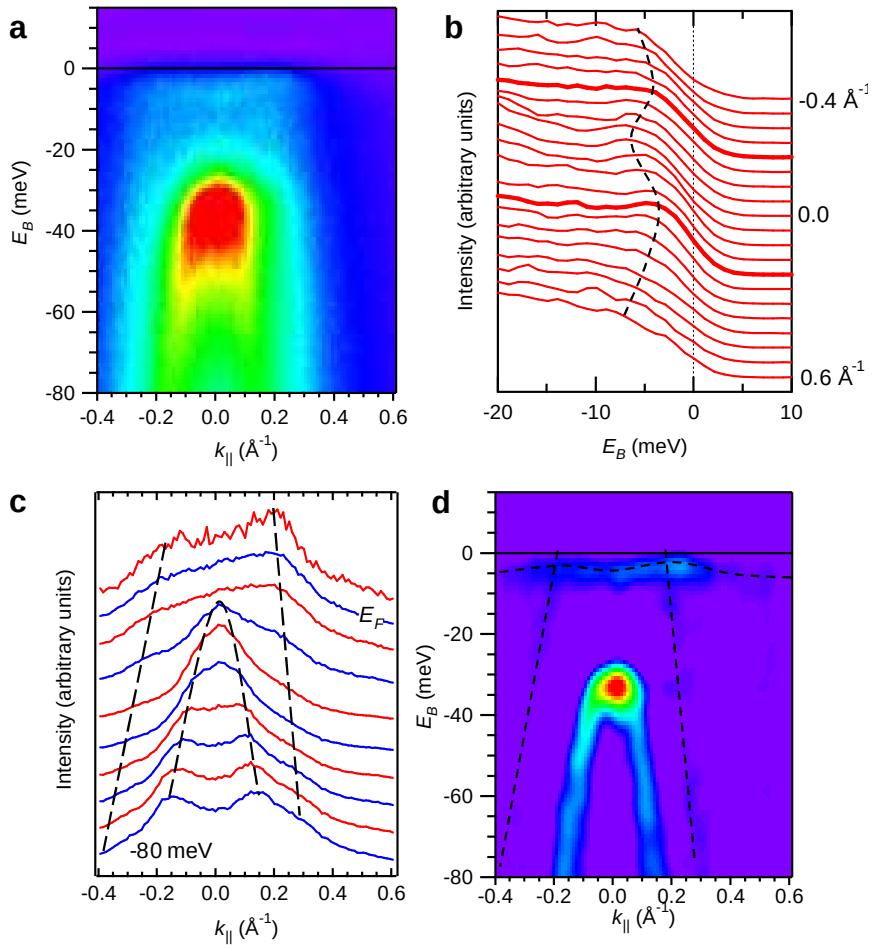

Figure 2.5: **Hybridization of the heavy band with a hole-like conduction band.** Panel (a): ARPES intensity color plot of the heavy band at $E \approx -7$ meV measured in (110) direction at $T < T_HO$. Panel (b): EDCs of the data shown in panel (a) in the region close to E_F. A black dashed line illustrates the dispersion of the heavy band. Panel (c): Corresponding MDCs, with black lines showing the dispersions of the surface state (discussed later) and another light, hole-like band (CB), apparently crossing E_F at the k_F vectors close to ± 0.2 Å^{-1}. Panel (d): Negative values of a 2$^{\text{nd}}$ derivative intensity plot of the data set in (a), highlighting curvature peaks. Black dashes sketch the E_F crossing of CB and QP_1 at the spots where QP_1 folds. *Image from reference [57].*

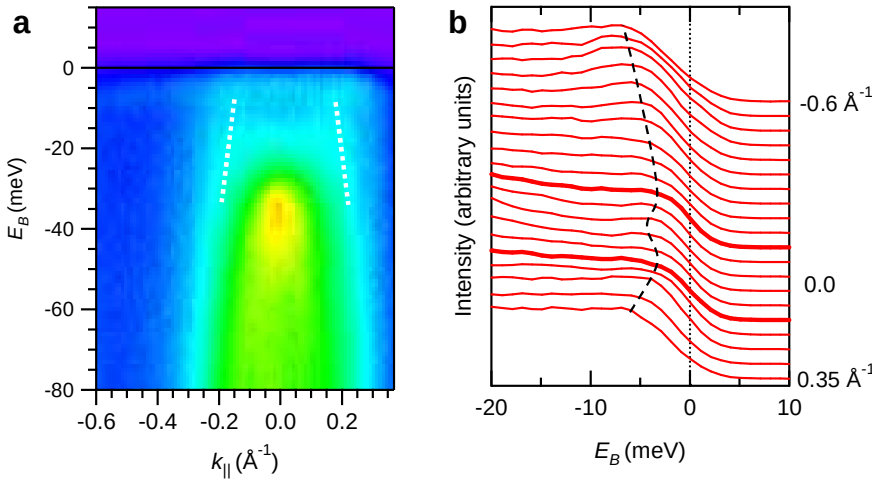

Figure 2.6: **The interaction between QP$_1$ and CB in the HO phase at $\Gamma_{21.2}$.** Panel (a): ARPES intensity measured in the HO phase (T = 14 K) along the (100) direction. A dispersing heavy-fermion band is visible at $E = -4$ meV below E_F. Parallel to SS, a hole-like conduction band (CB), indicated by white dashed lines, is detected. Panel (b): EDC stacks of the same data set. Black dashed line offers a guide to the eye for the heavy-fermion dispersion. Bold lines represent EDCs with their peak closest to E_F. *Image from reference [57].*

starting from the (0,0) point, in increments of 10°. The resulting MDCs are displayed in panel (c). Dashes on the MDCs indicate the maximum intensity, representing the $k_{||}$ distance from (0,0) at which the tips of the "M"-like QP$_1$ apparently touch E_F. They correspond to the points at which CB would disperse through E_F. The positions of the maxima of the MDCs from panel (c) are also overlaid on panel (b) as blue crosses. Empty circles on top represent the previous FS map trace from figure 2.7, for comparison. The shapes of the FS cuts match very well, resembling a square, with its corners along the (110) direction.

Interestingly, the only structure of approximately similar size in LDA calculations on paramagnetic URu_2Si_2 (e.g. from [32]), is rotated by 45 degrees with respect to the experimental data: it has its corners along (100). A misalignment of the URu_2Si_2 sample has been triple-checked by Laue, LEED, and by examining the optical appearance of the crystal surface (figure 1.9) and can be excluded.

An intriguing property of the high-resolution FS map from figure 2.8 is the noise structure along the borders of the main sheet. When viewed in this particular color map, in its 4-fold symmetrized version, the noise appears to add up to a further 4-fold symmetric FS sheet, emphasized by dotted green lines in panel (b). If it could be established as a legit structure, as opposed to random noise in the background, it may reconcile orientation differences between LDA and the experimental data. Unfortunately, for now the MDCs in panel (c) do not support this first impression beyond a reasonable doubt. However, the issue will be discussed again using better data in chapter 4.

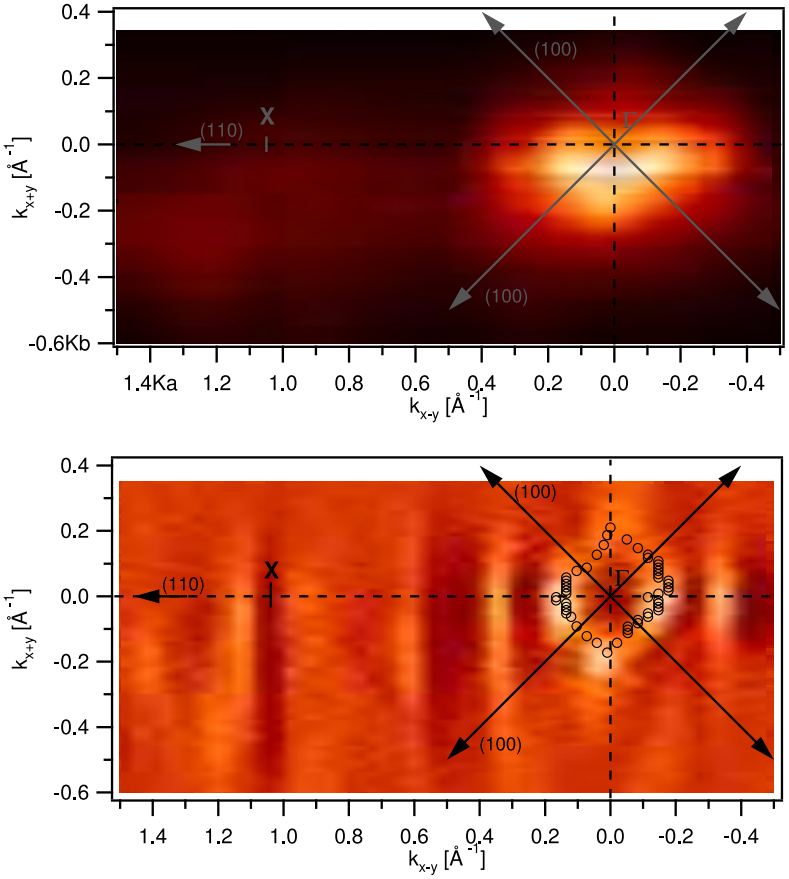

Figure 2.7: **Low-resolution He-I Fermi surface trace of URu_2Si_2.** Top panel shows an ARPES intensity map of a Fermi surface at $\Gamma_{21.2}$ measured at low resolution ($\Delta E \geq$ 10 meV). Bottom panel shows the same data in its 2nd derivative form, overlaid with black circles tracing the likely shape of the Fermi surface. The k_F vectors were obtained by tracing the points at which CB would disperse through E_F in the corresponding ARPES intensity plots used to create the Fermi surface map. *Image from reference [54].*

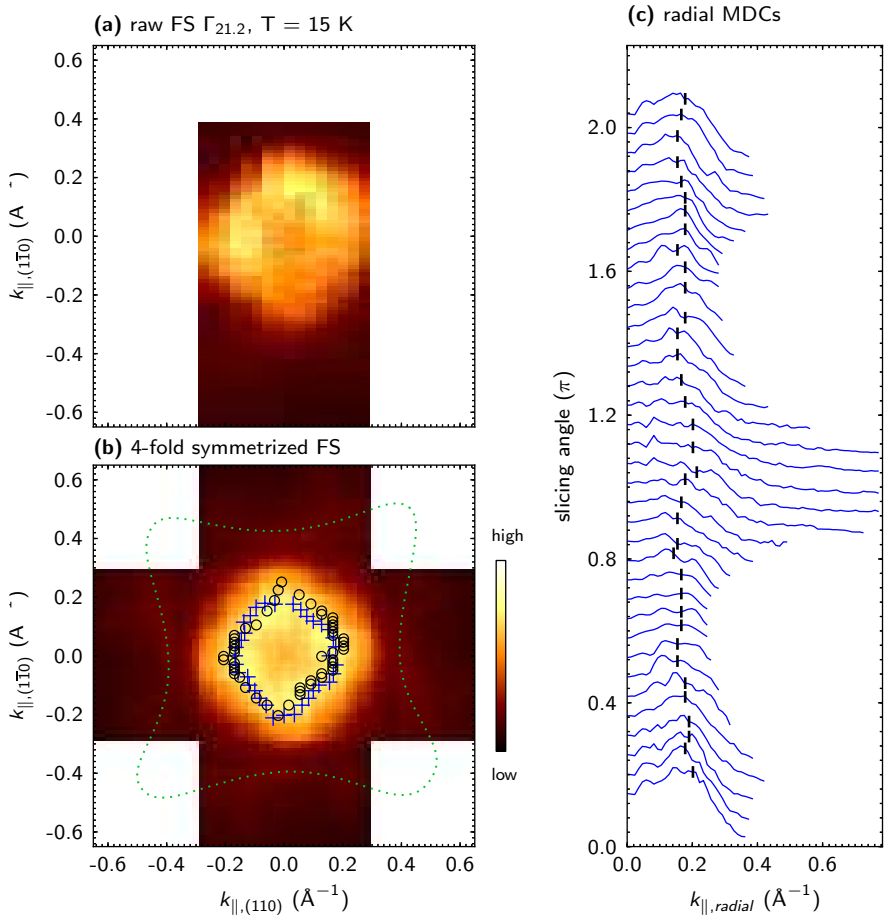

Figure 2.8: **High-resolution He-I Fermi surface of URu_2Si_2.** Raw ARPES Fermi surface map, obtained by integrating over 2 meV around E_F, shown (a) non-symmetrized and (b) 4-fold symmetrized. Blue crosses in panel (b) denote maxima of MDCs in panel (c); black circles are reproduced from figure 2.7, for comparison. MDCs in (c) were obtained from radial cuts through the data of panel (a) every 10°. Resulting Fermi surface trace is displayed in panels (b) as marked dots. Black circles are reproduced from figure 2.7, for comparison. Dotted green line suggests the shape of another trifle-like Fermi sheet (see main text).

Chapter 3

Unveiling the "Hidden-Order"

3.1 The Surface State

This section deals with the electronic structure feature labeled "SS" from figure 2.3. An analysis will be presented in the following of why this structure is identified as a surface state and what its likely origins are. The data at the basis of this discussion was gathered using laboratory He and Xe light sources at the reciprocal space points indicated in the figure to the left. Results were published in [61].

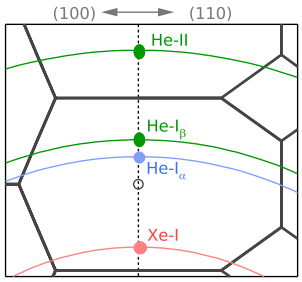

3.1.1 Similarities Between SS and CB

For a more quantitative analysis, each MDC in figure 2.3(b) was fitted with four Lorentzians: two innermost for the SS peaks, and two outermost for the CB peaks. The obtained peak maxima represent the dispersions of the SS and CB. The former, displayed as black dashed lines, was adjusted with a parabola, fixing the band maximum at $E = -36$ meV, as given by the maximum intensity in the EDC at $\Gamma_{21.2}$. The process is visualized in figure 3.1, where black open circles denote the SS and CB dispersions obtained from the MDC fitting procedure above and the full black circle is the SS band maximum. The resulting parabolic dispersion, shown by the inner white curve, has an effective mass of $m^\star \approx -1.4 m_e$. If the band maximum of this parabola is shifted upwards to an energy of 140 meV, it matches well with the CB dispersion. Hence, within experimental accuracy, the two bands have the same effective mass.

3.1.2 Lacking Dependence of Photon Energy

The intensity maps in the upper panels of figure 3.2 show the SS using the photon energies of He-I$_\alpha$, He-I$_\beta$, He-II$_\alpha$ and Xe-I, in each case for a freshly cleaved sample. Measurements with the He lamp were performed lasting only a few minutes. The SS dispersion and band maximum are the same in all four cases, despite the different k_z values for the different photon energies. Thus, this state does not disperse along k_z, in accordance with its identification as a surface band. The different intensities in the angle-resolved spectra of the He lamp have their origin in the intrinsic properties of the lamp used for He-I$_\alpha$ and He-I$_\beta$. The intensity in the He-II$_\alpha$ spectrum, lower than expected from lamp properties

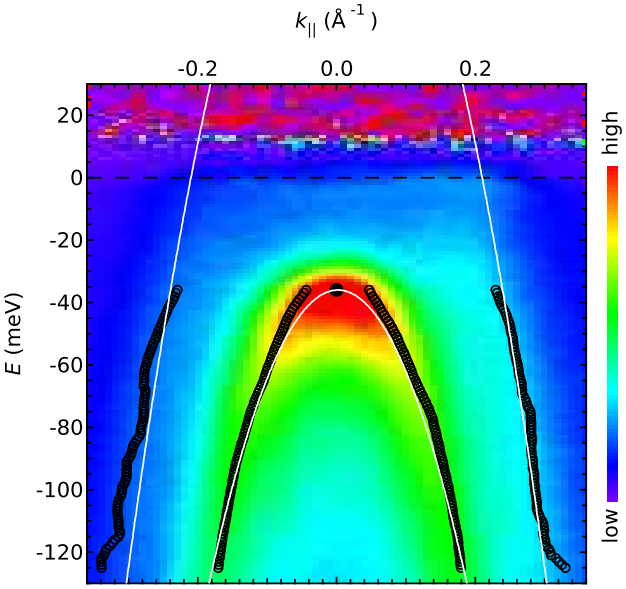

Figure 3.1: **Visualisation of the effective masses of the CB and SS.** This spectrum was measured at $T = 10$ K along the (110) direction. The open black circles trace the dispersions of the MDC peak maxima attributed to the SS (inner branches) and CB (outer branches). The inner white lines show a parabolic fit to the SS dispersion, performed keeping the band-maximum at $E = -36$ meV fixed (full black dot). Shifted up in energy to $E \approx 140$ meV, the parabola matches very well the CB (outer white lines), suggesting SS to be a Shockley state for which CB is the associated upper bulk band.

alone, could be attributed to the low photo-ionisation cross section of surface states for high photon energies [3].

Previous studies using a tunable light source have shown a narrow structure close to the Fermi energy, the intensity of which is strongly modulated along k_z [32]. The said structure can be consistently identified with SS. The bottom panel of figure 3.2 emphasizes that the SS band-maximum is constant as a function of photon energy by showing the corresponding integrated EDCs, to ameliorate the signal-to-noise ratio for the spectra with the He-I$_\beta$ and He-II$_\alpha$ lines.

The influence of the surface aging on the SS is shown in figure 3.3 using FDD-normalized intensity maps recorded at 17 K. From left to right the time from cleaving is 10, 40 and 70 minutes. As time—and thus surface contamination—increases, the SS shifts to larger binding energies, a behavior known from surface states [36, 39]. In contrast, as seen from this figure, the QP$_1$ band at E_F keeps its position, and only its width and amplitude degrade.

To investigate the cause of surface aging, further experiments were performed using different combinations of "lamp on/off" and "He-flow on/off" patterns. Figure 3.4 shows three different surveys of the SS band maximum during the first hour after cleaving. In the first survey, shown by the red circles and lines, the He-lamp was continuously running (He-flow on, lamp on). It confirms that the SS shifts down in energy with time after cleaving, in an approximately linear way. For the other two, the measurements were stalled after 10 minutes from cleaving over periods of time between 30 and 45 minutes. The green squares and lines show the survey with the lamp and He-flux switched off during the interruption, and the blue triangles and lines show the survey with the He-flux on at the normal operation pressure of 8×10^{-10} mbar and the lamp off during the interruption (i.e. only the voltage of the discharge circuit was switched off). In both cases, as the lamp was turned on again, the SS band continued shifting down in energy at approximately the same rate it did in the "He-flux on/lamp on" survey. This kind of behavior has been observed previously in experiments on surface states of noble

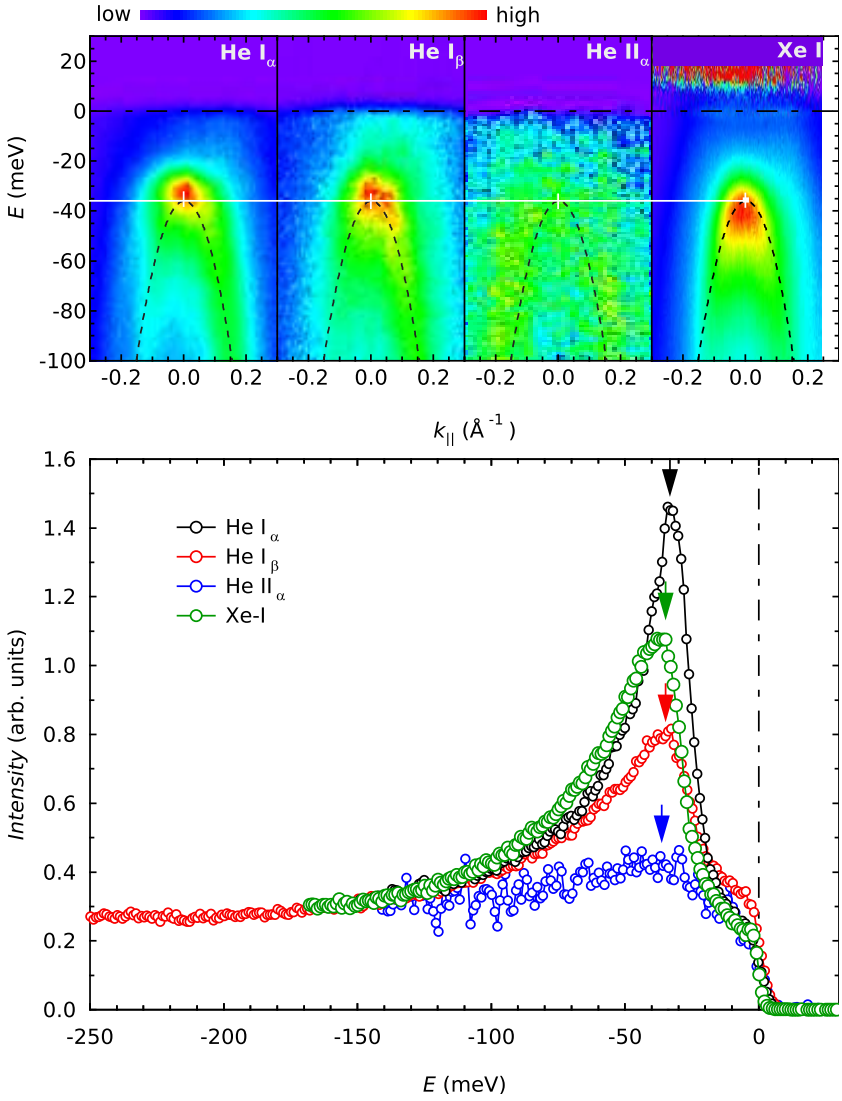

Figure 3.2: **EDCs of surface state using different photon energies.** Data measured with He-I$_\alpha$, He-I$_\beta$, He-II$_\alpha$, and Xe-I excitation energy shown both in angle-resolved mode (top) and integrated over the maximum intensity area around $k_{||} = 0$ (bottom). All measurements in this figure were done in the minutes following cleaving. The SS band is detectable at exactly the same binding energy for all photon energies, indicating its surface character.

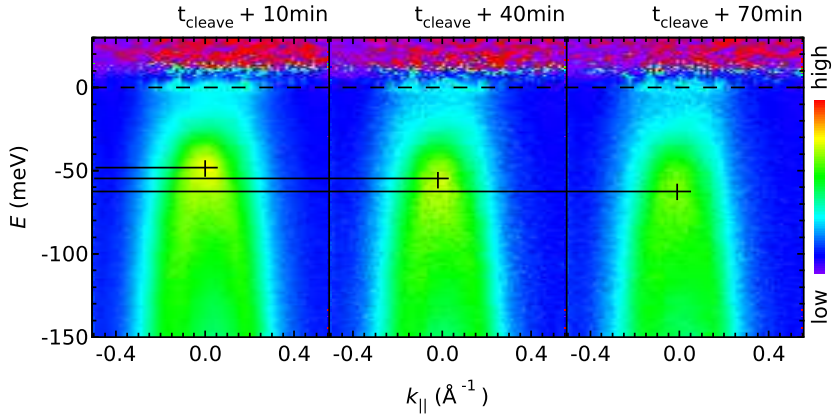

Figure 3.3: **Spectra measured 10, 40 and 70 minutes from cleaving.** All spectra were measured on a single sample at $T = 17$ K and are displayed normalized by the FDD. Intensity in all panels is normalized to the flat QP_1 peak at E_F. The surface state shifts towards higher binding energies broadens as a consequence of surface contamination. In contrast, the QP_1 feature at $E = 0$ does not shift with time.

metals [36].

The data emphasizes that surface contamination is mainly due to residual gases or ions of the plasma in the running He lamp [39], like activated hydrogen atoms or molecules. As the band, opposed to the bulk QP_1 feature, shifts with increasing surface aging and lacks any k_z dispersion, it is safe to be regarded as a true surface state. In the following section its possible origins will be discussed.

3.1.3 Origin of the Surface State

In a free electron model, and ignoring resonance effects, surface states appear in local gaps of the projected 3D band structure. They are accompanied by bulk bands, at higher and, respectively, at lower energies.

In this case, the fact that the dispersions of the SS and CB match suggests to identify the latter as the upper bulk band for the former. Candidates for the lower bulk band can be found in the structures at energies $E \leq -0.5$ eV at $\Gamma_{21.2}$, which are mainly of d character [32]. Figure 3.5 shows energy-momenta intensity maps around $\Gamma_{21.2}$, along both the (100) and (110) directions, in a wide energy range down to $E = -2.5$ eV. The red dashed line indicates the SS with the parabolic dispersion calculated as described above. The red dotted lines represent the proposed bulk bands. The upper one is the CB, too weak to be seen in the color scale of this plot. The lower serves as a guide to the eye to find a matching candidate in the bands at $E \approx -0.5$ eV, where most spectral intensity is present. Consequently, one viable interpretation is that the SS arises in the inverted gap of an *sp*- and *d*-like bulk band, and shifts towards the more bound *d*-band upon adsorption of activated H-atoms from the He plasma lamp [39].

In general, a surface state can shift upon deposition of residual gases for several reasons: (**i**) character change of the surface state to more overlayer-like, as in the case of adsorption of thin films in an ordered deposition; (**ii**) electron transfer between the surface state and the adsorbate; (**iii**) Pauli repulsion in the case of adsorbates with a

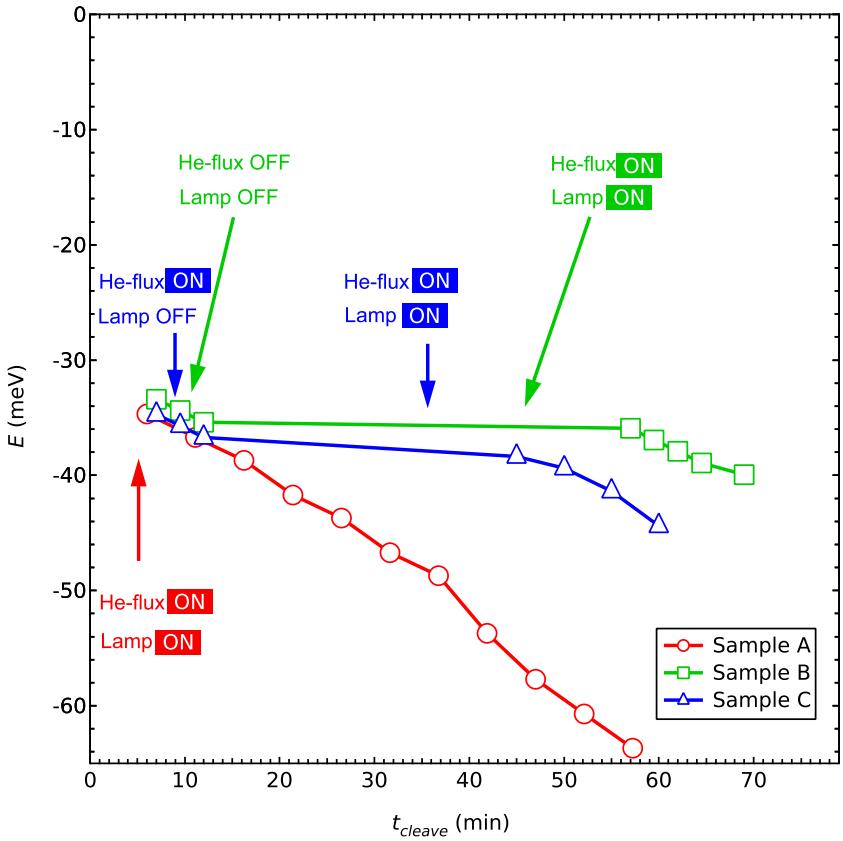

Figure 3.4: **Three series of systematic time-dependent scans.** The binding energy of the SS band-maximum is plotted against time from cleaving. The constant binding energy for the series where the high-voltage of the He-lamp was turned off for a period of time (blue and green curves) indicates that the origin of the surface contamination are the residual gases from the He-lamp plasma.

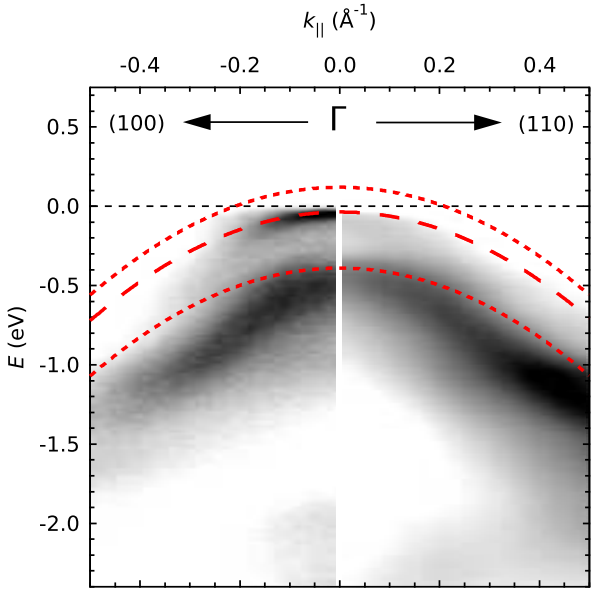

Figure 3.5: **The surface state and candidates for lower and higher bulk bands.** Energy-momentum intensity maps in inverse gray scale for URu_2Si_2 in a wide energy range are shown along the (100) and (110) directions. The dashed red line represents the fitted parabola for the SS, as discussed in the context of figure 3.1. The dotted red lines represent the CB and a candidates for the lower associated bulk band, as discussed in the text.

similar symmetry of the wave function as the surface state; and (**iv**) changes in the work function of the surface by the adsorbate, following the *phase accumulation model* [2, 44, 7, 58]. Option (**i**) is unlikely here, because only small quantities of unordered residual gases are adsorbed. Option (**ii**) is also difficult to support, as SS is a fully occupied band bound below E_F. Pauli repulsion and / or changes in the surface work function are two remaining scenarii that will be briefly explored.

The Pauli-repulsion scenario Following the Pauli principle, the wave functions of the surface state and of the electrons in the adsorbed molecule must be orthogonal. In order to accommodate for an adsorbate with a similar symmetry, a surface state shifts its character and hence its energy [25, 46]. Thus, the scenario (**iii**) above, involving Pauli repulsion, could be sustained here if CB and the bands depicted in figure 3.5 were assigned as the higher and lower bulk bands for SS. Calculations [51, 52] show that the k-space region close to E_F at Γ is mainly populated by *spd* bands attributed to Ru and Si. Comparing with the DMFT band-structure from reference [52], CB could be attributed to Si-p states.

Changes in the surface work-function and phase-accumulation scenario According to the phase accumulation model, waves of electrons and image charges are multiply reflected at potential barriers and interfere constructively. They give rise to an infinite number of bound states at the surface, the first of which are typically the observed surface bands. The binding energy of the surface bands depends, among others, on the energies of the lower and upper bulk band and on the work function of the surface. A lowering of the work function as a consequence of unordered deposition could well explain a shift of SS towards more bound states [20, 28]. But for a quantitative analysis, systematic investigations of the work function of URu_2Si_2 are needed.

3.1.4 Conclusion

To summarize, clear evidence was presented that a hole-like band of URu_2Si_2 bound below $E = -35$ meV and typically used to characterize the Γ point is a surface state. It is suggested that this band arises in the projected gap of a light hole-like Ru-4d band and a lighter conduction band, possibly of Si-p character. The shift in energy of this surface band upon adsorption of residual molecules or ions from the He-lamp plasma might arise from Pauli repulsion and / or local changes in the surface work function following the phase accumulation model.

Detailed slab layer calculations would be helpful to confirm the existence of a surface state within a gap formed by the lower / upper bulk bands with the correct symmetry combination, and to identify the mechanism underlying its energy shift upon surface degradation. Additionally, more bulk-sensitive experimental methods like Compton scattering [4, 21, 31] or ARPES with higher excitation energy [30, 42], could be employed to provide supplementary insight.

Independently of what its origin may be, the SS at Γ is not related to the HO transition. Its peak intensity, which is almost an order of magnitude larger than the observed heavy quasi-particle features, rather obscures bulk f-electron physics. As residual gases from plasma lamps without windows quickly affect the surface of URu_2Si_2, the signal-to-noise ratio also degrades, additionally complicating the detection of heavy quasi-particles.

In such cases, high-resolution measurements on this material should therefore be performed possibly within minutes after cleaving in order to achieve physically meaningful results.

3.2 The Heat-up State

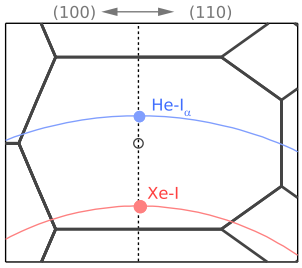

The surface state of URu_2Si_2 is significantly altered if a cleaved sample is heated up to room temperature and cooled down again. This was observed incidentally, when the He lamp in the Würzburg laboratory setup was replaced by the Xe lamp. In reciprocal space, the Xe-I excitation energy of 8.4 eV reaches close to the Z_{002} point. On the right-hand side, the figure indicates the relation between the dispersions of the measurement arcs of the two lamps.

The separation of the plasma lamp from the measurement chamber by means of a window relieved the constraints on URu_2Si_2 experiments. Thus, the time in which high-resolution experiments could be performed prior to surface degradation was extended from less than one hour to several days. The available supply of liquid He used for cooling became the new limiting factor, becoming exhausted within 16–24 hours of measurements. Because of technical constraints, the system (measurement chamber, sample holder, sample) had to be brought up to room temperature to refill the liquid helium can. This prompted investigations of the effect of heating / cooling cycles on an already cleaved sample surface. The results, discussed in the following, are presented here to my knowledge for the first time. Together with the analysis from section 3.4.1, as of this writing they are being prepared to be published as reference [83].

3.2.1 A Typical Measurement Session

Figure 3.6 shows a typical Xe lamp measurement session on one single cleave of a sample labeled "urs11", performed across several refills of liquid helium. The chronologic succession of ARPES scans is illustrated as small colored rectangles on a black string, the *time arrow*. The meaning of the symbols on the time arrow is as follows:

- **Rectangles** with labels inside represent spectra of the reference Cu-samples (green) and of URu_2Si_2 (pink). Numbers within the labels are for internal reference. Comments on the location in k-space, the manipulator tilt angle (in degrees), and measurement settings, are shown within the pink rectangles, where appropriate.

- **Arrows** denote the cooling down (blue) or warming up (red) activity preceding the respective scan.

- **Double arrows** represent a full heat-up to or cool-down from room temperature. Time labels represent the delay to the next activity, i.e. the time spent by the sample at room temperature in vacuum.

For easier perception, the scans are grouped as follows:

- **One temperature per row**: a series of URu_2Si_2 scans at a given temperature is always grouped together and displayed on a single row. Every series is accompanied by a reference measurement (green box) with the determined temperature within. The reference scan is measured indifferently either at the beginning or at the end of the respective series.

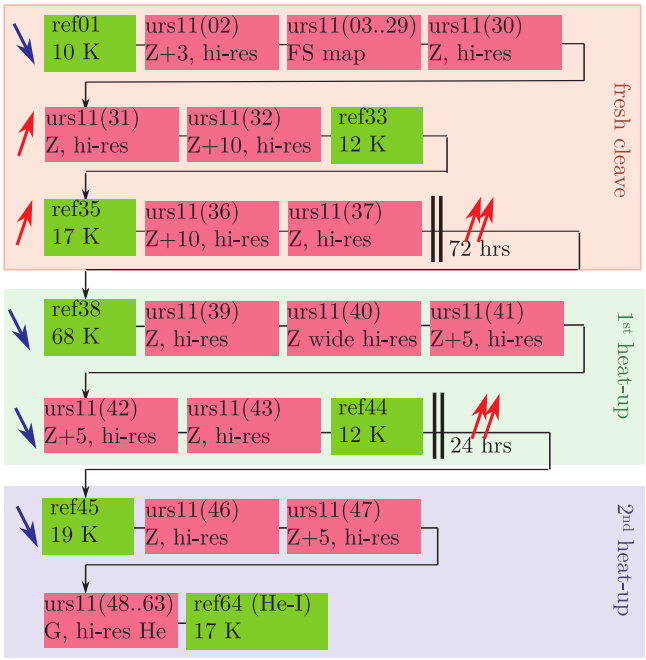

Figure 3.6: **Measurement timeline for a URu_2Si_2 sample.** Large color boxes (red, blue, green) demark individual Helium refill sessions. The first part, surrounded by a solid red border, represents a typical cooling, cleaving, and measuring session on a freshly cleaved sample. The green (blue) parts were performed after one (two) liquid helium refills, involving the heating up of the sample to room temperature in the process. The black line represents the "time arrow", showing the order in which the ARPES scans (small colored boxes with labels inside) were performed. See main text for a detailed description.

- **One cooling session per group**: measurement series are divided in three time periods, grouped together by large, colored rectangles. Each session is approximately 16 hours, limited by the amount of liquid helium available for cooling. Their succession is as follows:
  - the *fresh cleave* (red rectangle), showing a typical URu_2Si_2 measurement on a sample freshly cleaved at lowest attainable temperature;
  - the *1st heat-up* (green) is a subsequent session after one full cycle of heating up to room temperature and cooling down again 3 days later;
  - the *2nd heat-up* (blue) is another session, after one further heating & cooling cycle, 96 hours after the first session, or 24 hours after the previous cycle.

Besides "urs11", another sample, labeled "urs12", was measured involving one liquid helium refill, and thus one heat-up & cool-down cycle. Results from these two samples will be discussed in the following. In other cases, the measurement ended and the sample was recycled for a fresh cleave after the exhaustion of the first liquid helium supply.

3.2.2 Electronic Structure After a Heating-Cooling Cycle

Figure 3.7 shows "urs11" before and after a heating and cooling cycle. Panel (a) shows a nicely dispersing surface state measured in (110) orientation, below T_{HO}, during the red *"fresh cleave"* session from figure 3.6. The data is FDD-normalized. A 2nd derivative version of the same data is shown in (b). The SS fit from section 3.1 is overlaid as a red dashed line, bound at $E \approx -38$ meV. In panel (c), another 2nd derivative is shown, obtained from a scan performed during the green *"1st heat-up"* session, after one heating / cooling cycle. A structure similar to SS is appearing. It will be called "HS" (i.e. "heat-up state") henceforth. The new structure differs significantly from SS: first, it

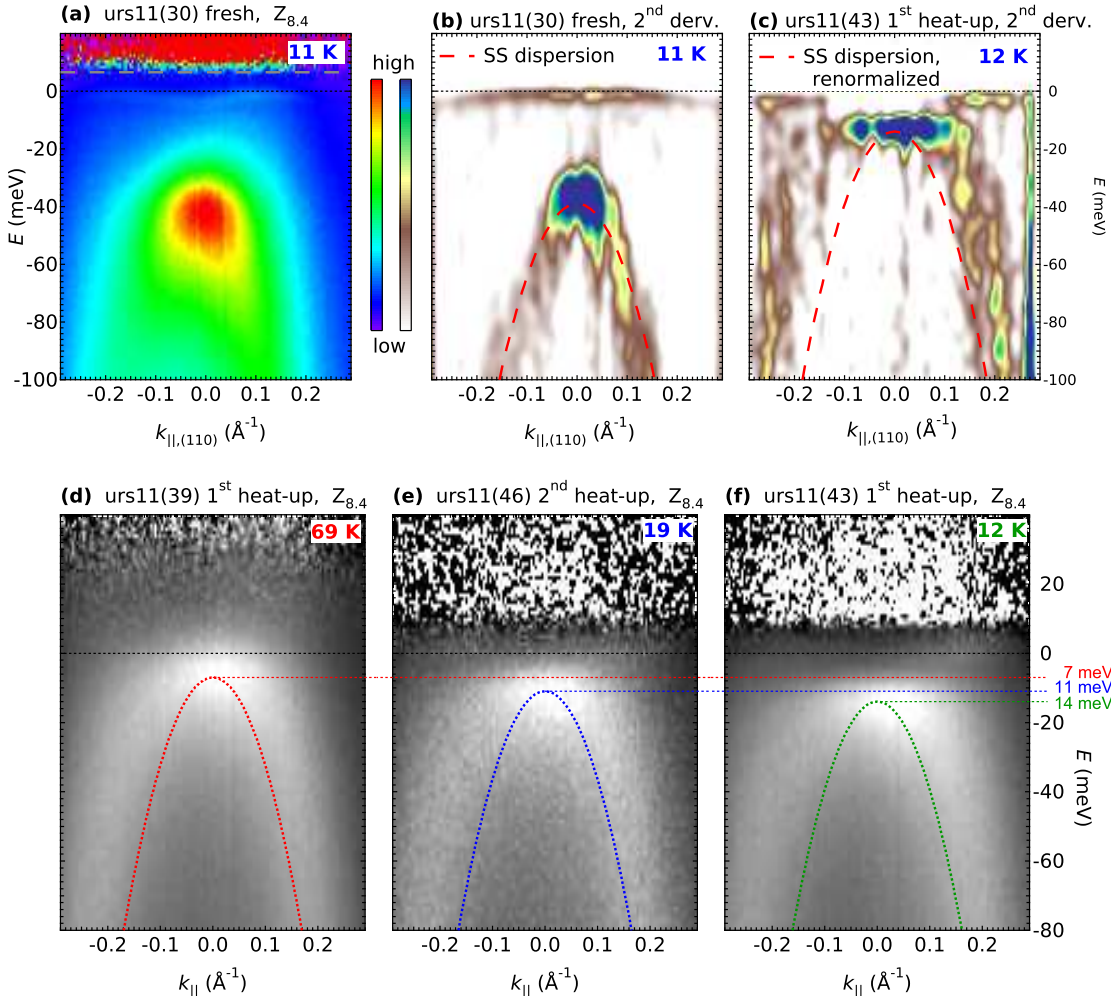

Figure 3.7: **Development of the heat-up state.** Panel (a): ARPES scan no. 30, measured on the freshly cleaved surface of sample "urs11" at $Z_{8.4}$. The data is shown FDD-normalized. Panel (b): the same data, convoluted with the 2nd derivative of a Gaussian ($\sigma_E = 10$ meV, $\sigma_k = 0.04$ Å^{-1}). Theoretical dispersion of SS (figure 3.1) is overlaid as a red slashed line. Panel (c): ARPES scan no. 43, after one heat-up and cool-down cycle, shown as a 2nd derivative similar to (b). Binding energy of the theoretical dispersion is set to $E = -13.5$ meV, the new binding energy of the intense hole-like state. Dispersion of the state differs significantly from that of SS: it is flat and heavy ($m/m_e = \mathcal{O}(100)$) close to E_F at crystal momenta $|k| \leq 0.15$ Å-1, and light ($m/m_e = \mathcal{O}(1)$) at higher momenta. Panels (d-f) show FDD-normalized ARPES data after one [panels (d,f)], respectively two [panel (e)] heat-up / cool-down cycles. In decreasing order of temperature, from left to right, HS shifts towards more negative energies. Unlike SS, this hole-like state shifts in strong dependence on temperature, without correlation to the time of exposure to residual gases.

is bound at $E = -14$ meV, much closer to E_F; then the dispersion of SS, again overlaid as a red dashed line, does *not* correspond to HS in spite of the adjusted binding energy. Instead, the upper part of the band seems rather flat. Only at energies below -50 meV does its effective mass become increasingly similar to SS.

Panels (d-f) document that HS is shifting gradually with cooling, from -7 meV at 69 K, to -11 meV at 19 K, finally reaching -14 meV below the transition temperature. The data is displayed as FDD-normalized ARPES intensity in grayscale. In all panels, a free electron hole-like dispersion with the same mass as SS is shown. The location of the peak corresponding to HS, extracted from EDCs at $k_{\|} = 0$, was chosen as the highest point of the parabolic dispersion. In spite of both SS and HS being hole-like, they are clearly of different nature. Unlike with SS, attempts to adjust the effective mass of the parabola to match the shape of HS have failed systematically.

Of particular importance seems the fact that HS does *not* shift with aging: chronological order for the three lower panels in figure 3.7 is (d), (f), (e). This differs from the order of their binding energies, which is instead related to the sample temperature. The scan succession is also proof that HS, once created by the first heating & cooling succession, is stable to further temperature cycles. This can be understood from scan 3.7(d), which was measured during in the blue *"2nd heat-up"* session of figure 3.6.

3.2.3 Heat-up State Dispersion

A systematic investigation of the HS dispersion is shown figure 3.8 using data obtained from the sample "urs12". Panels (a) and (b) show ARPES intensity maps in grayscale below and above T_{HO}. For a stricter analysis, in each EDC of a spectrum the point of maximum intensity was determined and marked on top of the corresponding ARPES panel with a cross. Polynomial fits to these marks are drawn as solid lines: red for the HO case in panel (a), blue in the PM data from (b). To assess the differences across the transition, the red line fit from (a) is also displayed in (b) as a dashed dispersion. In both cases, the hole-like band dispersion has a low effective mass, comparable to SS or CB, in the stronger bound region ($E \leq -50$ meV). Closely below E_F, the band appears dispersionless and flat at momenta between $k_{\|} = \pm 0.1$ Å^{-1}. The result is also illustrated in panels (c) and (d) as collections of EDCs, plotted in a waterfall manner. For orientation, the lines for $k_{\|}$ vectors of ± 0.1 Å^{-1} and 0.1 Å^{-1} are bold. The fitted HS dispersions are plotted as dashed lines.

In both "urs11" and "urs12", the shape of HS commends a strong resemblance with the lower part of a hybridization between a light and a heavy band. The fits suggest that the upper, heavier, flat part of the band is shifting to stronger bound states with cooling. The lateral, "fast" branches do not change within experimental accuracy. However, signal-to-noise ratio is too bad to make a clear distinction between HS shifting as a whole, or only its upper part moving, with the rapidly dispersing flanks remaining constant.

3.2.4 Systematic Behavior of the Heat-Up State

For comparison, a scan of HS using He-I excitation energy is displayed in 3.9(a) as an FDD-normalized ARPES intensity, together with the dashed dispersion from 3.8(c). Although data quality has significantly diminished—by this time, the sample had spent more than 100 hours in the measurement chamber—a structure is visible that is com-

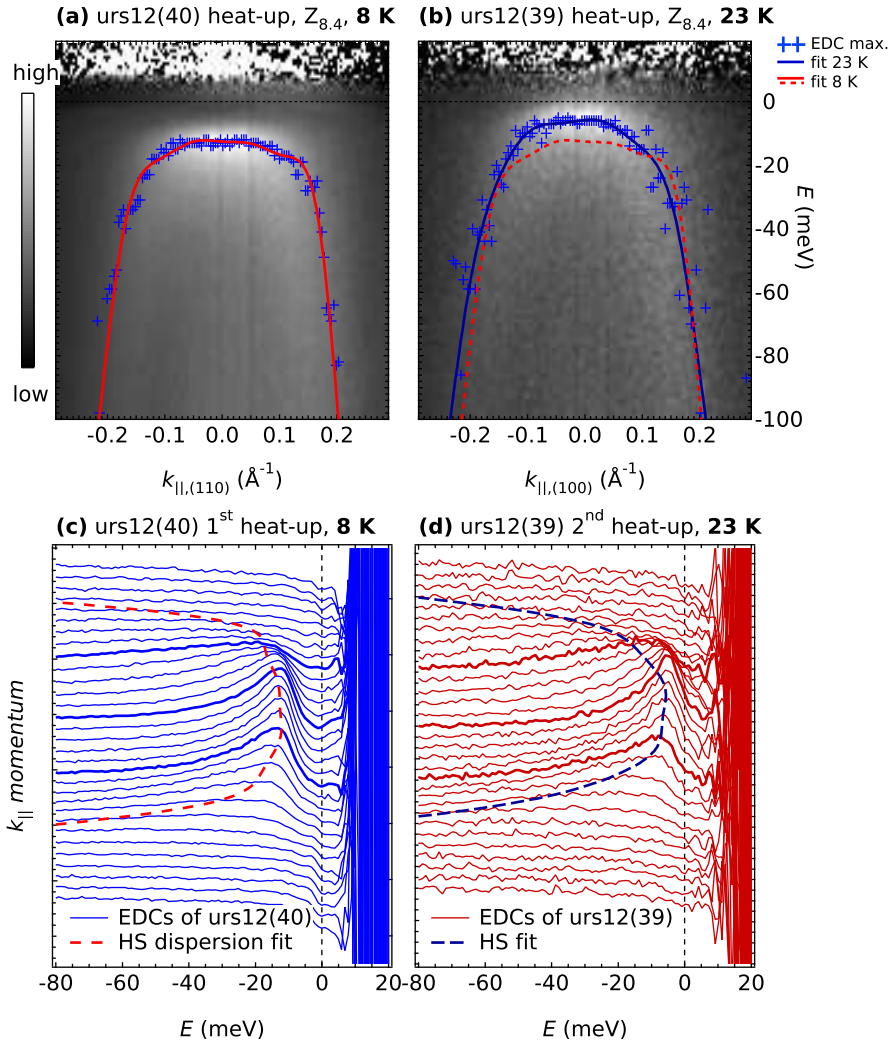

Figure 3.8: **Dispersion of the heat-up state.** Panels (a,b): FDD-normalized ARPES scans at $Z_{8.4}$ after one heat-up / cool-down cycle in a different sample (labeled "urs12") at 8 K and 23 K. For each EDC, the position of the maximum intensity is shown by cross markers. Solid lines, red in (a), blue in (b), show polynomial fits to the EDC maxima. In panel (b), the polynomial fit from panel (a) is reproduced as a dashed red line. Compared to the solid-line fit native to panel (b), the dashed line shows only a lower binding energy, remains otherwise unchanged. Panels (c,d): same data as in (a,b) shown as stacks of EDCs. Bold lines denote EDCs at $k_{\|}$ values of ± 0.1 Å^{-1} and 0.0 Å^{-1}. Dashed lines are the polynomial fits to the HS dispersion from panels (a), respectively (b). Beyond HS, heavy-fermion peaks are visible at or above E_F in the ARPES data from (a) and EDCs from (c). Similar peaks in panel (d) are difficult to detect owing to the poor signal to noise ratio.

patible with HS, and not with SS. This would suggest that the same band is available at more than one position along k_z, aiding the argument that HS may be a 2D surface state.

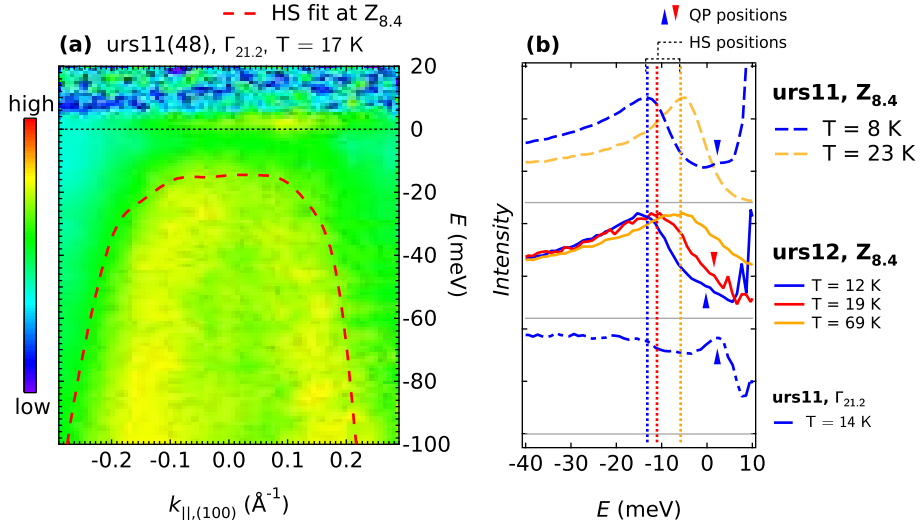

Figure 3.9: **Reproducibility of the HS dispersion.** Panel (a): ARPES scans of sample "urs11" measured with He-I$_\alpha$ at $\Gamma_{21.2}$ at 17 K. The overlaid slashed red line is a polynomial fit to HS obtained from another ARPES scan at $Z_8.4$, measured in the HO phase (figure 3.8). It matches the He-I$_\alpha$ ARPES dispersion. The weak contrast is a result of unfavorable experimental factors (see text). At E_F, the heavy-fermion peak QP$_1$ is clearly visible. Panel (b): EDCs integrated for k-values between ± 0.1 Å^{-1} from the FDD-normalized heat-up scans of "urs11" from figure 3.7 (top), of "urs12" from figure 3.8 (middle), and the scan from panel (a) (bottom). Dashed lines indicate the top-most position of HS below T_{HO} (blue), slightly above (red), and far above (orange). The filled triangles indicate the position of QP$_1$ at E_F, where detectable.

The temperature dependency of the binding energy of HS at $Z_{8.4}$ is consistent across multiple heating / cooling cycles, and also well reproducible in different samples. Figure 3.9(b) shows a summary, using data from figures 3.7 and 3.8 in the form of EDCs extracted from $k_\parallel = 0$. The legend links the different spectra to the corresponding samples. In all EDCs, the heavy QP$_1$ is marked by small colored triangles. The blue EDCs, all measured at approximately 10 K, show a peak corresponding to HS, demarked by a blue vertical dashed line. With increasing temperature, the HS peak shifts to higher energy, as indicated by the red and orange lines. Additionally, the following is observed concerning the succession of the HS binding energies:

- HS binding energies for "urs11" and "urs12" are similar around $T \approx 10$ K; this also covers the data at $\Gamma_{21.2}$ measured by the He-I lamp.
- Orange line of "urs12" at 23 K has essentially the same binding energy as "urs11" at 69 K, although the temperatures are far apart,
- but the red line of "urs12" at 19 K strongly differs from the orange line at 23 K from "urs12".

Thus, it would appear that the shifting of the binding energy stops somewhere between 19 K and 23 K. This points to modifications of the electronic structure occurring at temperatures around 23 K.

3.2.5 Conclusion

The presence of HS at Γ raises the question of whether it may be another surface state. Even if the quality of the data is rather poor, it shows that the HS does not disperse much with k_z, at least not in the ordered phase. But the argument is weak for two reasons: first, $\Gamma_{21.2}$ and $Z_{8.4}$ are precisely $1/2$ Brillouin zone apart with respect to the body-centered tetragonal unit cell in URu_2Si_2. If a symmetry transition from body-centered to simple tetragonal was involved in the HO transition, then the appearance of HS at Γ for temperatures below 17.5 K would be the natural consequence. Second, given the large effective mass of HS close to the Fermi level, a small dispersion along k_z cannot be excluded: it could easily have gone undetected, considering the poor data quality in figure 3.9(a).

In contrast, evidence that HS is a bulk state predominates. For one, the band is shifting towards E_F—the wrong direction, when compared to SS, which shifts towards stronger bound states. Then the shifting direction of HS shows no dependency on age; instead, it shifts as a function of sample temperature. Finally, HS apparently is involved in a hybridization process, similarly to QP_1 and CB, which are considered to be bulk bands.

3.3 The X-Point

Extensively discussed, the electronic properties of URu_2Si_2 are determined by the dual itinerant-localized character of the Uranium $5f$ electrons, with Kondo screening developing around $T \approx 75$ K. Band hybridizations between heavy f-electrons and light hole-like conduction bands were already shown at the X point for paramagnetic URu_2Si_2 [32].

In a body-centered tetragonal lattice, two different "flavors" of the high-symmetry point, X and X', can be probed experimentally, owing to the Brillouin zone stacking discussed in section 1.3.3. With He-I$_\alpha$ and He-II$_\alpha$ light, they can be reached at sample tilt angles of 30°, respectively 21°, as indicated by the image to the right.

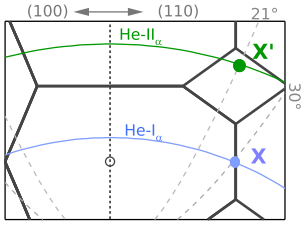

In part 3.3.1 of this section, the band structure at X, close to E_F, is examined in both the PM and the HO phase of the crystal, using high-resolution He-I$_\alpha$ ARPES data. The development of band hybridizations and a hybridization gap across the HO transition—circumstance previously not captured directly by other experiments—is revealed in the data, and backed up by a simple phenomenologic model. The finding represent a major ingredient in the main message of this thesis: the "hidden-order" developing on top of a pre-formed Kondo lattice.

In part 3.3.2, complementary wide energy range scans at X and X' will be discussed. To attest beforehand, in this particular experimental setup (section 1.3.2), the rapidly degrading signal of the He lamp does not permit definitive insight concerning a possible symmetry change from body-centered to simple tetragonal—a topic vigorously pursued during the 3$^{\text{rd}}$ generation of research (section 1.2.5). But none the less rewarding, the wide-range data at X offers opportunity to compare the experimental band structure with theoretical calculations.

3.3.1 High-Resolution Features

The first part of the following discussion concerns band hybridizations between a heavy and light band at X, aswell as the resulting Fermi surface (FS). It has not been previously published. Based on high-resolution He-I$_\alpha$ data measured by Dr Andreas Nuber and myself in 2009, it is elaborated here for the first time. The second part focuses on a systematic hybridization analysis of the same data using a phenomenological model. It is based on the data analysis from C. Bareille's MSc thesis [60], extended here in several experimental aspects I deemed important. In a reduced form, the findings were also published as part of reference [77].

Band hybridization at X He-I$_\alpha$ ARPES scans with a resolution of $\Delta E = 5.18$ meV were performed at various temperatures around the HO transition. Figure 3.10 shows color plots of the FDD-normalized data. The scans were performed with samples tilted by 30° along the $(1\bar{1}0)$ direction. The momentum axis of the plots designates (110), the direction parallel to the X plane in reciprocal space. The stark difference in intensity between positive and negative momentum coordinates is attributed to matrix elements. Starting at 12 K in panel (a), a light hole-like dispersion is visible below E_F, and a flat structure with electron-like dispersion at and above the Fermi level. The highest point of

the light band is $E = -8$ meV, below E_F. At that energy it displays a very high effective mass, appearing to be the result of a hybridization with the heavy band. The lowest part of the upper band is at $E \approx -2$ meV. A hybridization gap separating the two is observed as a region of strongly reduced intensity, at momenta between $k_{\|} = \pm 0.14$ Å^{-1}, and energies from -6 meV to -3 meV. Dashed vertical lines at 0.195 Å^{-1} indicate the boundaries of the X plane, ruling out the crossing of Brillouin zone limits as a trivial reason for the band hybridization.

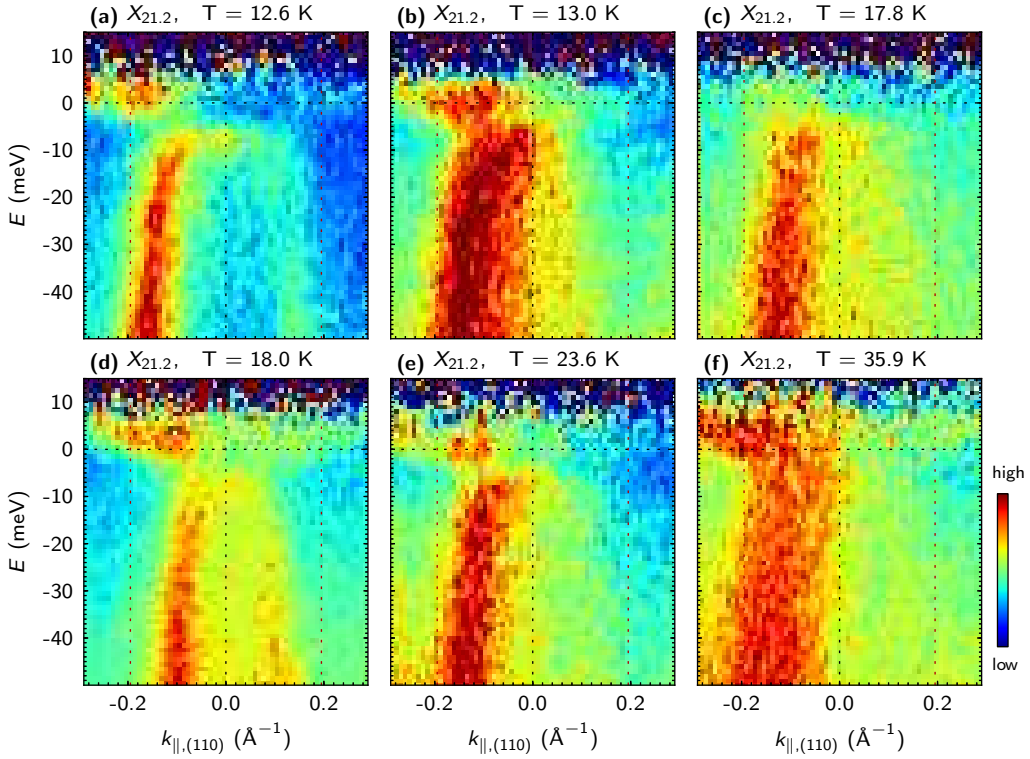

Figure 3.10: **T-dependent high-resolution ARPES intensity maps at X.** The data was measured using He-I$_\alpha$ excitation energy in the HO phase in (a,b), around the phase transition in (c,d) and in the PM phase in (e,f). Vertical dashed lines at $k_{\|} = \pm 0.195$ Å^{-1} denote the boundaries of the X plane. A rapidly dispersing hole-like state hybridizing with a heavy electron band ($m/m_e \approx 100$), aswell as the hybridization gap at $k_F \approx 0.14$ Å^{-1}, are visible below and above T_{HO}. At 35 K, a hybridization gap is not discernible, possibly owing to thermal broadening.

With increasing temperature in subsequent panels, the appearance of the bands changes slightly, owing to temperature broadening and experimental noise. The hybridization gap, however, remains clearly visible well into the PM phase, for example in panels (d) and (e), at 18, respectively 24 K. At 35 K, in panel (f), both bands are still observed, but whether the hybridization has ceased or the gap is just blurred by thermal broadening is impossible to say within the limits of the experimental conditions.

The structure of the Fermi surface A systematic analysis of the FS shape is mediated by figure 3.11. Panels (a) and (d) show two $k_{\|,\mathrm{det}} \times k_{\|,\mathrm{tilt}}$ intensity maps at $E = 0$,

for temperatures below, respectively above T_{HO}.

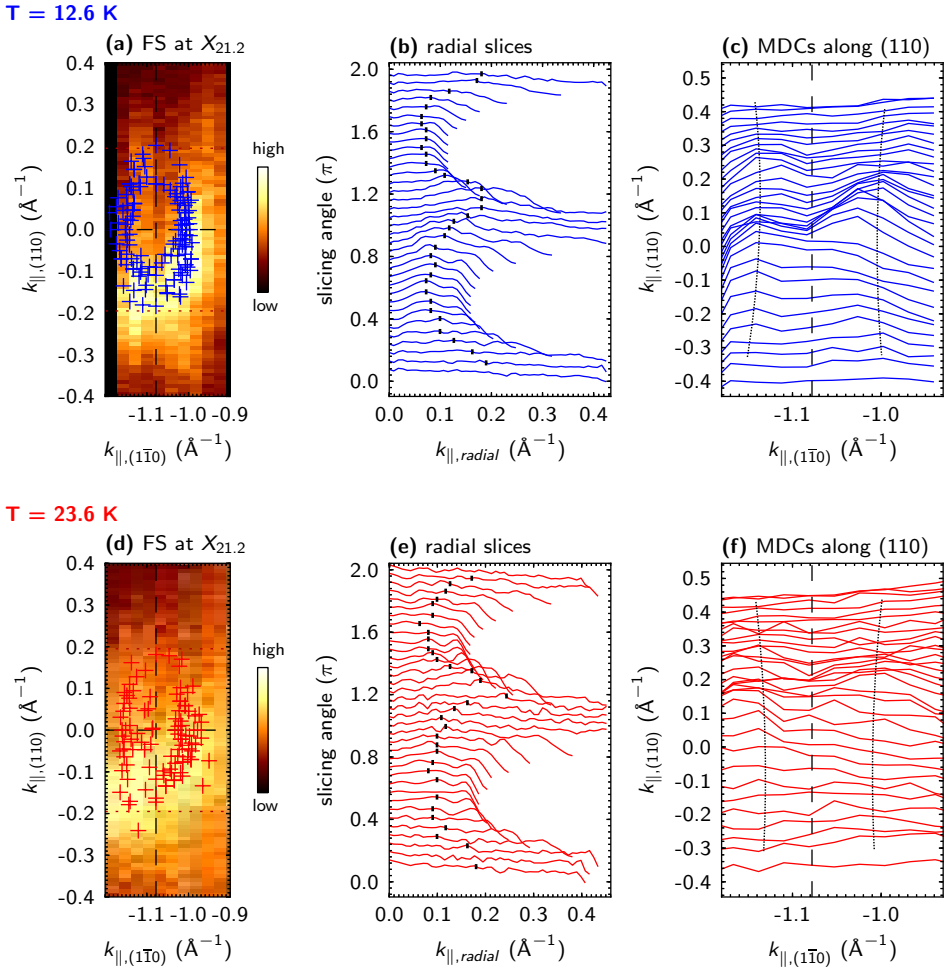

Figure 3.11: **Fermi surface cuts at X.** The data was measured with He-I$_\alpha$ energy in the HO phase (a-c) and the PM phase (d-f). Stacked MDCs integrated from high-resolution ARPES scans at -4 meV $\leq E_{\mathrm{kin}} \leq 1$ meV are shown in panels (a) and (d), respectively. Overlaid crosses demark the positions of intensity peaks obtained from radial MDCs taken every 10°, as displayed in panels (b) and (e). Panels (c) and (f) show MDCs parallel to the measurement tilt direction, with a double-peak structure dispersing parallel to (110). This suggests that the idea of an oval BCT-symmetric pocket around X may be misleading (see main text).

MDCs created by slicing the data from the X point radially every 10° are shown in panels (b) and (e). Maxima in the MDCs, denoted by black dashes, belong to maximum intensity in the FS maps of (a) and (d). This procedure was repeated for all available data sets. The positions of the maxima for all data sets are shown as blue (HO phase), respectively red (PM phase) crosses in the corresponding FS maps.

The figure demonstrates three things. First, a 2-fold symmetric structure of the FS

map is suggested, elongated along (110) with respect to $(1\bar{1}0)$. The size of the oval is (0.2 ± 0.1) Å^{-1} in the $\Gamma - \Gamma$ direction, and (0.35 ± 0.15) Å^{-1} along $Z - Z$. Second, the FS does not change across the HO transition within the experimental error, which can be easily inferred from the distribution of the crosses on top of panels (a) and (d). Third, the straight-forward idea of an oval pocket around the X point appears too simple. This is suggested not only by the unusually large errors on the shape of the FS, but also by the intensity distribution in the plots themselves: in the corners of the panels (a) and (d), for example around $(k_{\parallel,(110)}, k_{\parallel,(1\bar{1}0)}) = (-0.3, -1.0)$ Å^{-1}, signal intensity is drastically increased. This could be attributed to noise if it weren't for the fact that the same intensity increment is noticed at all 4 corners, albeit more difficult to observe in the upper part of the images owing to matrix elements. To illustrate this, panels (c) and (f) in figure 3.11 show MDCs created parallel to the $(1\bar{1}0)$ directions of the data from panels (a) and (d). Shoulders at momenta of approximately $X \pm 0.08$ Å^{-1} disperse straight from the top to the bottom of the $(1\bar{1}0)$ axis, without regard for the presumably oval structure of the FS. They are systematically discernible in all MDCs in spite of the poor signal quality.

The fact that the peaks in (c) and (f) are *not* well reproduced in the radial slices from (b) and (e) could indicate that there are two other FS sheets along the $(\Gamma) - X - (\Gamma)$ direction, dispersing at a distance of approximately 0.08 Å^{-1} left and right of the X plane. But this conclusion cannot rest solely on the data at hand. Instead, it will be formulated more confidently in reference [76], based on higher-resolution synchrotron data. For now, considering only the He-I$_\alpha$ spectra presented here, the interpretation of a 2-fold symmetric, oval Fermi surface at X, which is *not* changing its shape across the HO transition, appears most likely.

Systematic temperature dependency of the gap and the Fermi surface A comparative analysis of the size of the hybridization gap across the HO transition is presented in figure 3.12. Panel (a) shows data obtained from a number of ARPES scans as EDCs integrated over the "inner" and "outer" momentum areas, i.e. around the highest point of the lower band, at momenta -0.05 Å$^{-1} \leq k_\parallel \leq 0.05$ Å^{-1} (blue), and around the lowest point of the upper band, with 0.2 Å$^{-1} \leq k_\parallel \leq 0.15$ Å^{-1} (red). In all data sets, two peaks are detected systematically at the same positions: $E_l \approx (-8 \pm 1)$ meV and $E_h \approx (1 \pm 1)$ meV. They belong to the lower, respectively the higher band, revealing a gap $\Delta_x \approx (9 \pm 2)$ meV that is independent of temperature.

MDCs of the Fermi surfaces, integrated in tilt and detector direction, are shown in panels (b) and (c). Black crosses demark the position of the peaks, with the width of the crosses representing the experimental uncertainty. In spite of the noise, the data remain well compatible with the conclusion that the oval-shaped FS of approximate size 0.2 Å$^{-1} \times 0.3$ Å^{-1} does not change across the HO transition.

Phenomenological modeling of the hybridization gap Figure 3.13 shows a phenomenological fit to the data. The band dispersions in two ARPES data sets, one below and one above T_{HO}, were used to adjust the parameters of a simple hybridization model as described for example in [1]:

$$E'_{1,2} = E_1 + E_2 \pm \frac{\sqrt{(E_1 - E_2)^2 + 4|V_{cf}|^2}}{2} \tag{3.1}$$

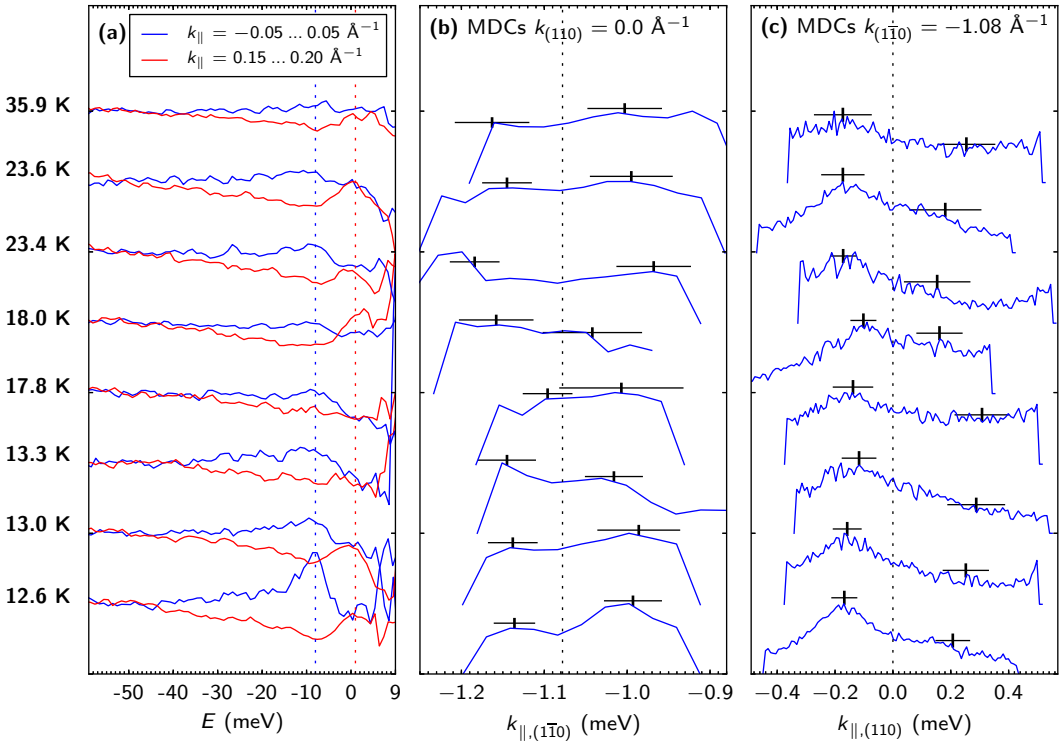

Figure 3.12: **T-dependent evolution the bands at the X-point.** Panel (a) shows EDCs integrated in the region of the lowest binding energy of the upper band ("outer" area, red lines) compared to EDCs integrated at the highest binding energy of the lower band ("inner" area, blue). The gap of magnitude $\Delta_X \approx 9$ meV is highlighted by the blue and red dashed lines and does not change across the phase transition. MDCs of the Fermi surface along the sample tilt direction and the analyzer direction are shown in (b) and (c). Black crosses demark positions of the Fermi sheets. Width of the crosses represent errors of the peak locations estimated from the MDCs and the 2D Fermi surface maps. Within the experimental limits, no temperature dependency is observed.

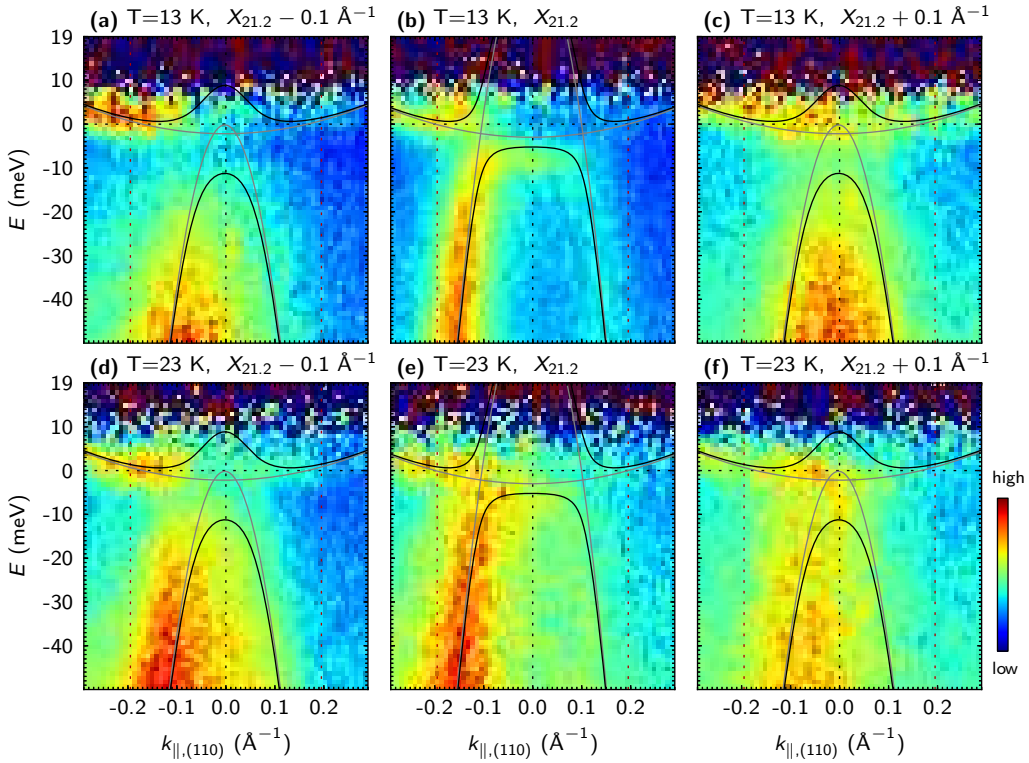

Figure 3.13: **Fitting of the band hybridization at X.** ARPES intensity plots at $X_{21.2} - 0.1$ Å^{-1}, $X_{21.2}$ and $X_{21.2} + 0.1$ Å^{-1} [panels (a-c)] in the HO phase, overlaid with parabolic free electron dispersions of a light hole-like ($m = m_e$) and a heavy ($m/m_e = 50$) electron band. The dispersions are shown before (grey) and after (black) hybridization with a potential $V_{\mathrm{cf}} = 10$ meV. Panels (d-f) show similar data in the PM phase. Fit parameters and hybridization potential remain unchanged.

In each case, the full three-dimensional $k_{\parallel,\mathrm{det}} \times k_{\parallel,\mathrm{tilt}} \times E$ data set was used for fitting. As a lower band, a paraboloid free electron dispersion with effective mass $m = m_e$ was used. The heavy band required an effective mass of $m \approx 50 m_e$ to match the experimental data.

Using a hybridization potential of $V_{\mathrm{cf}} = 10$ meV, not only the data at $k_{\parallel,(110)} = X + 0$ Å^{-1} was reproduced [panels (b) and (d)], but also for momentum values of $X \pm 0.1$ Å^{-1} [panels (a) and (d), respectively (c) and (f)]. The initial, non-hybridized bands, are shown on top of the ARPES scans as grey lines. Black lines represent the hybridized dispersions. A systematic analysis of the hybridization parameters, using data at several temperatures between 10 K and 35 K, was performed by C. Bareille. A summary of results is shown in 3.14, based on [60]. In contrast to my analysis, the hybridization parameters were fitted in [60] only to the central ARPES scan at $k_{\parallel,(1\bar{1}0)} = X + 0$ Å^{-1}, not to the full 3D data.

Regardless of the fitting method, the results are essentially the same, certifying a light hole-like band of relative mass $m/m_e = -1.2 \pm 0.3$, a heavy band with $m/m_e = 60 \pm 20$, and the hybridization potential of (11 ± 3) meV, all unchanged across the HO transition. The gap size of $\Delta_x \approx 10$ meV in my fit analysis, or (11±2 meV from [60], matches perfectly with the direct experimental result from figure 3.12. Thus, this simple phenomenological approach robustly estimates the interactions between the light hole-like and the heavy

electron band at X.

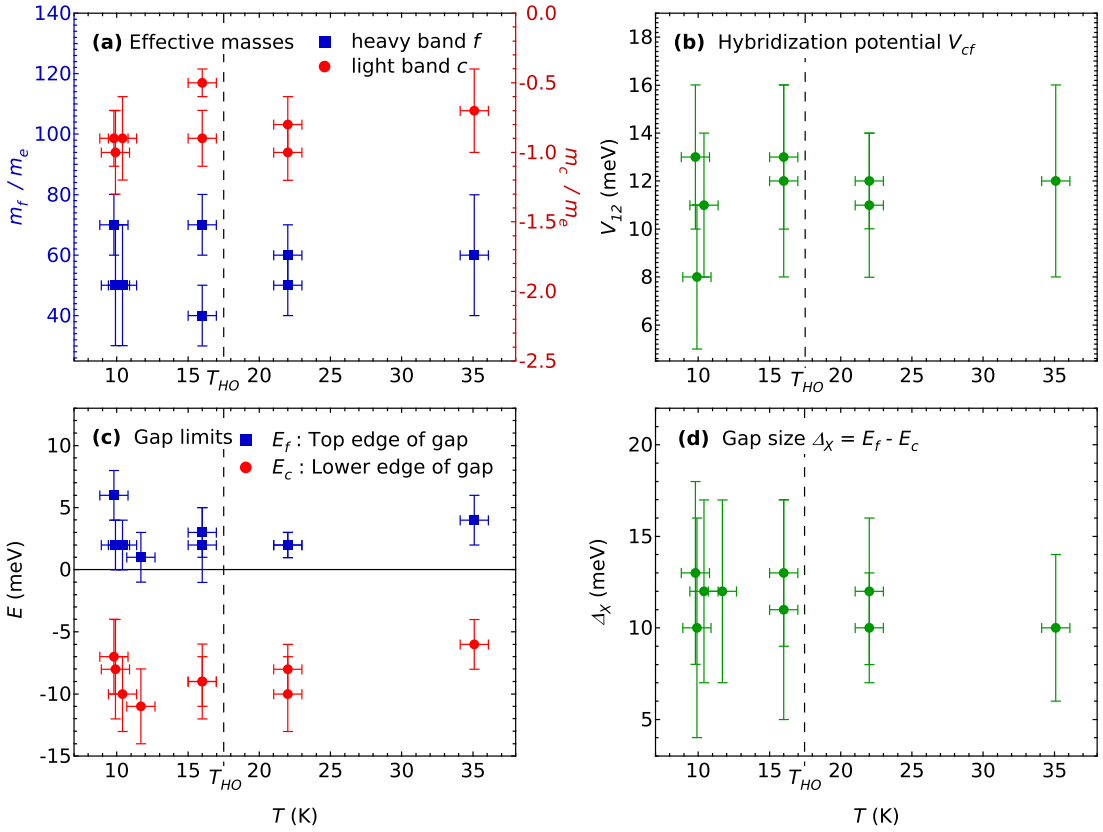

Figure 3.14: **Summary of the band hybridization at the X point.** Created on the basis of the data analysis of Cedric Bareille [60]. Panel (a): Effective masses $m/m_e \approx 1$ for the light (red) and $m/m_e \approx 60$ for the heavy (blue) band, in dependency of measurement temperature. The bands are hybridizing with a potential $V_{\mathrm{cf}} \approx 11$ meV displayed in (b). The hybridized bands have a lowest (blue), respectively highest (red) energy as indicated in (c), giving rise to a hybridization gap $\Delta_x \approx 10$ meV constant across the HO transition, as displayed in (d). *Figure based on data analysis from [60].*

3.3.2 Wide Energy Range Scans

Scans over a wider energy range at X, similar to the data at $\Gamma_{21.2}$ from section 2.2, augment the information about the electronic structure. Local density approximation (LDA) density functional theory calculations exist for the band structure in the PM phase [29]. Concerning the phase transition itself, recent dynamical mean-field theory (DMFT) models based on the HO / AF adiabatic continuity offer concise predictions for the band structure at X and X' [51, 69]. They will be tested against the wide-range ARPES scans in the following.

The "band zoo" at the X-point Figure 3.15 shows the band structure with medium resolution ($\Delta E \geq 10$ meV) over an energy range that reaches up to 2.5 eV below the

Fermi level. In each case, the data was obtained up to several hours after the fresh cleave of a sample, leading to a diminished contrast and an effective resolution much lower than the nominal 10 meV.

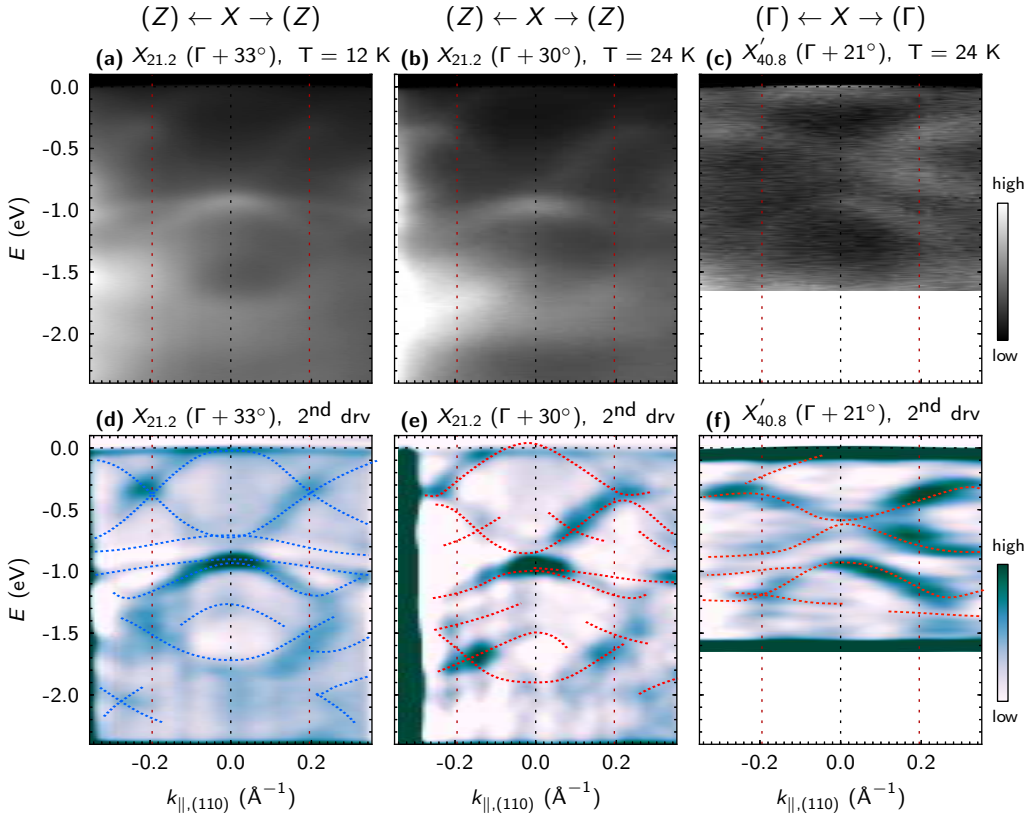

Figure 3.15: **Wide energy range, angle-resolved data of the X-point.** Panels (a-c) show grayscale AREPS intensity of X and X' (see text), covering an energy range of up to 2.8 eV below the Fermi level. The scans along the $(Z)-X-(Z)$ momentum direction were performed using He-I$_\alpha$ light at 12 K in (a), and at 24 K in (b). For the $(\Gamma)-X-(\Gamma)$ direction, displayed in (c), He-II$_\alpha$ light was used at a sample temperature of 24 K. Panels (d-f) show the same data as 2$^{\text{nd}}$ derivative, with higher intensity representing band peaks. Dashed overlays represent hand-traced band dispersions as guides to the eye. The red vertical dashed lines represent the would-be boundaries of the diamond-shaped X plane. Along $(Z)-X-(Z)$, in panels (a,b,d,e), band foldings are visible close to the Brillouin zone boundaries, while along $(\Gamma)-X-(\Gamma)$, panels (c,f), most of the foldings disappear.

In the figure, vertical dashed lines demark key positions along the $k_\parallel$ coordinate. The black line is at $k_\parallel = 0$, red lines indicate the positions $k_\parallel = \pm 0.195$ Å^{-1}. For panels (a) and (b), where the momentum axis runs along $(Z)-X-(Z)$, this corresponds to the Brillouin zone boundaries at the corners of the X plane. The first thing to notice are strong differences in intensity between the left and the right image halves, owing to transition matrix elements. For better contrast, the 2$^{\text{nd}}$ derivative of the same data is shown in panels (d-f). Darker regions correspond to minima, representing the location

of bands in the original data. Abstract bands, traced by hand similarly to section 2.2, are shown on top. The band tracing procedure was repeated for a large number of scans (approximately 30 in total) at X and X', at different temperatures in the HO and PM phase.

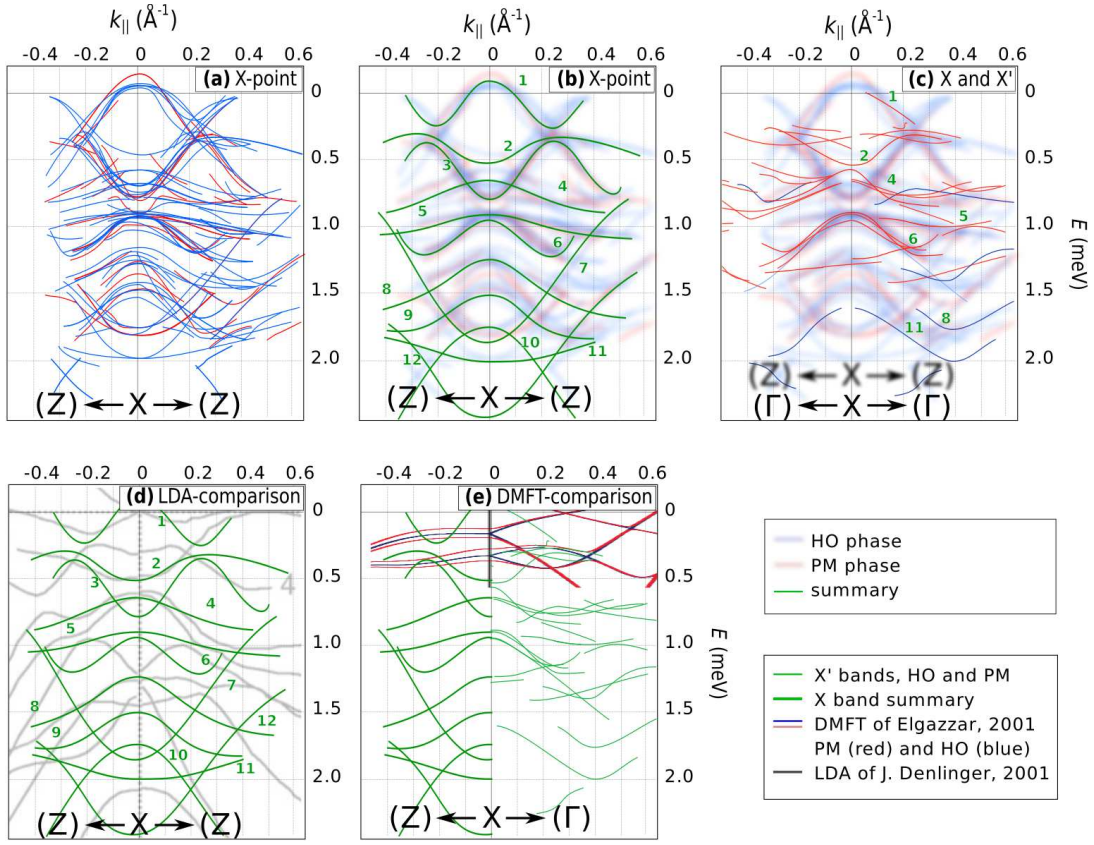

Figure 3.16: **Experimental band struture at X compared to LDA and DMFT calculations.** Panel (a:) hand-traced bands at the X point in the PM (red) and HO (blue) phases, created as demonstrated in 3.15(d-f). No significant differences are detectable across the HO phase transition. Panel (b): bands from (a), displayed more faintly and blurred, overlaid with a simplyfied "summary" view (green) of the bands. Panel (c): bands from (a), blurred and semi-transparent, overlaid with band traces measured at X' with He-I$_\alpha$, with the momentum coordinate along the $\Gamma - \Gamma$ diagonal. Panel (d): comparison of the measured band structure at X with LDA calculations of paramagnetic URu_2Si_2 from [32]. Panel (e): comparison of the band structure at X and X' with corresponding DMFT data from [51] in the PM (red) and HO (blue) phase.

Putting together all available bands yields a fairly consistent impression of the band structure at the X point. This is shown in figure 3.16. In panel (a), the red (blue) lines correspond to bands from scans at X above (below) T_{HO}. There are no detectable changes across the HO phase trantition. This justifies the attempt to distill a unified band structure at X to match both the blue and red lines. The result is shown in panel (b) as green lines, with the band structure from (a) shown as a blurred background for orientation. In panel (c), the experimental band structure at X', measured along

$(\Gamma) - X - (\Gamma)$, is plotted as thin lines—red for the HO, blue for the PM phase. The bands from (a), dispersing along $(Z) - X - (Z)$, are shown here as blurred lines, too.

Comparison with theoretical calculations Panel (d) in figure 3.16 shows the experimental bands as green lines overlaid over calculations of Denlinger *et al.* [29]. Good agreement is found close to E_F for bands 2–5, especially for momenta close to $k_{\|} = 0$. The folding momenta for bands 1–3, and for stronger bound states ($E \leq -1.0$ eV, bands 7 and 8) also agree. In general, the experimental bands have a tendency of being heavier than the calculated ones. Binding energy for stronger bound states, e.g. band 10, seems underestimated by $\Delta E \approx 1/2$ eV.

Comparison with DMFT [51, 69], attempted in panel (e), is difficult owing to a very limited energy range of the theoretical band dispersions. However, the calculations offer band structure predictions for both the $(Z) - X$ and the $X - (\Gamma)$ directions. Red and green lines represent DMFT predicted bands for the PM, respectively the HO phase. The experimental bands dispersing along the $X - (\Gamma)$ direction are shown as thin green lines, reproduced from the red bands in panel (c); for the $(Z) - X$ direction, the same green bands as in panels (b) and (e) are shown. A small degree of agreement is conceivable in $X - (\Gamma)$ direction, for example in the heavy dispersions close to theenergy $E \approx -0.4$ eV. Otherwise, perhaps due to the restricted energy range area of the available calculations, no agreement with experiment is found. This holds especially for the $(Z) - X$ direction, where heavy hole-like bands that could match the dispersion suggested in the calculations (e.g. at -0.2 eV and -0.4 eV) would occur only close to -1 eV in the experimental data. Further, the heavy e-like bands that participate in the hybridization discussed previously (section 3.3.1), are not predicted at all.

To conclude, band dispersions based on DMFT calculations mis-estimate the binding energies by at least half an order of magnitude. The theory systematically lacks the heavy band masses observed experimentally, apparently focusing on itinerant electronic features only. Further, none of the band splittings predicted in theory are observed experimentally, although this could be a consequence of the limited data resolution.

3.3.3 Conclusion

A hybridization between a light hole-like and a heavy ($m/m_e \approx 50$) band with a visible gap of 10 meV was detected at the X point. Changes do not occur either in the band structure nor in hybridization parameters across the HO transition. This is a robust result supported both by high-resolution experimental data and by theoretical considerations. The hybridization is therefore not related to the HO. Instead, its properties remain unchanged below $T \approx 35$ K. The pressing question then becomes: what *is* the origin of the hybridization? The border of the Brillouin zone is, even considering the large error bars, too far away to matter. Instead, features of a coherent Kondo lattice were demonstrated in URu_2Si_2 by momentum-integrated experimental methods already at temperatures around 100 K [24, 26, 59, 63]. Consequently, the presented data could be the first momentum-resolved evidence that the lattice becomes fully coherent, band hybridizations occur, and an energy gap of 10 meV opens already above the HO transition temperature.

From the shape and size of the Fermi surface, and the wide energy range band structure, the question about a possible transition to a simple tetragonal lattice across the HO

cannot be settled. Issues like the parallel shoulders in MDCs from figure 3.11(c) suggest a more complex FS structure, beyond the capabilities of the He-based laboratory setup. The data suffers from the limits imposed by a rapidly degrading surface.

Comparison of experimental bands with LDA and DMFT calculations show that the resemblance between theory and experiment is better for rapidly dispersing features than for heavy bands. For example, not even the existence of the heavy band at E_F is predicted, let alone its key parameters. While expected for LDA, which does not capture correlation effects (and thus quasi-particles), this is somewhat of a surprise for the DMFT-based calculations. The latter miss essential heavy band structure elements by at least half an order of magnitude. This idea is significantly extended and refined by following research of the Paris / Würzburg group in references [75, 76].

3.4 The "Hidden-Order" on Top of a Coherent Lattice

Heavy quasi-particles have been shown by ARPES and STM to participate in the Fermi surface instability that leads to the HO phase. This suggests that the instability is caused by the interaction between such heavy fermions and a band of light electrons (sections 1.2.4 and 2.3). In the previous section, high-resolution data at the X point extended this view by the crucial aspect that the HO develops in conjunction with band hybridizations that remain unchanged across the transition.

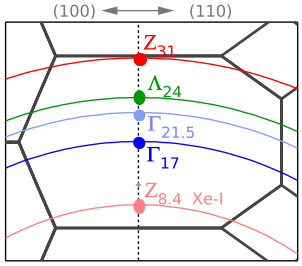

In this section, a double heavy-fermion feature is presented, observed at various high-symmetry points along the k_z axis of URu_2Si_2. The thumbnail image to the right gives a quick overview over the locations in reciprocal space explored in the following. The data was gathered using He-I$_\alpha$, Xe-I, and synchrotron radiation as excitation energies. Although officially first reported by Yoshida *et al.* in 2012 [74] at Z only, the structure was independently detected by the Paris / Würzburg group already in 2010 using the Xe-I light source. The data remained unpublished until 2013, when a better understanding of its origins and the role it plays in the HO phase transition emerged in the context of reference [61]. In this section, its evolution up to temperatures close to the onset of the Kondo screening is investigated, showing its origin in the formation of the coherent lattice and its existence at various high-symmetry points besides Z. The electronic structure around E_F arises from the hybridization of the hole-like CB (section 2.3) with an itinerant heavy-electron band in the Kondo-screened state, far above 17.5 K. The transition to the HO phase then results from a further light electron-like band dropping below E_F. The latter interacts with the Kondo-lattice feature and pushes down its f-like part, opening up a gap. The pre-existent coherent lattice of heavy-fermions in URu_2Si_2 thus plays a major part in the transition to the HO state. Finally, to describe the electronic structure changes at multiple points, a phenomenologic model involving three hybridizing bands is proposed.

3.4.1 Another High-Mass Dispersion: QP$_2$

QP$_2$ below and above the transition temperature Figure 3.17 shows data obtained using the Xe-I excitation energy of 8.4 eV. High-resolution ARPES measurements, obtained at $Z_{8.4}$ in (110) direction, are shown as waterfall plots of EDCs in panels (a) and (b). They were created by binning and slicing ARPES data at 10, respectively 68 K, at intervals of 0.01 Å^{-1} in the $k_\parallel$ direction. In the HO phase, the data shows the heavy quasi-particle band QP$_1$. It is bound at energy $E = -3$ meV below E_F, folding at $k \approx \pm 0.16$ Å^{-1}. A light hole-like dispersion similar to CB, parallel to SS (section 3.1), is also being observed. An additional feature, QP$_2$, appears bound at $E = -10$ meV below E_F: a flat band of resolution-limited width, stretching parallel to QP$_1$ at momentum coordinates between ± 0.15 Å^{-1}. First reported by laser ARPES, QP$_2$ was interpreted as a dispersionless "satellite" of QP$_1$ by Yoshida *et al.* [74]. In stark contrast, a prime feature of QP$_2$ here is its clearly visible dispersion: the hole-like intensity left and right of SS, introduced as CB at the $\Gamma_{21.2}$ point, is at $Z_{8.4}$ in fact a band that has a high effective mass at the top, but is rapidly dispersing with an effective mass similar to SS

($m/m_e \approx 1.5$) for momenta $|k_\parallel| \geq 0.15$ Å^{-1}. Its shape suggests that it is the lower part of a hybridization between a heavy f-state and a light hole-like state. At 68 K, in panel (b), the electronic structure is very similar to the HO case. Close to the lattice coherence temperature of URu_2Si_2, the QP_2 band shows the same peculiar shape typical for a hybridized band: flat close to $k_\parallel = 0$, rapidly dispersing at high momenta. This poses another difference to the data reported by laser ARPES, where the band could not be observed above T_{HO}.

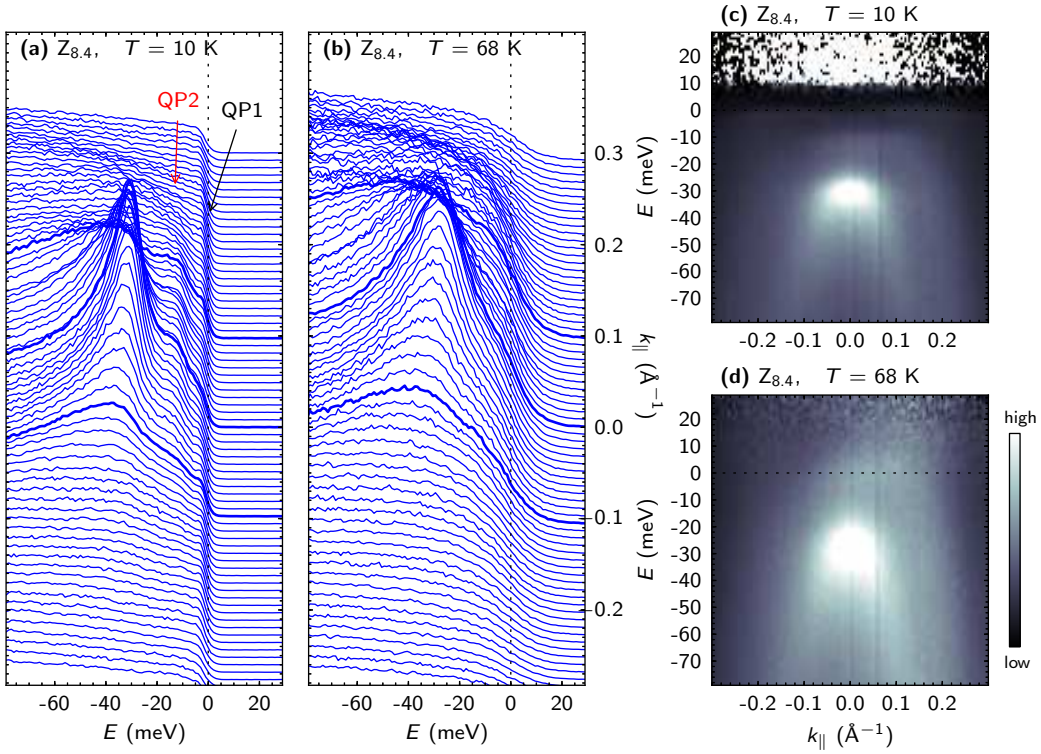

Figure 3.17: **A second heavy-fermion dispersion parallel to QP_1.** Panels (a,b): EDC stacks of ARPES raw data at Z8.4 , using Xe-I photons, at 10 K and 68 K respectively, measured in (110) direction. The red and black arrows point to the bands labeled QP_1 and QP_2. The $k_\parallel$ scale at the right-hand side scale refers to the zero of the spectra. The bold EDCs correspond to $k_\parallel = 0, -0.1$ and 0.1 Å^{-1}. Panels (c, d): FDD-normalized ARPES intensity plots of the same spectra. QP2 is clearly visible as a hole-like dispersion parallel to SS at both temperatures. In the HO phase (c), QP_2 appears bound at $E = -13$ meV, repelled by QP_1 at $E \approx -3$ meV. In the PM phase, panels (d), QP_2 disperses up to the Fermi level, traces of its broadened intensity being easily discernible in the region $E_F \pm 10$ meV.

The same data is shown in panels (c) and (d), as FDD-normalized ARPES intensity in gray scale. In the thermally populated area at and above E_F, QP_2 is seen dispersing from a higher binding energy for 68 K than for 10 K, but otherwise unchanged. Whether QP_1, essentially a flat dispersion at 10 K, merges with QP_2 or outright disappears at 68 K, is not discernible from the data.

Connection between QP_2 and HS A very similar dispersion, reminiscent of a hybridization between a heavy and a light band, was already presented in section 3.2 as the "heat-up state". Figure 3.18 shows a systematic comparison between HS and QP_2 using EDCs from samples "urs11" and "urs12" as waterfall plots. For each sample, two different scans are presented at the same temperature: one taken on a freshly cleaved surface, the other after a heating & cooling cycle. Thus, QP_2 and HS are visible at similar temperatures and on exactly the same sample, allowing a direct comparison to one another. For easier grasping, the figure is organized as follows:

- **Line colors** of the EDCs indicate the sample orientation and temperature:
  - blue is "urs12", (110) orientation, HO phase;
  - red is "urs12", (110) orientation, PM phase;
  - green is "urs11", (100) orientation, HO phase (data for the normal phase is not available for this sample).
- **Line style** of the EDCs indicates whether the sample was freshly cleaved (solid) or has undergone any heating & cooling cycles (dashed).

All other plot parameters are kept constant across all panels: the binning in momentum direction is 0.02 $Å^{-1}$, bold EDCs denote momentum coordinates $k_{\|} = 0$ and ± 0.01 $Å^{-1}$, data is normalized to the maximum intensity point. The hole-like dispersion of HS, as fitted in section 3.2, is plotted using a bold dashed line on top of both the freshly cleaved and the heat-up spectra. It fits perfectly with the shape of QP_2 for all directions and temperatures.

With all the essential features of QP_2 matching to HS, starting from its binding energy close to E_F down to the typical dispersion along the sides of SS, the data offers compelling evidence that QP_2 and HS are the same band. Conversely, the conclusion from section 3.2 that heating up the sample removes SS, effectively exposing the bulk HO related band structure, is also re-confirmed. The data in figure 3.18 also suggests that whatever causes the T-dependent shifting of HS, it is apparently limited to temperatures slightly above T_{HO}. This is seen comparing panels (e) and (f), where the binding energy of HS at 23 K matches that of QP_2 at 68 K without any modifications.

Evolution of QP_2 along the perpendicular momentum axis Figure 3.19 presents the development of QP_1 and QP_2 across the HO phase transition at different photon energies. The data was collected at the 1^3 BESSY beamline. Samples were oriented in the (110) direction with respect to the analyzer slit. The top row shows data in the HO phase, the bottom row displays the PM state. Temperatures on the left represent thermocouple readings. From left to right, the columns show the $\Gamma_{17}, \Gamma_{21.5}, \Lambda_{24}$ and Z_{31} points. Corresponding point labels are shown for each column along the top figure axis. $\Gamma_{21.5}$ is essentially the same point as $\Gamma_{21.2}$, the point reachable by the He-I_α lamp.

The ARPES data is displayed as waterfall diagrams of EDCs integrated at equidistant intervals of 0.0167 $Å^{-1}$ along the momentum axis. An FDD normalization was performed only on the data from the paramagnetic state. For the HO data, owing to the very narrow Fermi level at 1 K, the procedure is not reliable and offers close to no benefit considering the narrow range above E_F within which meaningful data can be obtained. Bold lines

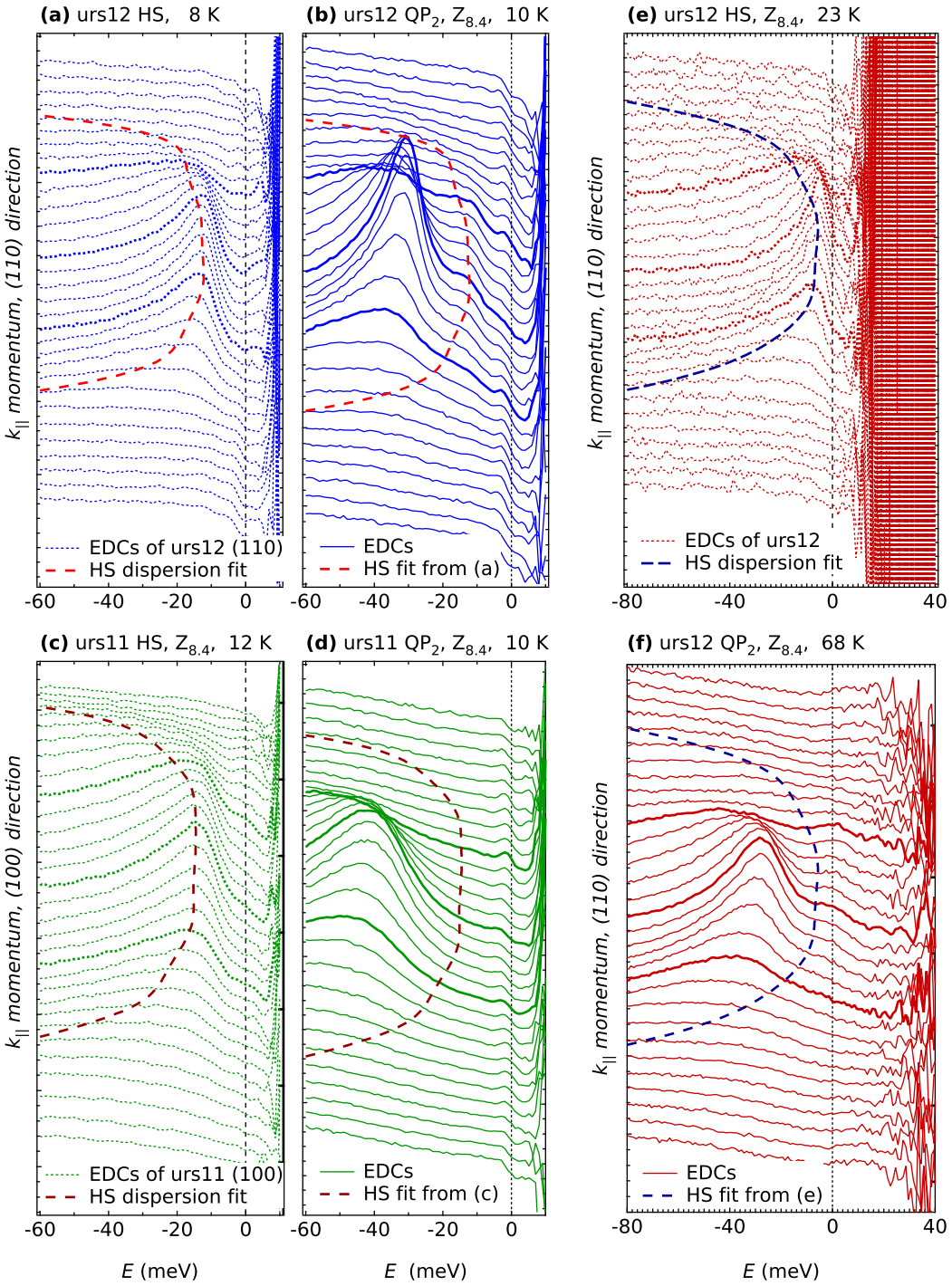

Figure 3.18: **Identity of HS and QP_2.** The panel pairs, grouped by color, show scan on a freshly cleaved (heat-up) surface as solid (dashed) EDCs. The EDCs were obtained by integrating FDD-normalized Xe-I ARPES scans every 0.02 $Å^{-1}$. Bold lines indicate $k_{||}$ values of ± 0.1 $Å^{-1}$ and 0.0 $Å^{-1}$. The overlaid hole-like dispersions represent HS, as discussed in figure 3.8. Panels with blue (red) EDCs are measured along (110) in the HO (PM) state. The green panel shows HO data measured in (100) direction. In all cases, the hole-like HS fit matches the binding energy and shape of the QP_2 dispersion.

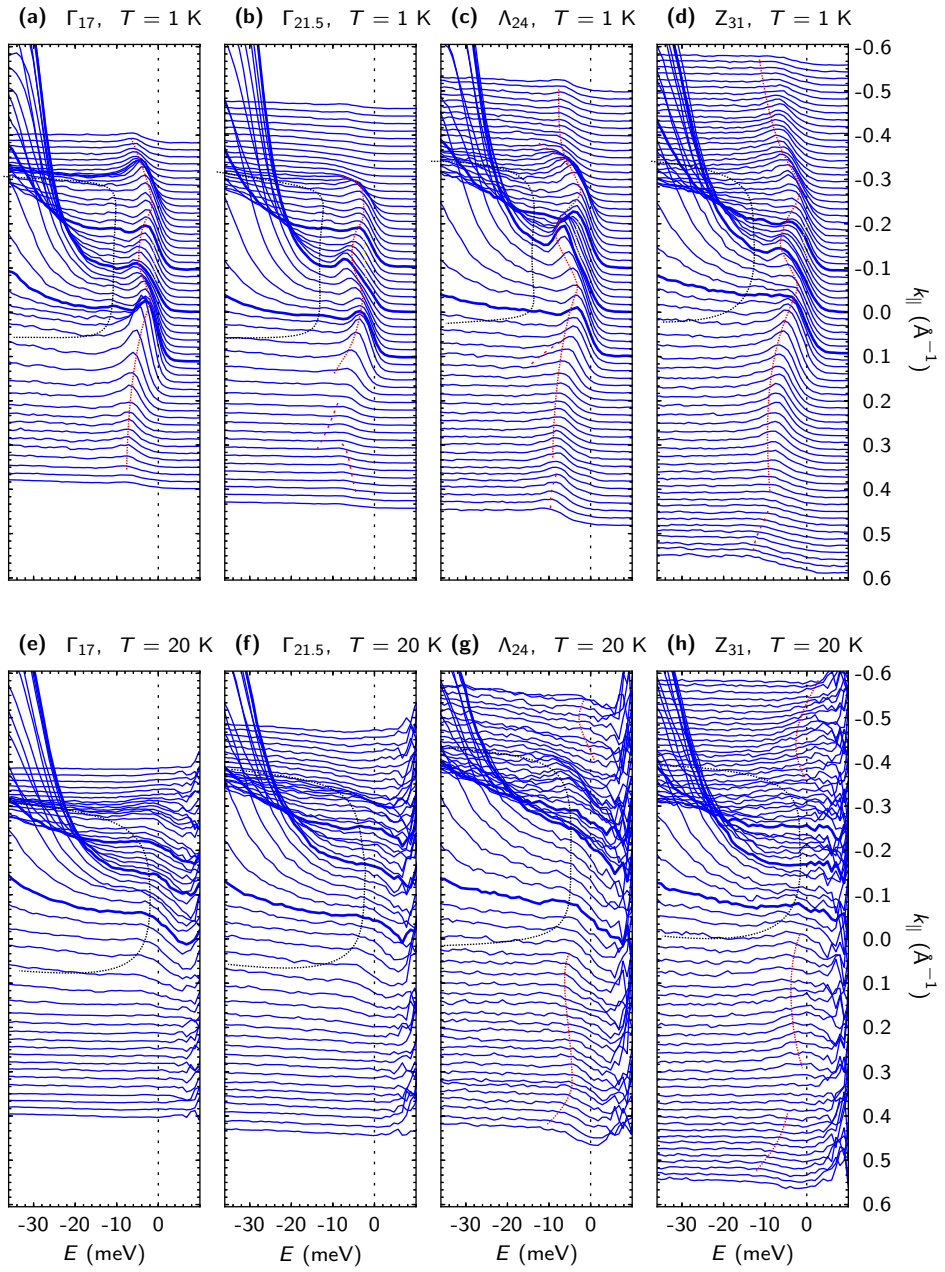

Figure 3.19: **Evolution of QP_1 and QP_2 along $k_\perp$ across the HO transition.** Panels (a-d): waterfall-representation of EDCs in the HO phase at $\Gamma_{17}, \Gamma_{21.5}, \Lambda_{24}$ and Z_{31}, generated from raw data. Panels (e-h): corresponding points in the PM phase, FDD-normalized to illustrate the interaction between of QP_1 and QP2 close to E_F. EDCs for $k_\parallel = 0.0$ Å^{-1} and ± 0.1 Å^{-1} are shown as bold, the others are 0.167 Å^{-1} apart. Dashed lines represent guides to the eye for the dispersions of QP_1 (red), QP_2 (black), and the "split" band (yellow). The shifting and complex evolution of QP_1 and QP_2 across the HO transition are discussed in the main text.

denote $k_\parallel$ values of -0.2 Å^{-1}, 0.0 Å^{-1}, and 0.2 Å^{-1}. In the HO phase, at all points along k_z, there are two heavy peaks, detectable at energies of -3 meV and -11 meV at $k_\parallel = 0$. They are attributed to QP_1 and QP_2.

Electronic structure in the HO phase Depending on where at k_z it is measured, the band QP_1 band looks slightly different. For example at Γ_{17} and Z_{31} [panels (a) and (d)], it reaches its energy maximum at $k_\parallel \approx \pm 0.12$ Å^{-1}, developing its distinct "M"-like shape. At higher momenta, the dispersion is complemented by a flat structure stretching across the remaining $k_\parallel$ area, almost parallel to the Fermi level, less than 10 meV below it. This can be best observed in panel (d), where owing to the high excitation energy, a larger lateral region is visible in the data. There, peaks at higher momenta are well visible, for example in panel (d), as the "wings" of QP_1. They disperse from a binding energy equal to the Fermi level at $k_\parallel = \pm 0.1$ Å^{-1} towards stronger bound states, reaching $E \approx 7$ meV at $k_\parallel$ values ≥ 0.35 Å^{-1}. In spite of the tendency of the wings to disperse towards stronger bound states, behavior usually associated with hole-like bands, they display a positive curvature. This is rather compatible with electron-like bands.

In contrast to its shape at Γ_{17} and Z_{31}, at $\Gamma_{21.5}$ the tips of the "M" are at ± 0.16 Å^{-1} [panel (b)]. There, the band is most intense for momentum values between $k_\parallel \approx \pm 0.25$ Å^{-1}, with its signal significantly diminishing at higher momenta. For momenta $k_\parallel > 0.3$ Å^{-1} the band tends to disperse more rapidly towards stronger binding energies, not anymore parallel to E_F.

At Λ_{24}, the QP_1 dispersion resembles a mix between Z_{31} and $\Gamma_{21.5}$. On one hand, it shows a flat dispersion parallel to E_F at high momenta. On the other hand, it also presents components dispersing rapidly towards more negative energies, as indicated by the red dashed lines in panel (c). This dispersion of QP_1 along k_z is a direct evidence of its bulk nature.

In panels (a-d) a third feature is visible very close to E_F, at energy -1 meV. Indicated by the yellow lines, a peak appears in the falling edge of QP_1 at all points. It, too, was first detected by laser ARPES at the $Z_{7.0}$ point [74], and reported to be a "split" band of QP_1. A novelty in the data here with respect to reference [74] is that both fine structures, QP_2 and the "split" band, exist not only close to Z, but also at the Γ and Λ points. They strech in $k_\perp$ direction across large portions of the reciprocal space.

Electronic structure in the paramagnetic phase In the PM phase [panels (e-h)], none of the fine structure features of the HO regime are discernible. Z_{31} continues to present a heavy dispersion across all $k_\parallel$ values. However, around $k_\parallel = 0$, its electronic structure consisting of QP_1, QP_2, and the "split" band, is now replaced by a broadened structure visible at E_F. At high momenta, the broad band's intensity is much closer to E_F than in the HO phase, appearing in fact to have its main contribution above the Fermi level. Leaning increasingly towards the thermally populated region as the $k_\parallel$ momentum coordinate increases, its electron-like nature now becomes evident. The corresponding structure at Γ_{17} and $\Gamma_{21.5}$ has degraded in intensity for $k_\parallel > 0.25$ Å^{-1} to the point where it is difficult to distinguish from a metallic background. This cannot be attributed solely to the temperature broadening.

Comparing the difference in signal intensities between HO and PM scans exactly at E_F, for example at $k_\parallel$ momenta of 0.3 Å^{-1}, it seems as if the Γ and the Z points evolve

differently across the HO transition. At the Z_{31} point [panels (d) and (g)], the intensity is provided in both phases by the heavy electron band stretching across the whole available $k_{\|}$ region. The Γ_{17} point, on the other hand, displays a hole-like dispersion similar to Z_{31} in the HO phase [panel (a)], but appears more like $\Gamma_{21.5}$ in the PM regime [panels (d) and (e)]. Here, the flat structure is not visible in the data anymore for $k_{\|}$ momenta beyond 0.3 Å^{-1}.

Γ and Z becoming similar in the HO phase Judging by the shape and dispersion of QP_1, in the HO phase the Γ_{17} and Z_{31} points appear to be very similar, while $\Gamma_{21.5}$ and Λ_{24} differ from the former two: $\Gamma_{21.5}$ shows no significant intensity for QP_1 at large k coordinates, and Λ_{24} shows an "S"-like dispersion [red curved line in panel (c)] of QP_1 for 0.2 Å$^{-1} \leq k_{\|} \leq$ 0.4 Å^{-1}. In paramgnetic URu_2Si_2, on the other hand, Γ_{17} and Z_{31} look very differently. Intensity close to E_F at high momenta, which could be attributed to QP_1, is practically non-existent for Γ_{17} in the PM phase. It is gradually appearing at $\Gamma_{21.5}$, finally reaching well detectable levels at Λ_{24} and Z_{31}. One possible explanation, explored in reference [76] and in chapter 4, is that the HO electronic structure is restructured away from a body-centered tetragonal towards a simple-tetragonal crystal symmetry.

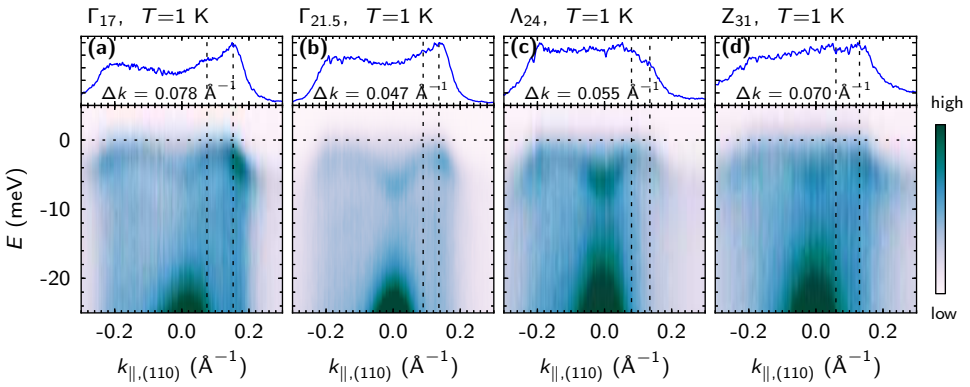

Figure 3.20: **The momentum gap of QP_1.** Raw ARPES intensity at k-space points $\Gamma_{17}, \Gamma_{21.4}, \Lambda_{24}$ and Z_{31} show the dispersion of the QP_1 band. Developing momentum gaps Δk, illustrated by dashed vertical lines, are visible as a perceived three-region dispersion of QP_1 along $k_{\|}$ (left of, between, and right of vertical lines) with reduced ARPES signal intensity between the vertical lines. Curves at the top of each panel represent MDCs integrated in the energy range -4 meV $\leq E_F \leq 1$ meV, distinctly showing two peaks at the Fermi level. Magnitude of the gap Δk is displayed below each MDC.

The momentum gap More exact analysis of the low temperature data from 3.19 reveals that the upper tips of the "M"-shaped QP_1 appear to touch the Fermi level. For example, this can be recognized along the red guide to the eye in panel (d) of the figure. For clarification, in figure 3.20 the raw QP_1 dispersion is reproduced as an ARPES color plot. The intensity is clearly reduced at the Fermi level, indicating that the "M"-shaped band is *not* located entirely below E_F. Instead, it crosses the Fermi level twice, at the positions indicated by the vertical dashed lines, creating a gap in momentum. This is

more clearly illustrated by the MDCs at the top of each panel, which were obtained by integrating the corresponding ARPES data over a region of 5 meV around E_F. The peaks demonstrate that the Fermi surface at the high symmetry points consists, in fact, of two sheets, separated by a momentum gap $\Delta k = 0.03$ Å^{-1} ...0.07 Å^{-1}.

Another method to realize this is by considering that the dispersion of QP_1 around the tips of the "M" is not smoothly curved, as would be expected from a fully occupied band in an ARPES color plot. Instead, it is best described by three edges: one rising from higher momenta towards E_F; another one, of slightly lower intensity, going parallel to E_F for a momentum interval corresponding to the width of the gap; a third one falling again from E_F towards the middle of the "M". It is highly uncommon for a band to show such non-analyticies in its dispersion, the only remaining explanation being that the intensity at the tips of the "M" are cut off by the Fermi-Dirac distribution.

Such a momentum gap opening across the HO transition indicates that two previously anti-crossing bands hybridize. Given the 3D nature of the URu_2Si_2 band structure, a gapping of the Fermi surface can be inferred somewhere else in momentum space even though the exact mechanism remains unknown. The whereabouts of the energy gap is a topic pursued in references [75, 76], as outlined in chapter 4 of this thesis.

Interplay between QP_1 and QP_2 How QP_1 and QP_2 affect one another in the HO phase is shown in figure 3.21. The plots show 2nd derivatives of different ARPES data, from left to right, at $Z_{8.4}, \Gamma_{21.5}$, and Z_{31}. The data in panels (a) and (d) were measured using the Xe-I laboratory light source. For panels (b-c) and (e-f), the data originate from the 1^3 beamline. Red lines indicating the familiar dispersions of QP_1 and QP_2 are guides to the eye.

The influence of temperature on QP_1 can be seen comparing (a) with (b-c), where the "M" structure is visibly shallower at higher temperature. The momentum gap is not visible at 10 K, but this could be a consequence of experimental resolution and thermal broadening. QP_2 shifts towards more negative energies upon cooling. This holds for the Z point aswell as for Γ and is consistent with conclusions from He-I_α experiments from section 2.3, but stands in conflict with laser ARPES data. At the lowest attainable temperature, the highest point of QP_2 is at $E = -15$ meV. Its rapidly dispersing flanks are neatly aligned with SS, as expected. The lowest point of QP_1 is visible around $E = -7$ meV at the lowest temperature, and at $E \approx -3$ meV at $T = 10$ K. This results in an energy gap between QP_1 and QP_2 of $\Delta_{QP} \approx 8$ meV.

Systematic temperature dependency A systematic view on temperature dependency is aided by figure 3.22: EDCs from FDD-normalized Xe-I scans, integrated between $k_\parallel$ values of ± 0.20 Å^{-1}, are shown for a number of temperatures between 10 and 68 K. Solid lines were integrated from ARPES scans on freshly cleaved samples, while dashed spectra are from heat-up surfaces. Intensity of the SS, eventually cut off by the upper border of the image, is not essential in the following.

For temperatures well below T_{HO}, two peaks are visible: one at $E \approx -3$ meV, the other at $E \approx -15$ meV. Small dashes point to their location: thin markers for the one with the lowest binding energy, thick markers for the following one, closest to E_F. Both are shifting towards higher energies, with temperature approaching T_{HO}. At temperatures below T_{HO}, it is clear that the stronger bound peak represents QP_2, the other being QP_1.

Above $T \approx 23$, only one peak remains visible, at a position essentially fixed at E_F for all higher temperatures. Whether the remaining peak above T_{HO} is QP_1 or QP_2 is difficult to ascertain. But for reasons laid out previously, it is assumed to be QP_2. Finally, the T-dependent evolution of the peaks is signalled as a guide to the eye by corresponding thick, respectively thin dashed grey lines.

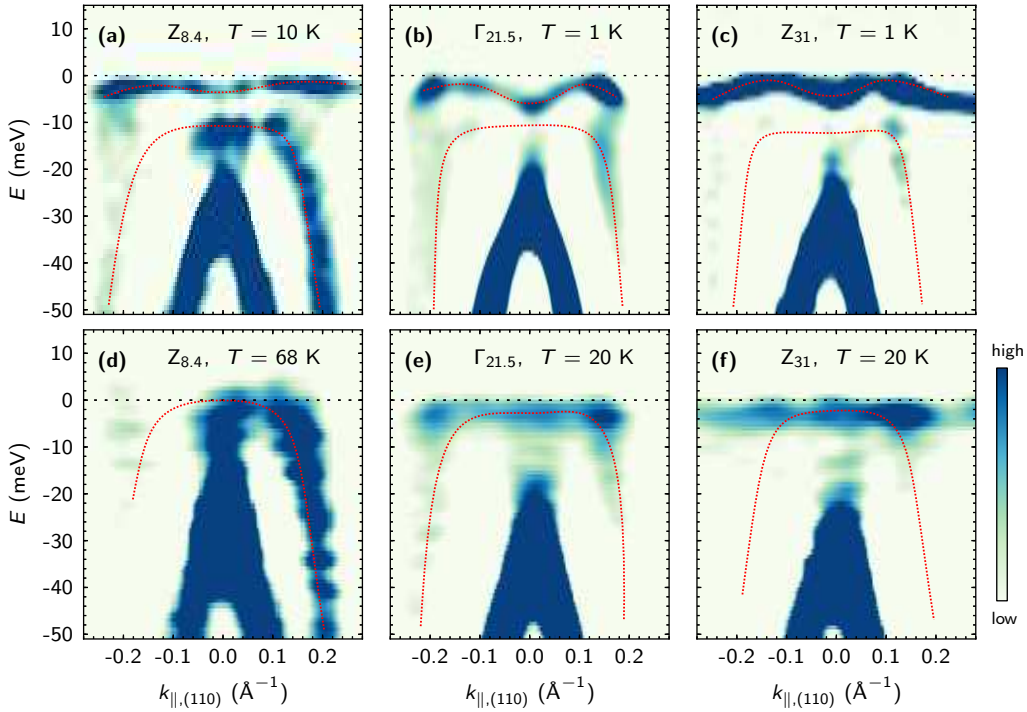

Figure 3.21: **Shifting of QP_1 and QP_2 with temperature.** Second derivatives of ARPES data show the Z and Γ points of URu_2Si_2 in the HO phase (a-c) and PM phase (d-f). The distinct Π-shaped dispersion of QP_2 is observed below the characteristic M-shaped QP_1 at $E_F - 3$ meV in panel (a), and at $E_F - 7$ meV in (b) and (c). Around $E_F - 15$ meV, the heavy part of QP_2 is visible, while rapidly dispersing intensity parallel to SS shows the light part of QP_2. In (d-f), QP_2 has shifted to E_F, pushing away or merging with QP_1. Dashed red lines serve as guides to the full dispersion of the bands. Data was convolved with a Gaussian of widths of 1.5 meV and 0.02 $\mathrm{Å}^{-1}$ for temperatures below T_{HO}, and 1.5 meV and 0.03 $\mathrm{Å}^{-1}$ for temperatures above.

Thus, a good summary of the experimental data at Z is offered by glancing the figure from top to bottom, following the grey lines: in the process of the reorganization of the electronic structure accompanying the HO transition, QP_1 is shifting below E_F, repelling QP_2 to even more negative energies. The latter has a large mass around to $k_{\|} = 0$, being the lower part of a hybridization between a heavy and a light band, which had already formed at temperatures at least as high as 68 K.

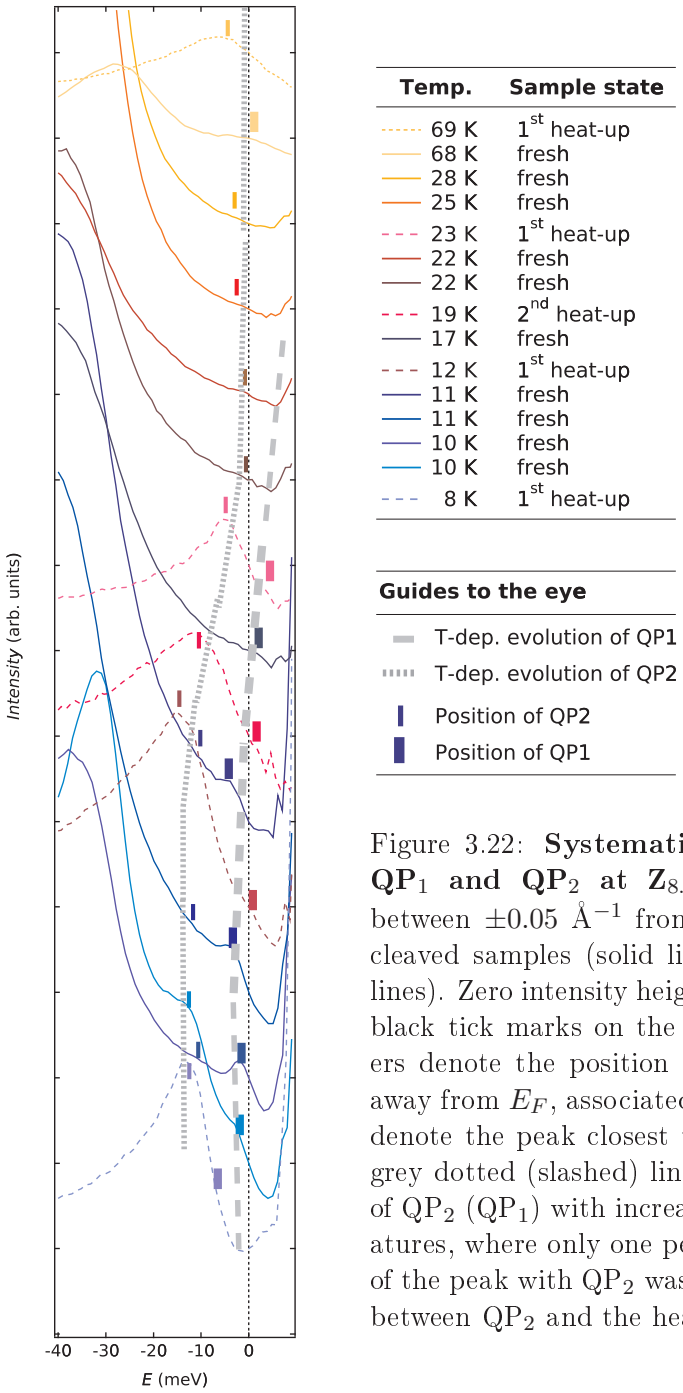

Figure 3.22: **Systematic temperature dependency of QP_1 and QP_2 at $Z_{8.4}$.** EDCs were integrated for $k_{\|}$ between ± 0.05 Å^{-1} from various APRES scans on freshly cleaved samples (solid lines) and heat-up samples (dashed lines). Zero intensity height for each EDC is demarked by the black tick marks on the vertical axes. Thin vertical markers denote the position of the quasi-particle peak farthers away from E_F, associated with QP_2. Thick vertical markers denote the peak closest to E_F, associated with QP_1. Bold grey dotted (slashed) lines serve as guides for the evolution of QP_2 (QP_1) with increasing temperature. At high temperatures, where only one peak is visible at E_F, the association of the peak with QP_2 was based on the matching dispersions between QP_2 and the heat-up state shown in figure 3.18.

3.4.2 The Γ-Point, Revisited

QP_2 at the Γ-point The complex T-dependent behavior and interdependence of QP_1 and QP_2 close to the Z point appears to be a signature for the HO transition. This persuades into revisiting the old He-I_α data analysis at the $\Gamma_{21.2}$ point from section 2.3, where QP_2 had not been accounted for. Owing to the short life time of the URu_2Si_2 surface under the influence of the He lamp, several dozens of scans at varying temperatures and quality levels had to be performed in 2007–2008. On one hand, a side effect of this necessity was that it supplied many data points along the HO ↔ PM transition temperature. This should allow for a systematic analysis of the T-dependent QP_1 and QP_2 shifting. On the other hand, the reduced signal-to-noise ratio for He-I_α data dampens expectations. But as it is already established that QP_2 exists at $\Gamma_{21.5}$ in the ordered phase, it is assumed that this is also the case at $\Gamma_{21.2}$. Then the quest of proving its existence doesn't need to be pursued. Instead, the lighter task is attempted of only assessing where QP_2 is, in order to check for a systematic behavior within the error bars.

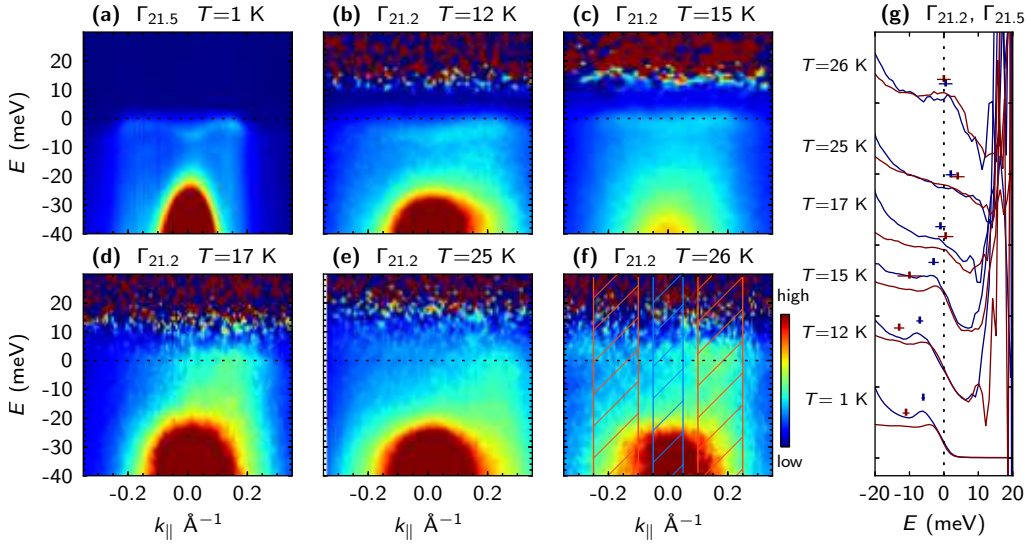

Figure 3.23: **Systematic temperature dependency of QP2 at $\Gamma_{21.2}$.** Panel (a): ARPES intensity plot as raw data, measured at 1^3 in the (110) direction with an excitation energy of $h\nu = 21.5$ eV (comparable to He-I_α). Panels (b-f): FDD-normalized ARPES intensity plots measured at various temperatures between 12 Kand 26 K using a He-I_α excitation energy of $h\nu = 21.2$ eV. The QP_2 dispersion, sharply visible in panel (a) below the characteristic M-like QP_1, is also discernible as a faint increase in intensity in the other HO scans [(b) and (c)] at energies smaller than −10 meV. In the PM phase, a broad, apparently non-dispersive feature, is detectable at or above E_F. Panel (g) shows integrated EDCs in around $k_\parallel = 0$ [blue lines, in panel (g), blue hashed area in (f)] and $k_\parallel = \pm 0.2$ (red lines, orange hashed area). Small crosses denote the positions of QP_1 (blue) and QP_2 (red), assigned as specified in the main text. The width of the crosses represents the error in the peak position.

Figure 3.23 shows a summary of the findings. Panels (b-f) show FDD-normalized He-I_α ARPES intensity at $\Gamma_{21.2}$ for various temperatures. For comparison, and as a

supplementary data point, panel (a) shows data at $\Gamma_{21.5}$ measured with synchrotron light at 1 K. It demonstrates that the difference between QP_1 and QP_2 is largest around $k_\parallel \approx \pm 0.2$ Å^{-1}, suggesting this as the region in which QP_2 would be easiest to discern from QP_1. QP_2 is still essentially flat in this region, as shown for example in figure 3.19. Thus, the error induced by reading its binding energy here instead of at $k_\parallel = 0$ will be insignificant. QP_1, on the contrary, is rapidly dispersing between -0.2 Å^{-1} and 0.2 Å^{-1}, and has its lowest binding energy at $k_\parallel = 0$. It is therefore most promising to look for the binding energy of QP_2 in EDCs around ± 0.2 Å^{-1}, and for QP_1 in EDCs at zero angle, as indicated representatively by the by the red, respectively blue hashed areas in panel (f). The corresponding EDCs were integrated and displayed in panel (g) in order of increasing temperature as red and blue lines. The peak positions corresponding to QP_1 and QP_2 are shown by small crosses. They have the same color as the EDCs from which they were obtained. Errors in the locations of the peaks are represented by the width of the crosses. As a fail-safe measure, the position of each peak was verified by hand for consistency with the angle-resolved data—a procedure not illustrated here. This was performed by slightly varying the integration area and observing which of the features below E_F change, indicating noise, and which are resilient to the changes, suggesting a legitimate signal of QP_2.

QP_1 is clearly visible at all temperatures. QP_2, as predicted, is also detected in spite of the large statistical noise. This is valid in particular for temperatures well below T_{HO}. For example, in the red EDCs, at 12.3 K, the two peaks are at -13 meV, respectively -5 meV. At higher temperatures, only one peak appears, residing at or above E_F regardless of the integration area. There, "red" and "blue" lose their associations with QP_1 and QP_2. The data doesn't show whether one of the peaks vanished, or whether they both exist at or above E_F, but cannot be resolved because of line broadening. However, consistently with previous considerations, the single peak at higher temperature is hereby proposed to be QP_2.

Reinterpretation of the He-I$_\alpha$ data The existence and temperature dependence of QP_2 in the He-I$_\alpha$ data at $\Gamma_{21.2}$ calls for a re-evaluation of the conclusions from section 2.3. The main assertion stands: a heavy quasi-particle band, here QP_1, crosses the Fermi level as temperature drops below the HO transition point. But details of the scenario are changed.

From the considerations above, it follows that QP_2 is identical to the CB band. However, since QP_2 is the lower part of a hybridization between a heavy f-electron and a light hole-like band, CB is not necessarily guaranteed to go through E_F anymore—at least not in straight-forward manner, as implied in section 2.3.3. The proposed Fermi surface then must arise not from CB, but from the tips of the "M" crossing E_F twice. Instead of the single-sheet from figure 2.8, a double-pocket Fermi surface is expected, dispersing along k_z for large parts of the reciprocal space.

A simple two-band hybridization picture between QP_1 and CB is thus not sustainable anymore. But a hybridization of QP_1 with other bands is not necessarily ruled out, it just requires more than only the presence of a heavy f and a light hole-like band. A fitting scenario is to be elaborated in section 3.4.4.

3.4.3 ARPES Signature of the HO Phase Transition

In light of the QP_1 and QP_2 behavior at Γ and Z, a more consistent picture of the HO-induced band structure changes emerges. Figure 3.24 displays the binding energies of these bands at the two high-symmetry points against the relative temperature. In both panels, the blue (red) data points represent QP_1 (QP_2), as discussed in sections 3.4.1 and 3.4.2. The grey points are those formerly published [49, 57], where no distinction between QP_1 and QP_2 was yet made.

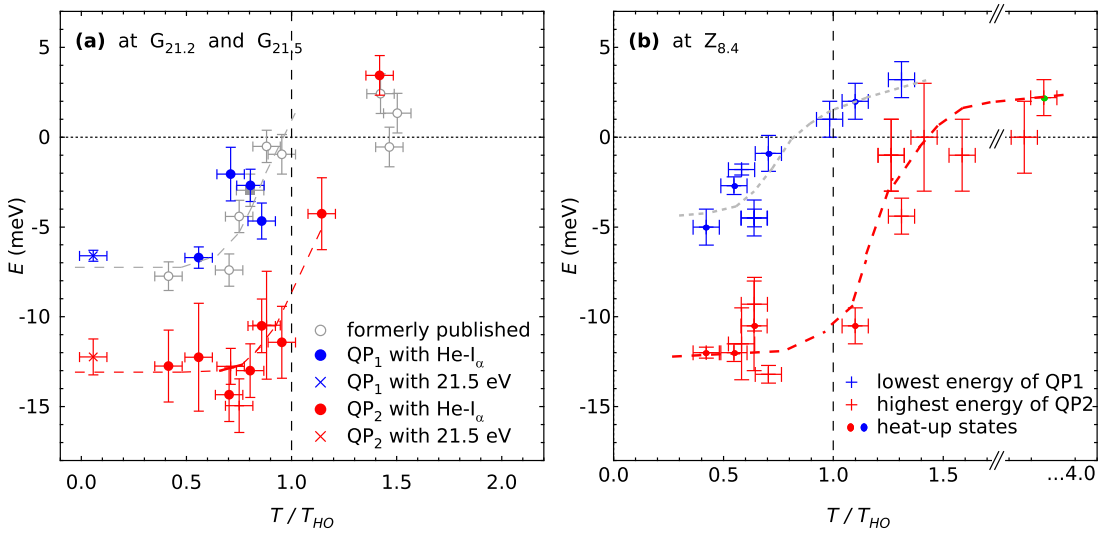

Figure 3.24: **Binding energies of QP_1 and QP_2 as a signature of the HO transition.** Lowest energy point of QP_1 (blue) and highest energy point of QP_2 (red), both at $k_{\parallel} = 0$, are shown in dependency of measurement temperature. Negative region is below E_F, positive region is the thermally populated area. The graph shows points formerly published in [57] (grey color, empty circles), new points measured wit He-I_α excitation energy (full circles) and new points measured at 1^3 with excitation energy 21.5 eV (crosses). Measurement temperature is the fitted temperature of the reference sample for He-I_α data, and thermocouple temperature for 1^3 data. In the PM phase, the points represent the only detectable peak, without a discernible dispersion. Large error bars in the position of QP_2 peaks stem from a small signal-to-noise ratio in the He-I_α scans. Dashed lines guide the eye through the proposed shifting of QP_1 and QP_2 during the HO transition.

At $\Gamma_{21.2}$, in panel (a), QP_1 is starting in the cold region at energies around $E \approx -7$ meV, gradually shifting with heating, reaching the Fermi level at $T \approx T_{\mathrm{HO}}$. QP_2 is traversing the HO phase mostly at $E \approx -13$ meV, abruptly shifting towards E_F at a relative temperature $T/T_{\mathrm{HO}} \approx 0.75$ and reaching $E \approx -8$meV (still below E_F) at the transition temperature. In paramagnetic URu_2Si_2 on the other hand, only QP_2 is visible. The plot in panel (b) certifies a similar behavior at $Z_{8.4}$. QP_1 starts from $E \approx -5$ meV at low temperature and crosses E_F at T_{HO}. QP_2 moves from $E \approx -13$ meV to reach -10 meV at T_{HO}. Consistent with investigations of the heat-up state in section 3.2, QP_2 finally stops shifting at $T \approx 25$ K, marking the end the band structure reorganization process.

Slight differences between the Γ and Z points are suggested only through the data points of the heat-up state, displayed as filled circles in panel (b): at Z there is a small temperature range between $T/T_{\mathrm{HO}} = 1.0 \ldots 1.3$, corresponding to $18 \ldots 22$ K, where QP_1 and QP_2 are detected simultaneously. This could indicate that QP_1 may not disappear immediately at 17.5 K. But since corresponding data points are lacking for Γ, and are subject to large error bars at Z on freshly cleaved samples, it is not possible to attach further physical meaning to this circumstance here.

The data suggests that it is the dropping of QP_1, "pushing" QP_2 below E_F in the process, that is creating the effects associated with the HO phase transition. The gradual shifting of the binding energy of QP_1 thus supplies a direct quantitative measure for the order parameter of the HO phase.

3.4.4 The 3-Band Model

Summing up the experimental facts, the fine structure discovered at the Z point, consisting of QP_1, QP_2, and a split band close to E_F is also detectable at Γ. A crucial insight is that QP_2 is not a satellite of QP_1, but likely a hybridization between a heavy band and a light hole-like band. It is detectable up to temperatures as high as 68 K, close to the lattice coherence temperature of in $\mathrm{URu_2Si_2}$. Consequently, it is not the product of an electronic restructuring triggered by the HO transition.

Hybridization of three bands A possible phenomenological model to explain the facts involves a hybridization process between three bands at E_F: one light hole-like conduction band (band 1 in table 3.1), a very heavy band (2), and one light electron band (3). In figure 3.25, panels (a) and (b), the proposed bands are displayed as dotted lines in colors green, blue and red, respectively. The relative effective mass m/m_e, binding energies in the HO and PM states, and the hybridization potential $V_{o,xy}$ (for the hybridization between bands x and y) are presented in table 3.1.

In the PM state, shown in panel (a), the flat heavy band is 2 meV above E_F and its hybridization with band 1 results in the structure observed as QP_2 below E_F. The e-like band 3, higher in energy, possibly above the top of band 1, does not affect what happens near the Fermi level. At $T = T_{\mathrm{HO}}$, in panel (b), the bottom of the e-like band 3 drops close to or touches E_F, possibly after having already gone down from its position at higher temperatures. The repulsion with the flat band 2 starts pushing the latter below the Fermi level. Hybridization between all the bands starts creating a complex structure. Well below T_{HO}, band 3 has reached its minimal binding energy (approximately E_F).

To describe the resulting electronic structure, starting from negative energies towards positive states, the hybridization between the three bands creates first QP_2, then QP_1, the long-wings heavy-electron band with a characteristic "M" shape. A third "W"-shaped band above E_F would be the smoking-gun evidence necessary for a complete understanding, but it is impossible to observe directly using ARPES. Panels (c,d) in figure 3.25 show the data set from 3.19(d,h) (i.e. at Z_{31}) as ARPES intensity plots, with the hybridized bands from figure 3.25(a,b) overlaid as dashed lines.

Variations of the model Not all experimental features of the QP_1 and QP_2 dispersion could be optimized simultaneously in the fitting process. The strategy was therefore to

Table 3.1: **Summary of the 3-band hybridization parameters.** In the HO phase, the light e-like band was artificially moved to 60 meV above E_F, far enough to avoid any significant influence on the hybridization between the light hole-like and heavy f-electron band.

Band	**Character**	m/m_e	E_{HO} (meV)	E_{PM} (meV)	$V_{o,xy}$ (meV)
1	light hole	-1.6	35	35	$V_{o,12} = 11$, $V_{o,13} = 11$
2	heavy electron	500	8	2	$V_{o,21} = 11$, $V_{o,23} = 7$
3	light electron	1.6	8	60	$V_{o,31} = 11$, $V_{o,32} = 7$

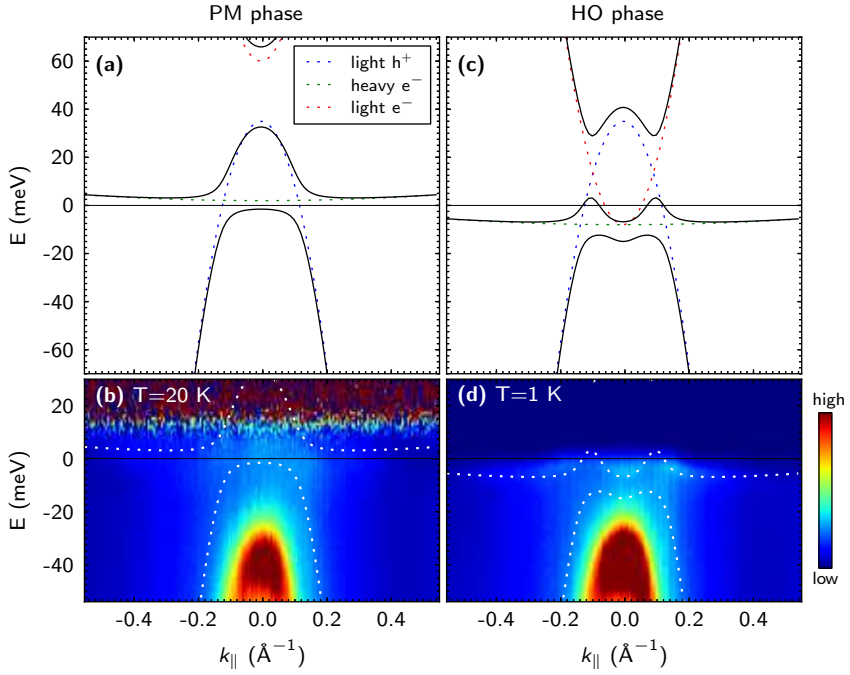

Figure 3.25: **Interaction between QP_1 and QP_2 modeled as a 3-band hybridization process.** Panels (a-b): hybridization between the heavy ($m/m_e \geq 500$) fermion band forming the high-k "wings" of QP_1 bound at $E_{\text{heavy}} = 2$ meV and the light hole-like band CB at $E_{\text{CB}} = 35$ meV above E_F (see also chapter 3.1). Panel (a) shows the original bands as colored dashed lines, the hybridized bands as solid lines. Panel (b) shows the hybridized bands as dashed lines superposed on an FDD-normalized ARPES intensity plot at Z_{31} in the PM-phase. Panels (c-d): same for the HO-phase; the ARPES plot in panel (d) represents raw data. Additionally, in the HO phase a previously non-interacting light electron band appears and hybridizes with the doublet from (a-b). Hybridization interaction potentials were not changed across the transition.

model the overall dispersion of the bands at lower $k_\parallel$ values ($|k_\parallel| \lessapprox 0.2$ Å^{-1}) as well as possible, without emphasizing a particular feature more than another.

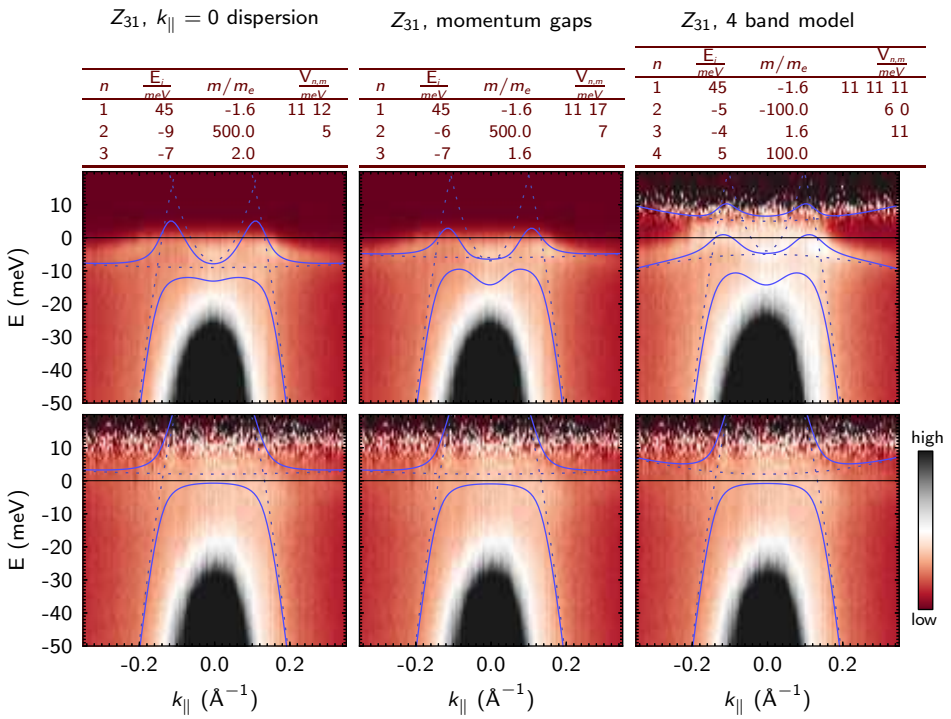

Figure 3.26: **Variations and limitations of the 3-band model.** Panels (a-c): ARPES intensity plots showing the same data set [FDD-normalized in panel (c)] of the HO phase at Z_{31}, overlaid with differently optimized versions of the 3-band model [panels (a-b)], and a 4-band model version [panel (c)]. The different optimization strategies are described in the main text. At the top of each panel a table with the original binding energies E_i of the non-hybridized bands, their effective masses m/m_e, and their interaction potentials $V_{n,m}$ (for each band n) is displayed. Bands are numbered as follows: light hole-like band ($n = 1$), heavy band below E_F ($n = 2$), light electron band ($n = 3$), heavy band above E_F ($n = 4$). Panels (d-f): PM-versions of the panels (a-c), where the light electron band $n = 3$ has disappeared and the heavy f-band has shifted to +2 meV. In panel (f), and the heavy hole-band $n = 4$ is also considered gone. Everything else remains unchanged between corresponding pairs of panels.

To convey an idea of the reliability of the 3-band model, other optimization strategies for fitting are discussed with the aid of figure 3.26. In panel (a), effort was concentrated to model the dispersion around $k = 0$, trying to capture the QP_1/QP_2 interaction at small $k_\parallel$. In (b), parameters were optimized to the dispersion around k-values of the gap, thus laying particular interest on the tips of the "M" forming the Fermi surface. To achieve this, the simulated dispersion of QP_2 was permitted to deviate from the experimental data as far as necessary. Finally, panel (c) shows a model that tries to achieve better results using 4 hybridizing bands instead of 3. The sign of the heavy band is inverted to match the dispersion of the heavy wings at larger k-values, far off $k_\parallel = 0$. The fit to the "wings" of QP_1 improves in the displayed region. However, at momenta

$|k_{\|}| > 0.3$ Å^{-1}, outside the scale of the plot, the resulting hole-like dispersion of the fitted band increasingly fails to describe the experimental electron-like band.

Robust facts inferred from the model The main insight delivered by the 3-band model is that for the particular dispersion of QP_1 close to $k_{\|} = 0$, the hybridization of two bands is not enough. To understand the "M"-like structure, a light, hole-like electron band crossing E_F is crucial. The character of the heavy band at E_F, here modeled as electron-like, is not relevant: given any effective mass $|m/m_e| \geq 20$, other parameters can compensate in order to reproduce the "M". The model also robustly explains why QP_1 and QP_2 are shifting in tandem: both are being repelled by the heavy band 2. Finally, the model illustrates how a constant hybridization potential of ≈ 10 meV, compatible with data at the X point and information from other experiments, is enough to consistently explain changes in the electronic structure across the HO transition.

Limitations of the model However, the 3-band model also suffers from a number of limitations. Everything above E_F in the PM state, in particular the energy of the heavy band, cannot be verified experimentally. Thus, QP_1, an essential ingredient of the HO phase, is missed the PM state, leaving its whereabouts open to speculation. Many parameters of the model, for instance the exact band masses, are flexible. Deviations in one parameter can be accomodated to a certain degree by tuning others. This is valid in particular for the hybridization strength: it was a deliberate choice to perform the simulation with a fixed potential, to demonstrate that it was suitable to describe the data. In any case, the model fails to reproduce the positive curvature of the QP_1 wings at high momenta, regardless of its assumed character. This suggests that a tight-binding model may be more appropriate for the heavy band.

Two central questions cannot be answered by the model: where does the light electron band stem from, and why does it and the heavy band drop, effectively pushing the hybridized QP_2 below E_F in the process? The light band must be already present below E_F in the PM state to assure conservation of particles. So far, it is not detectable at the Γ or Z points, but may be somewhere at different momenta in reciprocal space. Ultimately, where this band comes from and why it drops remain open questions. One possibility is nesting. However, standard nesting or band-folding act differently: in the case of folding, one band is wrapped "rigidly" onto another at a given instant. The intensity of the spectral function is being redistributed symmetrically around the symmetry point(s), but binding energies of the bands do not change gradually with temperature. Instead, only the hybridization gap between the original and folded bands may grow larger with cooling.

3.5 Implications

3.5.1 The Main Facts

To recapitulate, hybridizations between coherent, light hole-like and heavy f-electron bands were measured at the X point. The hybridization strength of approximately 10 meV does not change across the HO transition temperature. At normal emission along k_z, the feature QP_2 gives evidence of a similar hybridization, with the same strength, between a heavy and a light band, having been detected already at temperatures around 70 K. The dispersion of the band, and thus the nature of the hybridization, does not change across the HO transition. Only its binding energy starts shifting, together with QP_1, in correlation with the newly emerging order. Both bands, apparently of different origin, shift in tandem below E_F at temperatures below T_{HO}, offering a direct measure for the HO order parameter. A simple 3-band model consistently describes the changes to the electronic structure induced by the HO transition at multiple high-symmetry points.

3.5.2 Complementing and Diverging Views

Independent investigations of other groups conducted in parallel to the research at the base of this thesis offer essential clues to the interpretation of the data. As repeatedly discussed in previous sections, laser ARPES efforts [64, 74] attest the existence of the "M"-shaped band, the second QP peak, and another "split" band at E_F at the $Z_{7.9}$ point. Scanning tunneling spectroscopy (STS) experiments [59, 63] reported a heavy band splitting and hybridizing with a light hole-like band at or above E_F in the HO phase—a scenario very similar to the one proposed here.

But there are also differences between the 3rd-party experimental results and those presented here. For instance, the quasi-particle dispersions at $Z_{7.9}$ are reported to vanish upon entering the PM phase [64]. The authors do not specify whether the QP in question is QP_1 or QP_2 (the distinction between the two having not yet been published at that time), but the characteristic "M"-shaped dispersion suggests that they observed QP_1. However, spectral intensity at the Fermi level is visible at $Z_{8.4}$ up to 70 K in the form of QP_2. This band is shifting towards higher energy states with increasing temperature, displacing QP_1 in the process. The latter may not be discerned anymore in raw data of freshly cleaved samples, but a heavy dispersion characteristic to its high-k wings is.

In STS data, the details of the reported heavy-fermion double-structure differ from the way QP_1 and QP_2 were shown to interact. While my data show robustly that the bands are both situated below E_F in the HO state, Schmidt *et al.* exhibit the gap between the heavy bands to be essentially above the Fermi level. On one hand, this could be related to the connection between the "split" band and QP_1, hinting at its possible origin as a crystal-field induced effect. On the other hand, the STS data may show another version of the QP_1 and QP_2 interaction. To a degree, differences in the binding energy could be reconciled by the fact that the experiments are probing different positions in momentum space.

There are also very recent time-resolved laser ARPES experiments, which complement the picture offered here. Dakovski *et al.* reveal itinerant QPs with a "dramatically" increased life time in the ordered state at Z_7 [66]. This was confirmed by Chatterjee *et al.* in ARPES experiments [79] at Γ_{50} at the 1^3 BESSY beamline. The authors of the

latter publication claim that the decrease in width of the QPs visible in their data cannot be explained by thermal broadening alone. It is instead associated with a strong increase in QP life time and offered as a consequence of the lattice coherence forming or strongly increasing at the HO transition temperature, consistently with momentum-integrated optical and transport data (section 1.2.5).

In summary, although the majority of hard facts presented in this thesis are confirmed by similar experiments, noticeable differences persist in particular in the way results are interpreted. Issues raised revolve around three interconnected topic areas: (**i**) the formation of the Kondo lattice, (**ii**) the reconstruction of the Fermi surface during the phase transition, and (**iii**) the life time of the involved QPs, indicating coherence. In the following, these interpretation differences will be discussed by reference to the two essential data features from this thesis, QP_1 and QP_2.

3.5.3 The Interplay Between QP_1 and QP_2

It is important to realize that QP_1 and QP_2 are of fundamentally different nature and interact in an intricate way. In the following it will be elaborated why this is the case and how this aids the interpretation of the HO as a Fermi surface instability of a coherent lattice.

QP_2 and the Kondo lattice Considering the Kondo lattice, two questions are aching: when does it reach its fully developed stadium, and how is it related to the HO? The initial formation of the Kondo lattice with an associated hybridization gap of ≈ 10 meV is not a novelty in URu_2Si_2 history, having already been inferred from IR and transport data [13, 14, 15, 17, 24, 68] (section 1.2). Many HO related effects were attributed to an emerging, not yet fully formed Kondo lattice [72, 73], with the HO transition itself being elevated as the point at which a coherent lattice fully evolves.

Here QP_2 delivers an essential clue. The band has all the characteristics of a hybrid between a light hole-like and a heavy electron band already at higher temperatures. It is moving to lower binding energy at temperatures below 30 K, but remains otherwise unchanged. Further in the PM state, it continues to remain unchanged until 70 K, with the exception of temperature broadening. Consequently, it can be interpreted as the manifestation of a fully developed Kondo lattice forming already far into the PM state and remaining largely unaffected by the HO transition. The experimental data at the X point, where the upper and lower components of the hybridized bands are clearly observed even at 35 K, also prove this unambiguously.

The multi-component structure of QP_1 QP_1 disappears above E_F in the PM phase, with the "M"-dispersion being undetectable at 20 K. To investigate the nature of QP_1, polarization-dependent data is displayed in figure 3.27. Panels (a–f) are reproduced from reference [79], and are accompanied by my own scans in panels (g–l). Both data sets were measured at the 1^3 BESSY beamline by different groups of researchers, independently of one another.

In (g) and (h), ARPES intensity plots in the HO phase are shown, measured using linear vertical (LV) and linear horizontal (LH) beam polarization. Panels (j) and (k) show similar data for the PM case. The increased intensity of the rapidly dispersing QP_2 flanks for LV excitation is already evident from the raw data in panels (h) and

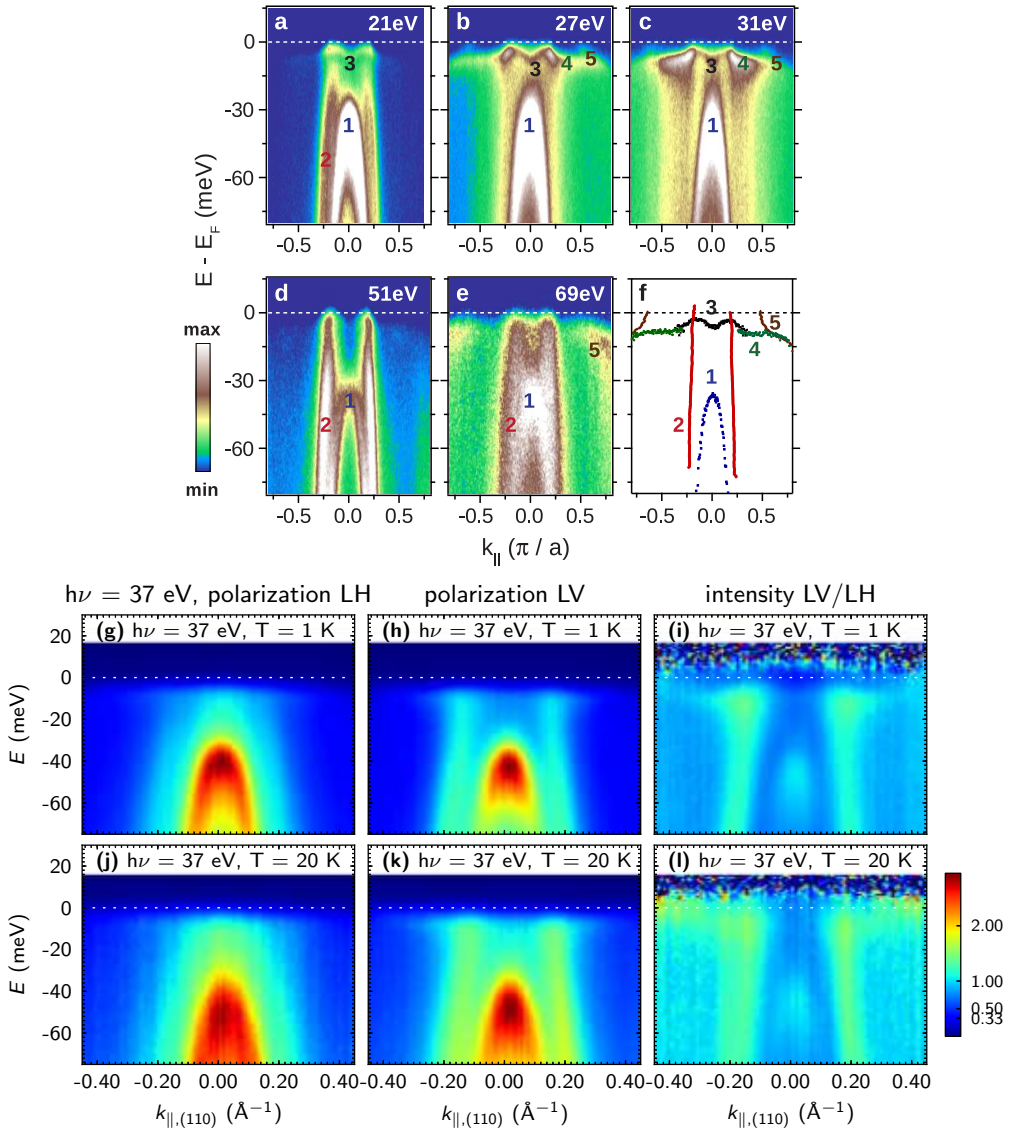

Figure 3.27: **Polarization dependence of the HO features in URu_2Si_2.** Panels (a-f), extracted from reference [79], show high-resolution ARPES data in the HO phase of URu_2Si_2 along $k_\perp$ using different beam polarization settings. Panel (f) shows a sketch of components of QP_1 and QP_2 with differing orbital characters. Panels (g,h): ARPES intensity plots at 1 K measured at 37 eV in linear vertical (LV) and horizontal (LH) polarization, respectively. Panels (j,k): same data in the PM phase. Panels (i) and (l) show intensities from plots (g,h) and (j,k), respectively, normalized to the maximum intensity point of the SS and divided by one another. The different orbital character for single components of the QP_1 and QP_2 bands is visible as intensity values different from 1.0.

(k). To highlight a possible change across the transition, intensities were normalized to the maximum intensity point, i.e. the peak of SS, then divided by one another. This carries the implicit assumption that SS is insensitive to beam polarization—a condition which was not formally verified, but experiments and literature so far have not given any reason to assume otherwise. In any case, even if SS was dependent on beam polarization, it is not expected to change across the HO transition. Thus, for the stated purpose of detecting changes in the quasi-particle bands close to E_F, the employed method is assumed accurate.

Panels (i) and (l) show the intensity ratio LV/LH for the HO, respectively the PM case. Color coding was chosen with light-blue corresponding with a ratio of 1.0, which can be easily verified by the flat intensity where SS is expected. Deviating to a ratio of LV/LH ≈ 1.8, the low-mass QP_2 flanks are subject to the most drastic change of intensity when switching polarization. This holds for both the HO and the PM phase. For QP_1, a difference between the LV/LH ratios at different temperatures appears to occur only at the high-momenta "wings". This is noteworthy because other features, for example the "M"-shaped part of QP_1 close to $k_\parallel = 0$, and the heavily dispersing part of QP_2, remain completely unchanged upon polarization switching. This is seen in the flat-blue intensity at E_F in panel (i), and between $k_\parallel = \pm 0.1$ Å^{-1} in panel (l).

In conclusion, the e-like part at momenta around $k_\parallel = 0$, the "wings" at $|k_\parallel| \geq 15$ Å^{-1}, and the rapidly dispersing QP_2 flanks behave in at least 3 different ways upon polarity change. Panels (a-f), in which the features numbered 3–5 correspond to QP_1, were reproduced from reference [79] to document that Chatterjee *et al.*, too, arrive at the same conclusion: the "M"-shaped structure is made of components with *"substantially different orbital character"*. Given their distinct nature, not only may QP_1 and QP_2 behave differently with changing temperature, but also for itself is QP_1 not necessarily guaranteed to evolve uniformly for all momenta across the HO transition.

Instability of the coherent lattice Direct proof for Fermi surface instability, indirectly suggested by massive gapping of the Fermi surface at the HO transition temperature, was delivered by ARPES as the heavy QP_1 shifting across E_F (section 2.3). If and how a hybridization with the light hole-like band took place was then still speculated. Meanwhile, it is revealed that the reconstruction is accompanied on one hand by gaps in the range 2–5 meV, appearing upon cooling below the transition temperature and associated in part with the momentum exchange vectors Q_0 and Q_1 [10, 11, 18, 19, 48, 53, 72]. On the other hand, prognostic effects of the instability seem to appear at temperatures close to, but definitely above T_{HO}: changes in band structure that occur already in the PM phase below 30 K are accompanied by a hybridization gap in the range 10–12 meV [68].

The behavior of the QP_2 structure fits in here remarkably well: the band performs a significant amount of its shifting upon cooling already below 25 K, but remains stable at higher temperatures up to at least 68 K. On one hand this is an indication that, while the coherent lattice is an essential ingredient of the HO transition, it does not suffice as the only mechanism involved. On the other hand, STM also shows [59] that the FS reconstruction appears in spatial correlation to the Kondo lattice (U-atoms!), a clue that the two are related. The HO therefore evolves on the already developed Kondo lattice. How exactly, that still remains unclear. But more than the simple onset of coherence is

at play, and the multi-component structure of QP_1, another main ingredient of the HO transition, seems key to understanding.

3.5.4 Quasi-Particle Life Time as a Consequence of Gapping

The transition acts differently on various high symmetry points. While the X point remains indifferent, a momentum gap is detected along k_z, observed in the data in the vicinity of the Γ, Z and Λ points (section 3.4.1). Even if the exact microscopic mechanism behind this is not obvious, the momentum gap implies an energy gap somewhere else in momentum space between hybridized bands. According to the 3-band model, the gap is related to the reorganization of itinerant band structure elements (shifting of a heavy and a light band) and is of the order of 10 meV. By its magnitude and its likely origin, it matches the PM hybridization gap from transport data excellently. With the momentum gap in QP_1 in one hand, and the 3-band hybridization model in the other, two independent pieces of evidence are available for at least one energy gap opening in the Fermi surface of URu_2Si_2.

With less states to scatter to accessible at the Fermi level, coherence of the quasi-particles is expected to increase—a conclusion also drawn from thermal transport data [40]. According to references [66, 79], the specific part of QP_1 representing the "wings" [bands 4 and 5 in figure 3.27(f)], is changing life time. But this does not necessarily require the quasi-particles to be formed only at the HO transition temperature. Instead, a fully coherent lattice may well exist at higher temperatures. The sudden increase of the QP sharpening observed across T_{HO} would then emerge as a natural consequence of the Fermi surface gapping.

Last but not least, it should be noted that the change in quasi-particle life time is documented only for a specific part of QP_1, namely the "wings" at high momenta. What happens to the other components of this complex band is not established.

3.5.5 Conclusion

The results demonstrate that the HO transition is intimately related to the Kondo lattice elements of URu_2Si_2. This occurs via a hybridization of 10 meV observed consistently at several high-symmetry points, as suggested also by simple, yet robust theoretical considerations. The data integrates very well with previous He-I_α results of the Paris / Würzburg group and with comparable experiments of others. Offering a consistent scenario to describe band structure changes across the transition, it is helping to reconcile a number of differences between modern momentum-resolved experiments. The band hybridization, taking place between a heavy-fermion band *and* a light electron band, requests that itinerant quasi-particles with a high effective mass be a part of a successful theory to describe the HO phase transition.

Chapter 4

Gaps and Symmetries of the "Hidden-Order"

The URu_2Si_2 investigations of the Paris / Würzburg group continued throughout the time period of the writing of this thesis, succeeding to identify the location of the HO Fermi surface gaps and the symmetries associated with the transition. I helped to perform large parts of those experiments, aided with certain aspects of the data analysis, and participated in the scientific discussions. Nonetheless, the main merit for this research is attributed to Cedric Bareille and his PhD advisor, Prof. Dr Andres Santander. In the following, an outline of their work is presented, based on figures from reference [76], which we published together.

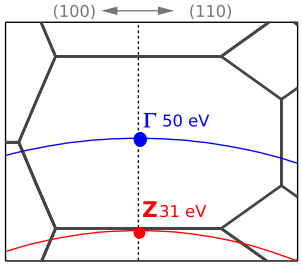

The high-symmetry points discussed in this chapter, Γ_{50} and Z_{31} (image to the right), were measured at the 1^3 BESSY beamline. The facts to be presented emerge seamlessly from the topics of previous chapters. They extend the messages conveyed therein and arrive to new conclusions, some of which could have been partly implied already from the data in chapter 3. However, they could not have been formulated within the confidence limits of that data. Consequently, the second part of this chapter will deal with exposing and discussing the implications of the new findings on the previous conclusions.

4.1 Gapping and Restructuring of the Fermi Surface

4.1.1 The Fermi Surface Reconstruction

The development of the Fermi surface of URu_2Si_2 in the $\Gamma - Z$ plane across the HO transition is discussed using figure 4.1. To cover the large area, data measured using excitation energies of 31 eV and 50 eV is combined.

Panel (a) shows the ordered state. At the Γ point, the Fermi surface consists of two sheets: a larger one at the border of the red area in the color plot, and a smaller one contained within. This is a consequence of the momentum gap displayed in figure 3.20. At higher momenta along (100) and (010), four Fermi petals with a diagonal distance of (0.91 ± 0.01) Å^{-1} are shown. This corresponds to the reciprocal lattice vector

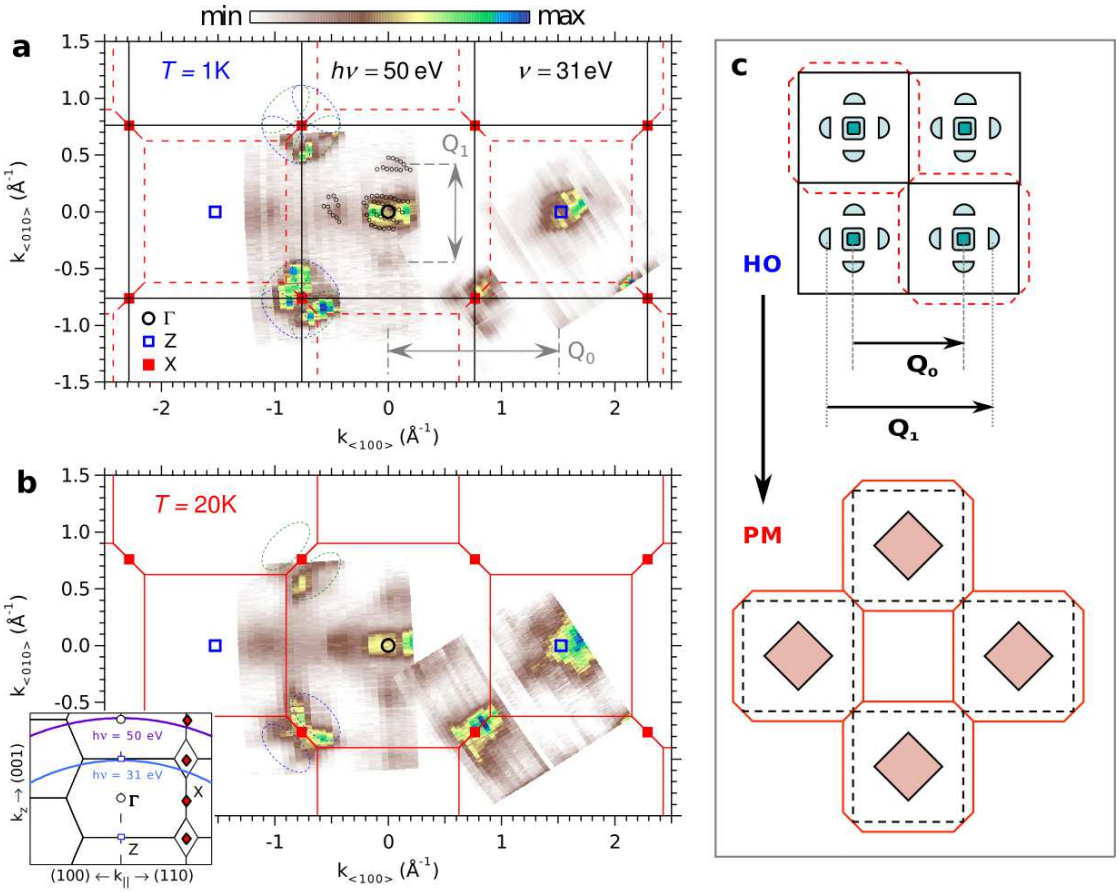

Figure 4.1: **Reconstruction by Q_0 of the electronic periodicity and Fermi-surface gapping** [part 1]. Panels (a,b): In-plane Fermi surface maps at 1 K and 20 K spanning the Γ, Z and X points. Each map combines data measured at 31 eV and 50 eV, reaching different points in the Brillouin zone as shown in the inset of (b). The double arrows show the vectors Q_1, connecting two Fermi petals, and Q_0, corresponding to a ST electronic periodicity. Open circles show the Fermi momenta from figure 1(b). The white blue/green dashed ovals around X in (a) and (b) are guides to the eye. Panel (c) explains the relation between the Brillouin zones and Fermi surfaces in the HO and the PM phase using a cartoon. *Images and captions for panels (a,b) extracted from [76].*

$Q_1 = (0.6, 0, 0)$.

Panel (b) shows the paramagnetic state. The main difference here is that while there is still significant intensity closely around Γ, the four petals separated by Q_1 have disappeared. Instead, a large diamond-shaped Fermi sheet is connecting the reciprocal space points at which previously the petals were found. In this particular color scale, it is observed as a faint intensity.

At the X point, the spectral intensity can be described by four overlapping ovals forming a 4-fold symmetric buckle structure in the HO state. In the paramagnetic state, it is more compatible with a two-fold symmetric structure composed of ovals aligned along the (110) direction. Additionally, the similarity between the distribution of spectral intensity between Γ and Z in panel (a), *not* given in panel (b), suggests that details of the electronic structure become simple-tetragonal symmetric below 17.5 K. This is illustrated in panel (c), where a cartoon explains how the body-centered and simple tetragonal Brillouin zones, and their respective Fermi surfaces, are related to one another.

4.1.2 The Q_1 Excitations and Gapping

An interband gap $\Delta_P \approx 5$ meV, compatible with the 4 meV reported by neutron scattering, opens in the HO between the lower and the higher part of the hybridized bands at the high-k wings of QP_1. This is illustrated in figure 4.2, panels (c–f), explaining the reconstruction of the Fermi surface.

In the PM phase, in panels (d) and (h), a structure of two bands is shown, anti-crossing at the Fermi level, separated by Q_1. The band structure is sketched by black dashed lines in panel (d). This structure results in the large diamond-shaped Fermi sheet, encompassing the four petals in the paramagnetic phase, and providing the faint intensity at E_F in figure 4.1(b).

During the HO transition, shown in (c) and (g), a degeneracy is lifted at the anti-crossing point of the bands, opening a gap below E_F. The result is a changed dispersion, indicated by the blue lines, shaping the familiar "M"-like QP_1. The momentum gap (section 3.4.1) gives rise to the double Fermi-sheet structure at the tips of the "M". The dropping of an electron-like band pushes the heavy high-k wings of QP_1 below E_F, in the process also gapping large parts of the Fermi diamond (gap size $\Delta_{HS} \approx 7$ meV). This is illustrated in panels (g) and (h). The Fermi petals are created as demonstrated in (c), by the dipping of a small electron-like pocket below E_F. Q_1 magnetic excitations are possible from the occupied lower part of the band hybridization into the thermally depopulated region at E_F, as indicated by the black arrow. In the HO phase, the excitations cross the energy gap of $\Delta_P \approx 5$ meV.

4.1.3 The Q_0 Symmetry Change

Although Q_1 is directly involved in the Fermi surface reorganization, it appears that the Q_0 vector, connecting neighboring Γ and Z points of the body-centered tetragonal lattice, corresponds to the actual symmetry of the HO transition. This can be observed along the $k_\perp$ direction in figure 4.3. Panels (a) and (c) show a cut through the URu_2Si_2 Fermi surface obtained scanning along $k_z = k_{(001)}$ by tuning the energy of the light source between 20 eV and 33 eV.

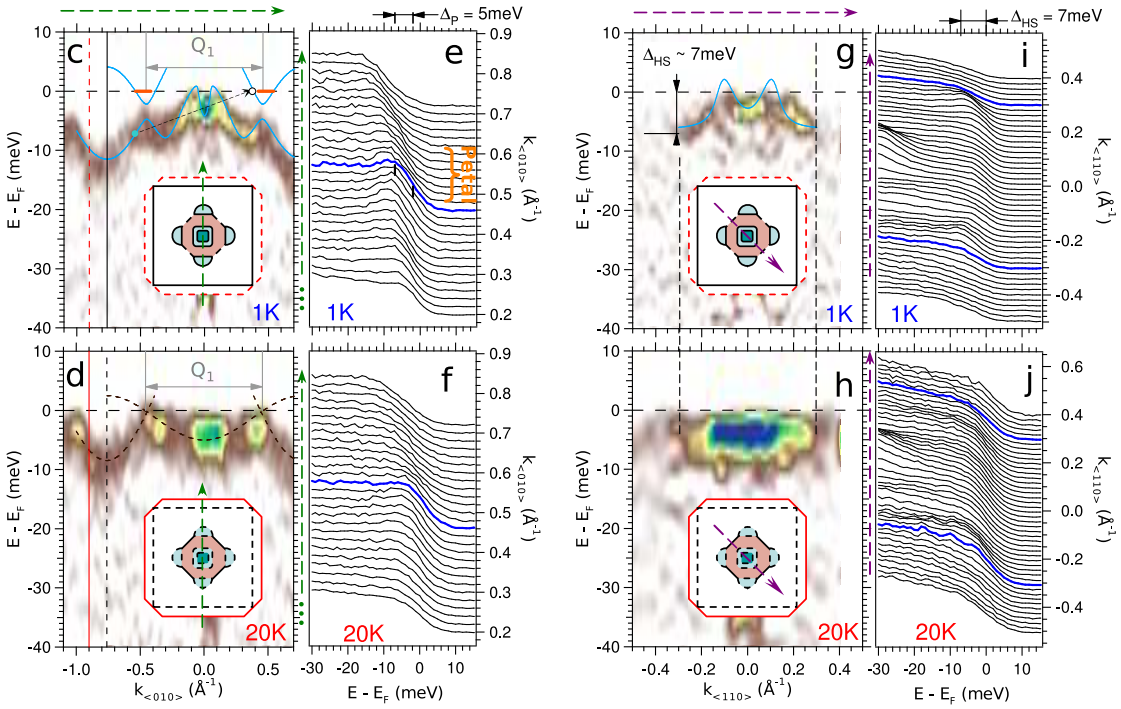

Figure 4.2: **Reconstruction by $\mathbf{Q}_0$ of the electronic periodicity and Fermi-surface gapping** [part 2]. Panels (c,d): ARPES dispersions (second derivative) at 1 K and 20 K, respectively, measured along the (010) as shown by the dashed green arrows in the insets. The black and red lines denote, respectively, the borders of the ST and BCT Brillouin zones. Blue curves in (c) and dashed brown curves in (d) are guides to the eye. In (c) the orange dashes mark the experimental location of the petals, whose intensity is too small to be apparent in this figure. Panels (e,f): raw EDCs from (c,d) zooming into the region where the petals form. Spectra in blue correspond to $k_{\|} = \mathrm{Q}_1/2$. Panels (g,h): same as (c,d) measured along (110) as shown by the dashed purple arrows in the insets. Dashed black lines are the Fermi momenta in the PM state. The blue curve in (g) is a fit serving as a guide to the eye (*details in [76]*). Panels (i, j): raw EDCs from (g, h). Spectra in blue show the Fermi momenta in the PM state. *Images and caption from [76].*

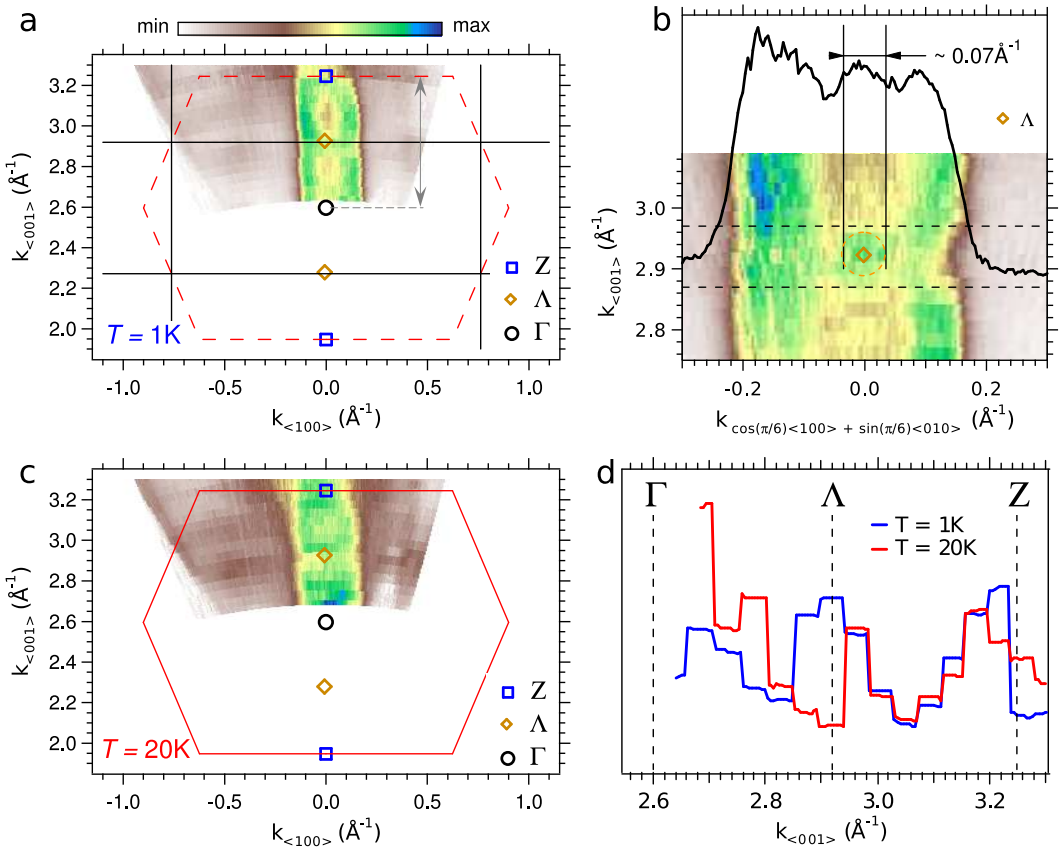

Figure 4.3: **Hidden-order changes in the electronic structure along (001).** Panel (a): Fermi surface map in the (100) - (001) plane at 1 K. The double arrow defines the ST periodicity along *c*. Panel (b): evidence of a new Fermi sheet, the 'lentil', illustrated with a different set of data using a smaller step in photon energy. The orange dashed oval is a guide to the eye. The black curve shows the intensity integrated between the two black dashed lines on the Fermi map. Note that the orientation in the *a*-*a* plane is, here, 30° with respect to (100), corresponding to the Fermi surface maps of figure 4.1. Panel (c): Fermi surface map in the (100) - (001) plane at 20 K. The distribution of spectral weight at the Fermi level is not anymore symmetric with respect to Λ. Panel (d): momentum distribution curves integrated from data of panels (a, c) in the interval $k_{(100)} = 0 \pm 0.05$ Å^{-1}. The distribution of spectral weight is symmetric with respect to Λ only in the HO. *Images and caption from reference [76].*

In the PM phase [panel (c)], the intensity distribution around the Λ point is not uniform. This is not required by the lattice symmetry. In the HO phase, however, the intensity is redistributed uniformly around this point. This is best visible from the MDCs in panel (d): signal intensity around the high-symmetry point is well within the expectations for a simple-tetragonal Brillouin zone in the ordered state (blue curve), while the PM state (red curve) shows large differences between the regions above and below the Λ point. An interesting detail of the shape of the Fermi surface is revealed in panel (b) by a HO data set measured with a higher resolution: the intensity is reshaped to resemble two ovals, each stretching roughly from the Γ (respectively Z) point, to Λ. There the ovals intersect creating a small "lentil" enclosed in the larger structure. This sheet is associated with the ν branch from Shubinkov–de Haas experiments (section 1.2.5).

4.1.4 Summary of the Reconstruction

"Excellent correspondence" [76] is found between ARPES and Subnikov–de Haas, mapping the sheets in the HO phase between the experimental methods as follows:

- the outer central square as the α sheet from SdH, and
- the inner central square as the γ sheet—these two sheets correspond to the momentum gap of QP_1 (section 3.4.1);
- the 4 petals along (100) as the β sheet, with in-plane crystal symmetry—this explains the splitting of the SdH signal when magnetic field is rotated from the c to the a axis;
- the small lentil at Λ as the ν sheet.

During the reconstruction of the large diamond to the smaller 4-fold pocket structure, a large part of the Fermi surface is gapped, preserving at most 40% of its original size. The following gaps were identified here by ARPES:

- $\Delta_{HS} \approx 7$ meV, the gap that occurs during the restructuring of the large diamond at Γ to the 4 small petals, and suppresses 60% of this Fermi sheet. This is in good agreement with [6], which attributed a 58% reduction of the Sommerfeld coefficient to the opening of a 10 meV gap.
- $\Delta_P \approx 5$ meV, the gap in the Q_1 magnetic excitations, triggered by the lifting of degeneracy of the anti-crossing bands upon the transition from body-centered to simple tetragonal crystal symmetry.

4.2 Implications

4.2.1 Symmetry Changes and Fermi Surface Gapping

The experiments confirm that Q_0 is the ordering vector behind the transition, making the electronic structure at Γ and Z similar in the HO phase. This also effectively changes the symmetry of the X point and its Fermi surface from 2- to 4-fold. The process is accompanied by a reconstruction of the heavy-fermion bands stretching along the

$\Gamma-X-\Gamma$ diagonal along (110). At least 60% of the large pocket are thus gapped, creating the four Fermi petals separated by Q_1. Relating to neutron scattering data [48, 53], the 5 meV gap at the petals in figure 4.2(c) implies that a large part of the spin excitations become unavailable. Together the gaps explain why the specific heat coefficient drops in the HO phase: there are simply less states to scatter to, as discussed in section 3 in the context of quasi-particle life time. However, for a formal confirmation that the Q_1 excitations, as reported by neutron scattering, are indeed attributed to interband excitations at the Fermi petals, an autocorrelation analysis far beyond the scope of this review is required.

It is still debated [76, 81, 82] whether a full crystal symmetry change from body-centered to simple tetragonal is taking place, or only specific components of the electronic structure adopt a simple tetragonal symmetry. For example, several issues (discussed in [75, 76]) in the intensity distribution of the Fermi surface map at the X-point and along k_z are incompatible with nesting as required by conventional density waves. Future experimental efforts should thus be directed to answer this question. In particular, since ARPES is a very surface-sensitive technique, the role which the surface Brillouin zone may play in the band mapping experiments needs to be considered.

4.2.2 Impact on the Kondo Lattice Considerations

The He-I_α Fermi surface shape at X (section 3.3.1) is called into debate by the fact that Γ and Z become similar in the HO phase. However, the symmetry of the X point pocket does not interfere with the conclusions from chapter 3. The arguments for the evolution of the HO on top of an already developed Kondo lattice rely on the fact that the hybridization strength does not change across the transition. This observation remains valid. It was based on the interaction between heavy and light bands as presented in sections 3.3.1 and 3.4.1. The (lack of) change in the hybridization potential is robustly backed up by data and corresponding modeling at the X and Z points, not subject to restrictions imposed by the crystal symmetry or shape of the Fermi surface.

4.2.3 The Dual Nature of the HO Transition

A recent theory introduced in references [51, 69], exploiting the adiabatic continuity between LMAF and HO, and emphasizing their itinerant character, reproduces the experimental Fermi surface extremely well [76, 81]. This is remarkable, in particular because the theory underestimates experimental band dispersions and effective masses by one order of magnitude (section 3.3.2 and supplementary material of [76]). Apparently, itinerant *spd*-bands suffice to describe the Fermi surface shape, and thus the general properties of the HO transition. However, the data here stipulates that for details of the quasi-particle interactions, and correct values for the effective mass, "dual" intinerant-localized theories as attempted in references [52, 70, 78] are essential.

Chapter 5

Conclusion

5.1 Further Suggested Investigations

To complete the picture, many fine details of the band structure, in particular the dynamics of heavy bands close to the Fermi level, require additional efforts. For instance, the whereabouts of the "split" band from section 3.4.1, as well as some details of the band dispersions at high-symmetry points along k_z are obscured by the bright surface state. The electronic structure in the unoccupied region is not available to high-resolution ARPES experiments at all, and is probable to remain so for years to come. But even within current capabilities, the list of experiments to be performed includes better (higher resolution, extremely low-noise) band structure and 3D Fermi surface mapping. A targeted investigation of small features, such as the lentil forming at Λ below T_{HO}, would render the documentation of the Fermi surface reconstruction more complete. Together with calculations for the magnetic susceptibility and transition matrix elements, the data could also be used for quantitative comparison of the ARPES data with inelastic neutron scattering experiments. Systematic analysis of the temperature dependency of the gaps would provide a good testing ground for emerging theories.

Finally, HO is a precursor for the SC phase: Fermi surface topology of the HO could help understand the order parameter of a highly exotic superconducting phase. This, in turn, would aid in the theoretical grasp of a possible quantum-critical point in URu_2Si_2 at $p = 0.5$ GPa.

5.2 Summary

An essential dichotomy of the 30 year old riddle of the "hidden-order" of URu_2Si_2 was the question of whether itinerant carriers or rather localized magnetic moments were responsible for the phase transition. The question finally received the irrefutable answer that both are to be considered in 2009, when the Paris / Würzburg team offered evidence [57] for a Fermi surface reconstruction driven by itinerant bands of heavy quasi-particles. But many details of the electronic structure changes, including the location of the gaps, the involved symmetries, and finally the mechanism responsible for the reorganization, were not clear. Several generations of momentum-integrated data from optical and electrical transport experiments, thermodynamics, and Fermi surface probing, suggested an intimate connection between Kondo elements in URu_2Si_2 and the mysterious 2^{nd} order

phase transition. But ultimately, the nature of this connection, whether it is causal or merely incidental with the HO transition, remained speculative.

Continuing the ARPES experiments within the Paris / Würzburg group, in this thesis band hybridizations setting in already above the lattice coherence temperature of URu_2Si_2 were demonstrated. The itinerant quasi-particles with large effective masses, interacting via a potential in the range of 10 meV, remain unchanged across the HO transition, documenting that the new order cannot represent the *onset* of lattice coherence in URu_2Si_2. Instead, the Kondo lattice merely sets the stage for the reordering at 17.5 K, with the transition itself representing an instability of the quasi-particle Fermi surface. The resulting energy gap at the Fermi level as a result of an electronic structure reconstruction is then in perfect agreement with differently focused ARPES experiments of competing groups. The latter attest a drastically increased life time of the quasi-particles at low temperature.

Finally, the work in this thesis laid ground for the momentum-resolved investigation of the Fermi surface reconstruction. The interplay between QP_1 and QP_2 is hereby the main ingredient of a process leading to the gapping of at least 60% of the solid's carriers. A large square-like sheet encompassing the Γ point is reorganized into four smaller pockets. The changes are driven by the reciprocal lattice vector Q_0, which connects neighboring Γ and Z points of the body-centered tetragonal reciprocal lattice. This makes the high-symmetry points similar in the HO phase and more compatible with a simple tetragonal symmetry. As an accompanying effect, interband excitations separated by the Q_1 reciprocal space vector become gapped in full agreement with other experimental data.

At this stage, the understanding of the "adiabatic continuity" between HO and LMAF, the involved symmetries and Fermi surface properties appears advanced. The documented interplay between light bands and heavy f-electrons imposes strong restrictions on theoretical models. While essential details regarding the mechanism behind the HO transition still remain concealed, crucial questions regarding the symmetry, gaps, and entropy loss were answered by modern momentum-resolved experiments [76, 81, 82]. These may arguably represent the verge to a 4^{th} generation of URu_2Si_2 research. The "hidden-order", though still hidden, is conspicuously losing its veils.

5.3 Acknowledgments

The support of the following people is acknowledged and highly appreciated: my formal thesis advisor Dr Friedrich Reinert; the "father" of this project and very close advisor Dr Andres Santander; the equally-close co-worker on this project Cedric Bareille; the sample manufacturer Dr Pascal Lejay; my girlfriend Anna Reis, and my family Anca, Maria and Stelian; my colleagues directly involved in this project Holger Schwab, Dr Andreas Nuber, Dr Markus Klein, Dr Frank Forster, Dr Chul-Hee Min; the colleagues not directly involved, too numerous to name; scientists who delivered valuable insight through discussions and hints, like Dr Piers Coleman, Dr Thomasz Durakiewicz, Dr Premala Chandra, and many others with countless contributions and remarks.

Beyond the invaluable moral support, the financial assistance of my family and my girlfriend after the formal expiry of the contract with the Universität Würzburg for the time of the writing of the manuscript is greatly appreciated. The permission of Dr.

Thomas Schmidt to use the office infrastructure of his workgroup (office space, printer, internet connection) is greatly appreciated. I also thank his colleagues for their support, in particular Marcel Springer for more than just the coffee.

Appendix A

About Quantum Phase Transitions

This section, which is oriented after and inspired by Subir Sachdev's introductory section to *"Quantum Phase Transitions"* [71], gives a short overview over the topic of Quantum Phase Transitions. It aims to introduce the concepts of *quantum criticality*, *order parameters*, and how classical phase transitions like the "hidden-order" of URu_2Si_2 may evolve from *quantum critical points*. The goal is to convey the importance of identifying an order parameter for the HO.

A.1 What Is a Quantum Phase Transition

Consider a solid-state quantum system at temperature $T = 0$. Its Hamiltonian $H(g) = H_0 + gH_1$ on a lattice, observed as a a function of a dimensionless parameter g, be composed of the operators H_0 and H_1. If H_0 and H_1 commute, then they can be simultaneously diagonalized, and their eigenfunctions are independent of g. However, the eigenvalues, i.e. the energy levels in the system, will generally still depend on g.

Now consider adjusting the coupling g smoothly from 0 to higher values. There may exist a value $g = g_c$ where the ground level and first excited level cross, making the ground level the new first excited state, and vice-versa. In other words, the ground state of the system abruptly changes at $g = g_c$, leading to a non-analicity in the ground level energy with respect to g. This non-analicity, the *phase transition*, is visualized in A.1(a). Usually, it is accompanied by drastic qualitative changes in the physical properties of the solid, like lattice geometry, electronic structure, low energy physics, and electronic correlations in the ground state, etc.

A.2 Characteristic Energy, Length, Time Scales

With what is called a 2^{nd}-order phase transition, typical energy Δ and length ξ scales are associated. They are a consequence of the microscopic mechanism triggering the reorganization of the system, but show a powerlaw dependency on g with *universal* critical exponents:

$\Delta \propto J|g - g_c|^a$, is the smallest energy excitation above the ground state at zero temperature, related to a microscopic interaction J, and vanishing ($\to 0$) for $g \to g_c$

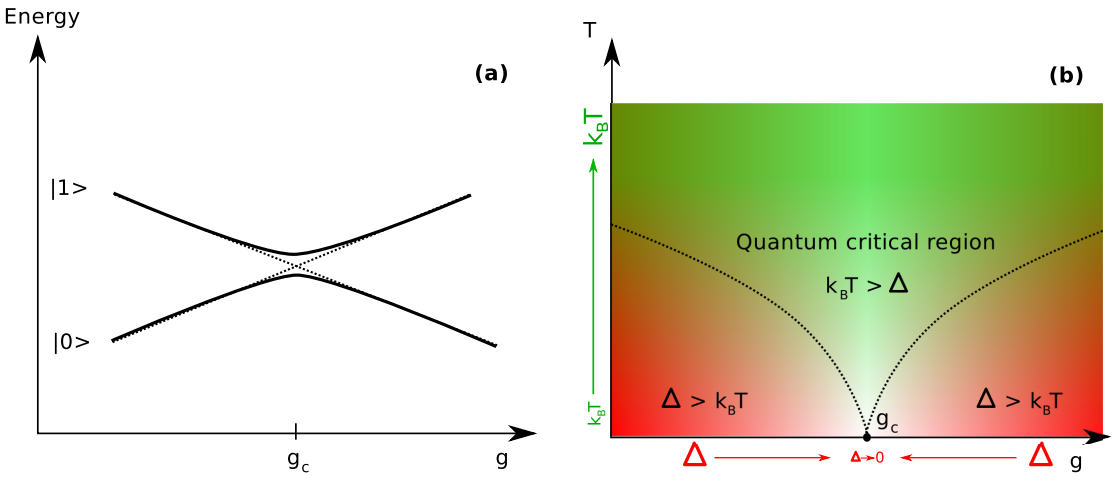

Figure A.1: **Quantum Phase Transitions and Quantum Criticality.** Panel (a) shows a quantum system evolving with a tuning parameter g. The former ground level $|0\rangle$ and first excited level $|1\rangle$ swap order at a critical $g = g_c$, changing the symmetry of the system. Panel (b) shows the quantum critical point at $g = g_c$ and $T = 0$ evolving into the quantum critical region (green area) at $T > 0$, where the subtle interplay between quantum and thermal fluctuations determine the physics of the system.

$\xi^{-1} \propto \Lambda|g - g_c|^b$, with ξ determining the length scale on which correlations decay exponentially, is related to a momentum cutoff Λ and is diverging ($\to \infty$) for $g \to g_c$.

Quantum phase transitions arise in a variety of circumstances supported by various microscopic mechanisms, for example from high-energy physics and the Higgs mechanism to meV-scale effects in solid state systems. But the universal behavior and scaling permits the formulation generalized theories, independent on the microscopic origin of the transition.

The situation for real-life systems differs from the considerations formulated above for the theoretical case of $T = 0$. Experimentally achievable systems are always measured at $T > 0$, even if T may become very small. For a theoretical grasp, systems are usually described by expansion around $g = g_c$ and $T = 0$. In this context, another energy scale, the available thermal energy k_BT, becomes important. Its connection to the lowest system excitation Δ brings into consideration two regimes at $T > 0$, visualized in A.1(b):

$\Delta > k_BT$ (red) available thermal energy is small compared to the excitation levels available in the system. This means that small (thermal) perturbations of the system in equilibrium state usually need a long time to relax again into a local equilibrium. The system is effectively classic.

$\Delta < k_BT$ (green) fast relaxation from small perturbations possible, equilibration time $\tau_{\text{eq}} \approx \hbar/k_BT$ independent of the microscopic mechanism. Here, the interplay between thermal and quantum-mechanical fluctuations is essential for the dynamics of the system. Characteristic for this *quantum critical region* is the multitude of phases developing close to one another, each representing a delicate equilibrium between the control parameters and quantum mechanical fluctuations.

The *quantum critical point* (QCP) at $T = 0$ and $g = g_c$ cannot be probed experimentally, but its properties are significant for the developing phases in the quantum critical region. Its theoretical understanding and modeling are therefore crucial.

A.3 Quantum Field Theories and the Order Parameter Concept

A.3.1 Mean-Field Theory

One approach of treating phase transition, classical or quantum ones, is the mean-field theory. It models local interactions by looking at a quantum mechanical observable at the i-th lattice site, in the average field of its neighbors. For example in the Ising model the observable is the expectation value of the spin. The average ferromagnetic moment is defined as $N_0 = \langle \sigma_j^z \rangle$. The local Hamiltonian H_i then, modelling the interactions of the i-th site with its neighbors, takes the latter into account only through N_0, as $H_i \simeq \text{const} \cdot K N_0 \sigma_i^z$. At a critical value of the tuning parameter $K = K_c$, a symmetry of the system is spontaneously broken and the system settles for a new ground state—a phase transition occurs.

A.3.2 Landau Theory and the Order Parameter

Landau theory models the physics in a more general manner, employing quantum field theoretical methods. Instead of averaging over discrete points (N_0 in the Ising case above), in Landau theory, the interaction is modeled into a continuum field $\Phi(x)$, representing a coarse average over the observable, varying over distances large with respect to the coherence length ξ. Here x is a space coordinate with the same dimension as the lattice, and the *order parameter* Φ itself may be real or imaginary, a scalar, or a multiple-component vector, spinor, etc., depending on the underlying microscopic mechanism. The normal state is the characterized by an order parameter which is constantly 0, while in the ordered state, below a transition temperature T_c, $\Phi(x)$ abruptly becomes finite:

$$\Phi(x) = \begin{cases} 0, & \text{for } T > T_c \\ |\Phi_0|, & \text{for } T < T_c \end{cases} \tag{A.1}$$

The strength of this method lies within the fact that the quantum field theory defined by the phase transition is also universal. Macroscopic properties of the system at scales larger than Δ and ξ become independent of the particular nature of the microscopic interactions. This is related to the universal power-law dependency of the scales. Landau theory thus formulates the physics in a form that depends only dimensionless parameters, without intrinsic energy or momentum scales, independent from microscopic couplings. Ultimately, constraints on the theory are imposed only by general properties like the symmetry of the order parameter, conserved quantities, and space dimensionality.

Finally, a two-step approach is commonly used for theoretical investigation of quantum phase transitions: first, the quantum field theory of the physical system of interest is identified; second, the properties of the field theory at finite temperatures are described, modeling the system in the vicinity of the QPT by expansion around the quantum critical point.

Appendix B

Data Analysis and Visualization Methods

B.1 Fermi-Dirac Normalization of Angle-Resolved Data

Following a well established procedure [33], thermally occupied states up to about $5k_BT$ above E_F were visualized by normalizing spectra by the Fermi-Dirac distribution (FDD). Precise knowledge of the Fermi level and line broadening (owing to temperature and resolution) are necessary. The typical precision of the E_F determination in this thesis ($\Delta E \leq 1$ meV) proved sufficient. FDD broadening was derived directly from fits to reference spectra.

The noise above E_F provides a good estimate for the quality of the FDD normalization, provided that the background intensity was correctly subtracted. For polycrystalline samples, this is usually easy to accomplish. Background can be obtained directly from the unoccupied area above $E_F + 5k_BT$.

This procedure can be applied to single crystals, too, with some precautions. For instance, the momentum-dependent intensity normalization is usually performed by calibrating a lateral intensity distribution function using an angle-resolved scan of a polycrystalline sample. This intensity distribution function is then used to normalize the lateral intensity in the single-crystalline samples one wishes to investigate. Small differences in the lateral intensity distribution between the reference sample and the single-crystal samples will thus result in slight imperfections in the momentum-dependent intensity distribution after normalization. These are well within boundaries required to analyze band data.

However, when performing the FDD-normalization on an angle-resolved scan, the imperfections of the lateral intensity distribution will result in a slightly different background for each EDC of the scan, and thus for a different noise structure at $E \geq 5k_BT$. EDC intensity there may diverge non-uniformly, with bias towards positive (or negative) intensity in the region where the Fermi-Dirac function is numerically zero. In such cases, to judge the quality of the FDD normalization process, typically the "overall" noise structure must be considered. This is easy to achieve when visualizing 2D FDD-normalized scans: the data should still show a well balanced distribution of points diverging into negative/positive intensities. However, if data is shown as EDCs, integrated over selective regions of crystal momentum, then slight negative or positive signal bias may add

up to a significant noise in the corresponding EDCs. In this case, the noise structure after the FDD normalization may show signs of a bad FDD (e.g. too early unilateral divergence towards positive values), even if the FDD was, in fact, performed correctly. To avoid this, the quality of the FDD normalization performed for this thesis was always cross-checked using the angle-resolved version of the data.

B.2 The 2nd Derivative Method

In 2D ARPES data with low count rate or from samples with an aged surface, the 2nd derivative can be used to increase contrast at the expense of resolution. For this, raw photoemission spectra were convolved with a two-dimensional Gaussian of typical widths in the range $\sigma_E = 2 \ldots 20$ meV and $\sigma_k = 0.01 \ldots 0.1$ Å^{-1}. The ideal value to choose for the widths depend on the band structure elements to be analyzed, data resolution, and signal-to-noise ratio.

For displaying, two possibilities of intensity scaling were used: (**i**) plot only negative intensities (corresponding to peaks in the raw spectra), cutting off positive intensities. This allows for an easy mapping of bands (intensity ⇔ band; no intensity ⇔ no band) but is error-prone with very noisy data, where random correlations of intensity create structures in the 2nd derivative data that do not correspond to any bands in the raw spectra (reference [49]). (**ii**) Plot both negative and positive intensities, adjusting the lower/upper limits of the color scale such that the features of interest (i.e. the band dispersions) are visible within their surroundings; this method was employed mostly for the wide energy range scans in sections 2.2 and 3.3.2, where the contrast in the data was particularly bad.

B.3 Resolution of the Würzburg Xe-I Lamp

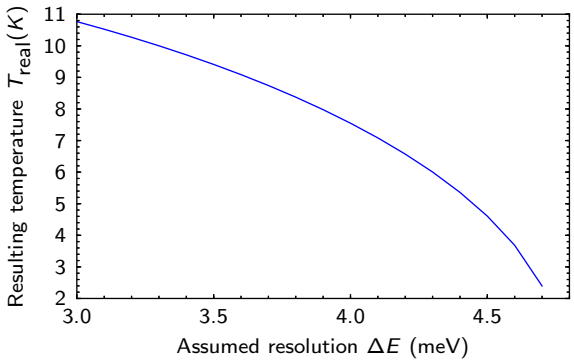

Figure B.1: **Estimated resolution of the Xe-lamp.** A lower bound for the Xe-I setup is estimated by showing the temperature T_{real} in dependency of a presumed resolution ΔE in the range $3 \ldots 6$ meV. For the likely sample temperature of $T \geq 7$ K, the experimental resolution needs to be $\Delta E \leq 4$ meV. Resolutions larger than 4.8 meV would result in unphysical temperatures. See main text for argumentation details.

Resolution of the Xe-I lamp in the Würzburg laboratory setup had not been formally

determined as the URu_2Si_2 experiments were performed. For this reason, the following estimation is used as replacement.

Measurement temperature is determined from the k_BT parameter of a Fermi-Dirac distribution function fitted to ARPES data of a poly-crystalline reference sample, as in [45]. The relation between the real sample temperature T_{real}, and the effectively measured temperature T_{eff} influenced by the instrumental resolution ΔE, is given by [45]:

$$T_{\text{eff}} = \sqrt{T_{\text{real}}^2 + (\Delta E/4k_B)^2}. \tag{B.1}$$

The lowest temperature ever measured with He-I_α on URu_2Si_2, in which case the resolution for the Wüzburg setup was known to be 5.18 eV from previous experiments [41, 57], was $T_{\text{real}} \geq 7K$. The lowest attainable effective temperature parameter ever fitted against a reference sample measured with Xe-I was $k_BT_{\text{eff}} = 0.001194$ eV The real temperature for a series of assumed resolutions between 3 meV and 6 meV is plotted in figure B.1. The following observations apply:

- The calculation gives unphysical results (imaginary temperature) for resolutions larger than $\Delta E_{\text{max}} = 4.8$ meV.
- The corresponding URu_2Si_2 data is not compatible with temperatures greater than 10 K. This refers both to the resolution of the Xe-I scans as estimated by eye sight in comparison to the approximately 100 cleaves measured with other light sources, and to the degree of binding energy shifting of HO-related features (discussed in detail in section 3.4). This renders $\Delta E_{\text{min}} = 3.3$ meV as a lower bound of the resolution
- If the real sample temperature is assumed as $T_{\text{real}} \approx 7$ K, consistent with the lowest temperature achieved during He-I_α experiments, then the Xe-I resolution is $\Delta E \approx 4$ meV.

Since the first URu_2Si_2 experiments in Würzburg (2007), the system was not capable of achieving a temperature lower than 7 K. In consequence of these facts, 4 meV was used as the most probable lower bound for the resolution in the Xe-I lamp setup, within the constraints imposed by the other experimental parameters.

Bibliography

[1] N. W. Ashcroft and N. D Mermin. *Solid State Physics*. 1976.

[2] P. M. Echenique and J. B. Pendry. "The existence and detection of Rydberg states at surfaces". In: *Journal of Physics C: Solid State Physics* 11.10 (1978), pp. 2065–2075.

[3] F. J. Himpsel and D. E. Eastman. "Observation of a Λ_1-Symmetry surface state on Ni(111)". In: *Phys. Rev. Lett.* 41.7 (1978), pp. 507 –512.

[4] M. J. Cooper. "Compton scattering and electron momentum determination". In: *Reports on Progress in Physics* 48.4 (1985), p. 415.

[5] T. T. M. Palstra, A. A. Menovsky, J. van den Berg, A. J. Dirkmaat, P. H. Kes, G. J. Nieuwenhuys, and J. A. Mydosh. "Superconducting and Magnetic Transitions in the Heavy-Fermion System URu_2Si_2". In: *Phys. Rev. Lett.* 55.24 (Dec. 1985), pp. 2727–2730.

[6] M. B. Maple, J. W. Chen, Y. Dalichaouch, T. Kohara, C. Rossel, M. S. Torikachvili, M. W. McElfresh, and J. D. Thompson. "Partially Gapped Fermi Surface in the Heavy-Electron Superconductor URu_2Si_2". In: *Phys. Rev. Lett.* 56.2 (Jan. 1986), pp. 185–188.

[7] M. Ortuo and P. M. Echenique. "Phase shifts, image planes, and surface states at metal surfaces". In: *Phys. Rev. B* 34.8 (1986), pp. 5199–5204.

[8] T. T. M. Palstra, A. A. Menovsky, and J. A. Mydosh. "Anisotropic electrical resistivity of the magnetic heavy-fermion superconductor URu_2Si_2". In: *Phys. Rev. B* 33 (9 May 1986), pp. 6527–6530.

[9] W. Schlabitz, J. Baumann, B. Pollit, U. Rauchschwalbe, H. M. Mayer, U. Ahlheim, and C. D. Bredl. "Superconductivity and magnetic order in a strongly interacting fermi-system: URu_2Si_2". In: *Zeitschrift für Physik B Condensed Matter* 62 (2 1986), pp. 171–177.

[10] U. Walter, C.-K. Loong, M. Loewenhaupt, and W. Schlabitz. "Evidence of a magnetic gaplike excitation in URu_2Si_2". In: *Phys. Rev. B* 33.11 (June 1986), pp. 7875–7878.

[11] C. Broholm, J. K. Kjems, W. J. L. Buyers, P. Matthews, T. T. M. Palstra, A. A. Menovsky, and J. A. Mydosh. "Magnetic excitations and ordering in the heavy-electron superconductor URu_2Si_2". In: *Phys. Rev. Lett.* 58.14 (Apr. 1987), pp. 1467–1470.

[12] M. W. McElfresh, J. D. Thompson, J. O. Willis, M. B. Maple, T. Kohara, and M. S. Torikachvili. "Effect of pressure on competing electronic correlations in the heavy-electron system URu_2Si_2". In: *Phys. Rev. B* 35 (1 Jan. 1987), pp. 43–47.

[13] J. Schoenes, C. Schönenberger, J. J. M. Franse, and A. A. Menovsky. "Hall-effect and resistivity study of the heavy-fermion system URu_2Si_2". In: *Phys. Rev. B* 35.10 (Apr. 1987), pp. 5375–5378.

[14] D. A. Bonn, J. D. Garrett, and T. Timusk. "Far-Infrared Properties of URu_2Si_2". In: *Phys. Rev. Lett.* 61 (11 Sept. 1988), pp. 1305–1308.

[15] D.A. Bonn, R.J. Klassen, J.D. Garrett, T. Timusk, J.L. Smith, and Z. Fisk. "Far infrared optical properties of heavy fermion superconductors: UBe_13 and URu_2Si_2". In: *Physica C: Superconductivity* 153–155, Part 1.0 (1988), pp. 453–454.

[16] D. E. MacLaughlin, D. W. Cooke, R. H. Heffner, R. L. Hutson, M. W. McElfresh, M. E. Schillaci, H. D. Rempp, J. L. Smith, J. O. Willis, E. Zirngiebl, C. Boekema, R. L. Lichti, and J. Oostens. "Muon spin rotation and magnetic order in the heavy-fermion compound URu_2Si_2". In: *Phys. Rev. B* 37 (7 Mar. 1988), pp. 3153–3158.

[17] A. LeR. Dawson, W. S. Datars, J. D. Garrett, and F. S. Razavi. "Electrical transport in URu_2Si_2". In: *J. Phys.: Cond. Mat.* 1 (Apr. 1989), pp. 6817–6828.

[18] T. E. Mason, B. D. Gaulin, J. D. Garrett, Z. Tun, W. J. L. Buyers, and E. D. Isaacs. "Neutron-scattering measurements of long-range antiferromagnetic order in URu_2Si_2". In: *Phys. Rev. Lett.* 65 (25 Dec. 1990), pp. 3189–3192.

[19] C. Broholm, H. Lin, P. T. Matthews, T. E. Mason, W. J. L. Buyers, M. F. Collins, A. A. Menovsky, J. A. Mydosh, and J. K. Kjems. "Magnetic excitations in the heavy-fermion superconductor URu_2Si_2". In: *Phys. Rev. B* 43.16 (June 1991), pp. 12809–12822.

[20] N. Fischer, S. Schuppler, R. Fischer, Th. Fauster, and W. Steinmann. "Image states and the proper work function for a single layer of Na and K on Cu(111), Co(0001), and Fe(110)". In: *Phys. Rev. B* 47.8 (1993), pp. 4705–4713.

[21] Bansil Z. *Naturforsch. Teil A.* 1993, p. 165.

[22] R. Escudero, F. Morales, and P. Lejay. "Temperature dependence of the antiferromagnetic state in URu_2Si_2 by point-contact spectroscopy". In: *Phys. Rev. B* 49 (21 June 1994), pp. 15271–15275.

[23] G.M. Luke, A. Keren, L.P. Le, Y.J. Uemura, W.D. Wu, D. Bonn, L. Taillefer, J.D. Garrett, and Y. Onuki. "Muon spin relaxation in heavy fermion systems". English. In: *Hyperfine Interactions* 85.1 (1994), pp. 397–409.

[24] P. Santini and G. Amoretti. "Crystal Field Model of the Magnetic Properties of URu_2Si_2". In: *Phys. Rev. Lett.* 73.7 (Aug. 1994), pp. 1027–1030.

[25] E. Bertel and N. Memmel. "Promotors, poisons and surfactants: Electronic effects of surface doping on metals". In: *Appl. Phys. A* 63.6 (1996), pp. 523–531.

[26] R. Pietri, B. Andraka, R. Troć, and V. H. Tran. "Non-Fermi-liquid, magnetic, and Kondo behavior in the heavy-fermion system $U_2Cu_{17-x}Al_x$". In: *Phys. Rev. B* 56.22 (Dec. 1997), pp. 14505–14509.

[27] H. Ohkuni, Y. Inada, Y. Tokiwa, K. Sakurai, R. Settai, T. Honma, Y. Haga, E. Yamamoto, Y. Onuki, H. Yamagami, S. Takahashi, and T. Yanagisawa. "Fermi surface properties and de Haas–van Alphen oscillation in both the normal and superconducting mixed states of URu2Si2". In: *Philosophical Magazine Part B* 79.7 (1999), pp. 1045–1077.

[28] Johan M. Carlsson and Bo Hellsing. "First-principles investigation of the quantum-well system Na on Cu(111)". In: *Phys. Rev. B* 61.20 (2000), pp. 13973–13982.

[29] J. D. Denlinger, G.-H. Gewon, J. W. Allen, C. G. Olson, M. B. Maple, J. L. Sarrao, P. E. Armstrong, Z. Fisk, and H. Yamagami. "Advances in photoemission spectroscopy of f-electron materials". In: *Elsevier Physics B* 281-282 (2000), pp. 716–722.

[30] A. Sekiyama, T. Iwasaki, K. Matsuda, Y. Saitoh, Y. Onuki, and S. Suga. "Probing bulk states of correlated electron systems by high-resolution resonance photoemission". In: *Nature* 403 (6768 2000), pp. 396 –398.

[31] P. Suortti, T. Buslaps, V. Honkimäki, C. Metz, A. Shukla, Th. Tschentscher, J. Kwiatkowska, F. Maniawski, A. Bansil, S. Kaprzyk, A. S. Kheifets, D. R. Lun, T. Sattler, J. R. Schneider, and F. Bell. "Fermi-surface and electron correlation in Al studied by Compton scattering". In: *Journal of Physics and Chemistry of Solids* 61.3 (2000), pp. 397 –401.

[32] J. D. Denlinger, G. H. Gweon, J. W. Alle, C. G. Olson, M. B. Maple, J. L. Sarrao, P. E. Armstrong, Z. Fisk, and H. Yamagami. "Comparative study of the electronic structure of XRu_2Si_2: probing the Anderson lattice". In: *Journal of Electron Spectroscopy and Related Phenomena* 117-118 (2001), pp. 347–369.

[33] D. Ehm, F. Reinert, G. Nicolay, S. Schmidt, S. Hüfner, R. Claessen, V. Eyert, and C. Geibel. "Electronic structure of $CeNi_2Ge_2$ investigated by angle-resolved photoemission and density-functional calculations". In: *Phys. Rev. B* 64.23 (Nov. 2001), p. 235104.

[34] K. Matsuda, Y. Kohori, T. Kohara, K. Kuwahara, and H. Amitsuka. "Spatially Inhomogeneous Development of Antiferromagnetism in URu_2Si_2: Evidence from S^{29i} NMR under Pressure". In: *Phys. Rev. Lett.* 87.8 (Aug. 2001), p. 087203.

[35] H. Amitsuka, K. Tenya, M. Yokoyama, A. Schenck, D. Andreica, F. N. Gygax, A. Amato, Y. Miyako, Ying Kai Huang, and J. A. Mydosh. "Inhomogeneous magnetism in URu_2Si_2 studied by muon spin relaxation under high pressure". In: *Physica B: Condensed Matter* 326 (Feb. 2003), pp. 418–421.

[36] F. Forster, G. Nicolay, F. Reinert, D. Ehm, S. Schmidt, and S. Hüfner. "Surface and interface states on adsorbate covered noble metal surfaces". In: *Surface Science* 532-535 (2003). Proceedings of the 7th International Conference on Nanometer-Scale Science and Technology and the 21st European Conference on Surface Science, pp. 160 –165.

[37] Springer Verlag Berlin/Heidelberg (Stefan Hüfner), ed. *Photoelectron Spectroscopy — Principles and Applications*. Springer Verlag, 2003.

[38] M. Nakashima, H. Ohkuni, Y. Inada, R. Settai, Y. Haga, E. Yamamoto, and Y. Onuki. "The de Haas–van Alphen effect in URu_2Si_2 under pressure". In: *Journal of Physics: Condensed Matter* 15.28 (2003), S2011.

[39] G. Nicolay, F. Reinert, F. Forster, D. Ehm, S. Schmidt, B. Eltner, and S. Hüfner. "About the stability of noble metal surface states during VUV-experiments". In: *Surf. Sci.* 543.1-3 (2003), pp. 47–56.

[40] K. Behnia, R. Bel, Y. Kasahara, Y. Nakajima, H. Jin, H. Aubin, K. Izawa, Y. Matsuda, J. Flouquet, Y. Haga, Y. Ōnuki, and P. Lejay. "Thermal Transport in the Hidden-Order State of URu_2Si_2". In: *Phys. Rev. Lett.* 94 (15 Apr. 2005), p. 156405.

[41] F. Reinert and S. Hüfner. "Photoemission spectroscopy–from early days to recent applications". In: *New Journal of Physics* 7.1 (2005), p. 97.

[42] A. Yamasaki, A. Sekiyama, S. Imada, M. Tsunekawa, A. Higashiya, A. Shigemoto, and S. Suga. "Bulk sensitive photoelectron spectroscopy with soft and hard X-rays: Soft X-ray ARPES toward high resolution HAXPES". In: *Nuclear Instruments and Methods in Physics Research A* 547.1 (2005), pp. 136 –150.

[43] H. Amitsuka, K. Matsuda, I. Kawasaki, K. Tenya, M. Yokoyama, C. Sekine, N. Tateiwa, T. C. Kobayashi, S. Kawarazaki, and H. Yoshizawa. "Pressure-temperature phase diagram of the heavy-electron superconductor URu_2Si_2". In: *Journal of Magnetism and Magnetic Materials* (2006).

[44] F. Forster, A. Bendounan, J. Ziroff, and F. Reinert. "Systematic studies on surface modifications by ARUPS on Shockley-type surface states". In: *Surface Science* 600.18 (2006). Berlin, Germany: 4-9 September 2005, Proceedings of the 23th European Conference on Surface Science, pp. 3870 –3874.

[45] D. Ehm, S. Hufner, F. Reinert, J. Kroha, P. Wolfle, O. Stockert, C. Geibel, and H. v. Lohneysen. "High-resolution photoemission study on low-T (sub K) Ce systems: Kondo resonance, crystal field structures, and their temperature dependence". In: *Phys. Rev. B* 76.4, 045117 (2007), p. 045117.

[46] F. Forster, A. Bendounan, F. Reinert, V.G. Grigoryan, and M. Springborg. "The Shockley-type surface state on Ar covered Au(111): High resolution photoemission results and the description by slab-layer DFT calculations". In: *Surface Science* 601.23 (2007), pp. 5595 –5604.

[47] Y. J. Jo, L. Balicas, C. Capan, K. Behnia, P. Lejay, J. Flouquet, J. A. Mydosh, and P. Schlottmann. "Field-Induced Fermi Surface Reconstruction and Adiabatic Continuity between Antiferromagnetism and the Hidden-Order State in URu_2Si_2". In: *Phys. Rev. Lett.* 98 (16 Apr. 2007), p. 166404.

[48] C. R. Wiebe, J.A. Janik, MacDougall G. J., G. M. Luke, J. D. Garrett, H. D. Zhou, Y.-J. Jo, L. Balicas, Y. Qiu, J. R. D. Copley, Z. Yamani, and W. J. L. Buyers. "Gapped itinerant spin excitations account for missing entropy in the hidden-order state of URu_2Si_2". In: *Nature Physics* 3 (Feb. 2007), pp. 96–100.

[49] F. L. Boariu. *Elecronic Structure of Low-Dimensional Actinides (Diploma Thesis).* EP2, Universität Würzburg, 2008.

[50] A. Villaume, F. Bourdarot, E. Hassinger, S. Raymond, V. Taufour, D. Aoki, and J. Flouquet. "Signature of hidden order in heavy fermion superconductor URu_2Si_2: Resonance at the wave vector $Q_0 = (1,0,0)$". In: *Physical Review B (Condensed Matter and Materials Physics)* 78.1, 012504 (2008), p. 012504.

[51] S. Elgazzar, J. Rusz, M. Amft, P. M. Oppeneer, and J. A. Mydosh. "Hidden order in URu_2Si_2 originates from Fermi surface gapping induced by dynamic symmetry breaking". In: *Nature Materials* 8 (Feb. 2009), pp. 337–341.

[52] K. Haule and G. Kotliar. "Arrested Kondo effect and hidden Order in URu_2Si_2". In: *Nature Physics* 5 (Nov. 2009), pp. 796–799.

[53] J. A. Janik, H. D. Zhou, Y-J. Jo, L. Balicas, G. J. MacDougall, G. M. Luke, J. D. Garrett, K. J. McClellan, E. D. Bauer, J. L. Sarrao, Y. Qiu, J. R. D. Copley, Z. Yamani, W. J. L. Buyers, and C. R. Wiebe. "Itinerant spin excitations near the hidden order transition in URu_2Si_2". In: *Journal of Physics: Condensed Matter* 21.19 (2009), p. 192202.

[54] M. Klein. *Starke Korrelationen in Festkörpern: von lokalisierten zu itineranten Elektronen (PhD Thesis)*. EP2, Universität Würzburg, 2009.

[55] J. Levallois, K. Behnia, J. Flouquet, P. Lejay, and C. Proust. "On the destruction of the hidden order in URu_2Si_2 by a strong magnetic field". In: *EPL (Europhysics Letters)* 85.2 (2009), 27003 (6pp).

[56] A. F. Santander-Syro. "Laue simulation of URu_2Si_2". In: *(private communication)* (2009).

[57] A. F. Santander-Syro, M Klein, F. L. Boariu, A. Nuber, P. Lejay, and F. Reinert. "Fermi-Surface instability at the 'hidden-order' transition of URu_2Si_2". In: *Nature Physics* 5 (Sept. 2009), pp. 637–641.

[58] A. Scheybal, K. Müller, R. Bertschinger, M. Wahl, A. Bendounan, P. Aebi, and T. A. Jung. "Modification of the Cu(110) Shockley surface state by an adsorbed pentacene layer". In: *Phys. Rev. B* 79 (2009), p. 115406.

[59] P. Aynajian, E. H. da Silva Neto, C. V. Parker, Y. Huang, A. Pasupathy, J. Mydosh, and A. Yazdani. "Visualizing the formation of the Kondo lattice and the hidden order in URu_2Si_2". In: *PNAS* 107.23 (June 2010), pp. 10383–10388.

[60] C. Bareille. *Structure électronique aux points X et Z de l'URu_2Si_2 autour de la transition d'ordre cachée (MSc Thesis)*. ESPCI, Université Paris-Sud, 2010.

[61] F. L. Boariu, A. Nuber, A. F. Santander-Syro, M. Klein, F. Forster, P. Lejay, and F. Reinert. "The surface state of URu_2Si_2". In: *Journal of Electron Spectroscopy and Related Phenomena* 181.1 (2010). Proceedings of International Workshop on Strong Correlations and Angle-Resolved Photoemission Spectroscopy 2009, pp. 82–87.

[62] E. Hassinger, G. Knebel, T. D. Matsuda, D. Aoki, V. Taufour, and J. Flouquet. "Similarity of the Fermi Surface in the Hidden Order State and in the Antiferromagnetic State of URu_2Si_2". In: *Physical Review Letters* 105.21 (Nov. 2010), 216409 ff.

[63] A. R. Schmidt, M. H. Hamidian, F. Wahl P.and Meier, A. V. Balatsky, J. D. Garrett, T. J. Williams, G. M. Luke, and J. C. Davis. "Imaging the Fano lattice to 'hidden order' transition in URu_2Si_2". In: *Nature* 465 (7298 2010), pp. 570–576.

[64] R. Yoshida, Y. Nakamura, M. Fukui, Y. Haga, E. Yamamoto, Y. Ōnuki, M. Okawa, S. Shin, M. Hirai, Y. Muraoka, and T. Yokoya. "Signature of hidden order and evidence for periodicity modification in URu_2Si_2". In: *Phys. Rev. B* 82 (20 Nov. 2010), p. 205108.

[65] M. M. Altarawneh, N. Harrison, S. E. Sebastian, L. Balicas, P. H. Tobash, J. D. Thompson, F. Ronning, and E. D. Bauer. "Sequential Spin Polarization of the Fermi Surface Pockets in URu_2Si_2 and Its Implications for the Hidden Order". In: *Phys. Rev. Lett.* 106 (14 Apr. 2011), p. 146403.

[66] Georgi L. Dakovski, Yinwan Li, Steve M. Gilbertson, George Rodriguez, Alexander V. Balatsky, Jian-Xin Zhu, Krzysztof Gofryk, Eric D. Bauer, Paul H. Tobash, Antoinette Taylor, John L. Sarrao, Peter M. Oppeneer, Peter S. Riseborough, John A. Mydosh, and Tomasz Durakiewicz. "Anomalous femtosecond quasiparticle dynamics of hidden order state in URu_2Si_2". In: *Phys. Rev. B* 84 (16 Oct. 2011), p. 161103.

[67] T. Durakiewicz. In: *(private communication)* (2011).

[68] J. Levallois, F. Lévy-Bertrand, M. K. Tran, D. Stricker, J. A. Mydosh, Y.-K. Huang, and D. van der Marel. "Hybridization gap and anisotropic far-infrared optical conductivity of URu_2Si_2". In: *Phys. Rev. B* 84 (18 Nov. 2011), p. 184420.

[69] J. A. Mydosh and P. M. Oppeneer. "*Colloquium*: Hidden order, superconductivity, and magnetism: The unsolved case of URu_2Si_2". In: *Rev. Mod. Phys.* 83 (4 Nov. 2011), pp. 1301–1322.

[70] C. Pépin, M. R. Norman, S. Burdin, and A. Ferraz. "Modulated Spin Liquid: A New Paradigm for URu_2Si_2". In: *Phys. Rev. Lett.* 106 (10 Mar. 2011), p. 106601.

[71] S. Sachdev. *Quantum Phase Transitions*. Cambridge University Press; 2 edition, 2011.

[72] J.S. Hall, U. Nagel, T. Uleksin, T. Rõõm, T. Williams, G. Luke, and T. Timusk. "Observation of multiple-gap structure in hidden order state of URu_2Si_2 from optical conductivity". In: *Phys. Rev. B* 86 (3 July 2012), p. 035132.

[73] U. Nagel, T. Uleksin, T. Rööm, R. P. S. M. Lobo, P. Lejay, C. C. Homes, J. Hall, A. W. Kinross, S. Purdy, T.J. Williams, G.M. Luke, and T. Timusk. "Optical spectroscopy shows that the normal state of URu_2Si_2 is an anomalous Fermi liquid". In: *PNAS* 109 (47 2012), pp. 19161–19165.

[74] R. Yoshida, M. Fukui, Y. Haga, E. Yamamoto, Y. Onuki, M. Okawa, W. Malaeb, S. Shin, Y. Muraoka, and T. Yokoya. "Observation of two fine structures related to the hidden order in the spectral functions of URu_2Si_2". In: *Phys. Rev. B* 85 (24 June 2012), p. 241102.

[75] C. Bareille. *Effets d'une brisure de symétrie sur les structures électroniques d'URu_2Si_2 et de $KTaO_3$ (PhD Thesis)*. 2013.

[76] C. Bareille, F. L. Boariu, H. Schwab, A. Nuber, P. Lejay, T. Durakiewicz, F. Reinert, and A. F. Santander-Syro. "Gaps, symmetries and entropy loss in URu_2Si_2". In: *(submitted)* (2013).

[77] F. L. Boariu, C. Bareille, H. Schwab, A. Nuber, P. Lejay, T. Durakiewicz, F. Reinert, and A. F. Santander-Syro. "Momentum-Resolved Evolution of the Kondo Lattice into "Hidden Order" in URu_2Si_2". In: *Phys. Rev. Lett.* 110 (15 Apr. 2013), p. 156404.

[78] P. Chandra, P. Coleman, and R. Flint. "Hastatic order in the heavy-fermion compound URu_2Si_2". In: *Nature* 493 (7434 2013), pp. 621–626.

[79] S. Chatterjee, J. Trinckauf, T. Hänke, D. E. Shai, J.W. Harter, T. J. Williams, G. M. Luke, K. M. Shen, and J. Geck. "Formation of the Coherent Heavy Fermion Liquid at the Hidden Order Transition in URu_2Si_2". In: *Phys. Rev. Lett.* 110 (18 2013), p. 186401.

[80] P. Coleman. *The evolving monogram on Many-Body Physics (evolving version).* http://www.physics.rutgers.edu/ coleman/, 2013.

[81] J.-Q. Meng, P. M. Oppeneer, J. A. Mydosh, P. S. Riseborough, K. Gofryk, J. J. Joyce, E. D. Bauer, Y. Li, and T. Durakiewicz. "Imaging the Three-Dimensional Fermi-Surface Pairing near the Hidden-Order Transition in URu_2Si_2 Using Angle-Resolved Photoemission Spectroscopy". In: *Phys. Rev. Lett.* 111 (12 2013), p. 127002.

[82] R. Yoshida, K. Tsubota, T. Ishiga, M. Sunagawa, J. Sonoyama, D. Aoki, J. Flouquet, T. Wakita, Y. Muraoka, and T. Yokoya. "Translational Symmetry Breaking and Gapping of Heavy-Quasiparticle Pocket in URu_2Si_2". In: *Sci. Rep.* 3 (2013).

[83] F. L. Boariu, C. Bareille, F. Reinert, P. Lejay, and A.F. Santender-Syro. "The Heat-Up state of URu_2Si_2 (working title)". In: *(in preparation)* (2014).

Zusammenfassung

Im Jahre 1985 wurde im Aktinidsystem URu_2Si_2 ein rätselhaftes Phänomen entdeckt. Trotz drei Jahrzehnten intensiver Forschung entzieht es sich noch immer einer adäquaten mikroskopischen Beschreibung, was ihm in der wissenschaflichen Literatur den Namen "*Hidden-Order*" Phasenübergang beschert.

Messungen zur spezifischen Wärme, elektrischen Widerstand und Hall Effekt zeigen, dass sich unterhalb einer Temperatur von $T_{\mathrm{HO}} = 17.5$ K eine Energielücke im Bereich von 11 meV über 40% der Fermi Fläche des Festkörpers erstreckt. Experimentelle Daten aus inelastischer Neutronenstreuung weisen an kommensuraten und inkommensuraten Gitterpunkten magnetische Anregungen nach, die unterhalb der Sprungtemperatur ebenfalls Lücken im meV-Bereich aufweisen. Das antiferromagnetische Moment des Festkörpers wird jedoch als zu klein angegeben, um für den gemessenen Verlust an Entropie verantwortlich sein zu können. Versuche den Phasenübergang als konventionelle Ladungs- oder Spindichtewellen zu beschreiben sind fehlgeschlagen. Die Frage, ob eher die lokalisierten oder doch die itineranten Eigenschaften der $5f$ Elektronen des Urans für den Phasenübergang verantworlich sind, wurde im Jahre 2008 durch die Kooperationsgruppe aus Paris / Würzburg zum ersten mal geklärt. Es gelang die Rekonstruktion der Fermi Fläche nahe am Hochsymmetriepunkt Γ durch schwere, kohärente Quasiteilchen durch hochaufgelöste, winkelabhängige Photoemissionspektroskopie zu dokumentieren.

Neuere theoretische Arbeiten suchen die Ursache für den HO-Übergang in der Kohärenz des Gitters, welche aus elektrischen Transportexperimenten bei einer Temperatur von etwa $T \approx 75$ K abgeleitet wird. Trotz der Kohärenztemperatur weit oberhalb von T_{HO} wurden Daten von Infrarotabsorption dahingehend interpretiert, den Phasenübergang bei 17.5 K als den eigentlichen Zeitpunkt der Gitterkohärenz darzustellen. Die "Hidden-Order" wurde in manchen neueren theoretischen Arbeiten als eine Art "verzögerter" Kondo Effekt betrachtet.

In dieser Arbeit wird mit Hilfe von winkelaufgelöster Photoemissionspektroskopie gezeigt, dass das Gitter tatsächlich bereits bei Temperaturen um 70 K kohärent ist. Weitere schwere Quasiteilchen, die bereits weit oberhalb der Sprungtemperatur existieren und von bisherigen Experimenten übersehen wurden, hybridisieren mit Elektronenbändern. Sie spielen somit eine essentielle Rolle in der Reorganisation der Fermi Fläche bei 17.5 K. Die Ergebnisse diese Arbeit bilden die Grundlage für ein ganzheitliches Verständnis der Energielücken, Symmetrien und Entropieverlust beim HO-Phasenübergang. Dieser Zusammenhang wird in einer anderen, mit dieser Arbeit verwandten Dissertation im Detail dargelegt. In den letzten Kapiteln dieser Arbeit wird dies ebefalls kurz umrissen.

Danksagung

Das Projekt, aus welchem diese Dissertation entstanden ist, wurde von Prof. Dr. Andres Felipe Santander-Syro, von der Université Paris-Sud im Jahre 2007 ins Leben gerufen. Die Beteiligung von schweren Quasiteilchen im HO-Phasenübergang war zu diesem Zeitpunkt noch nicht bestätigt. Prof. Dr. Friedrich Reinert von der Universität Würzburg konnte eines der wenigen ARPES Systeme weltweit zur Verfügung stellen, das in der Lage war, die geforderten Temperatur- und Auflösungskriterien zur Untersuchung der HO-Phase zu erfüllen. Die entstehende Kooperation führte zunächst in 2007–2008 zu Teilen der Dissertation von Dr. Markus Klein und zu meiner Diplomarbeit (beide unter der Betreuung von Prof. Dr. F. Reinert), in 2008–2009, zu der Masterarbeit von Cedric Bareille (betreut von Prof. Dr. Santander-Syro), und später zu den beiden Promotionsarbeiten von Cerdic Bareille und mir.

In diesem Zusammenhang möchte ich von ganzem Herzen folgenden Personen meinen Dank zum Ausdruck bringen: meinem Doktorvater und formalen Betreuer dieser Arbeit, Herrn Prof. Dr. Friedrich Reinert; dem "Vater" dieses Projekts und (nicht-formalem) Betreuer, Herrn Prof. Dr. Andres Santander; meinem Freund und weiterem Doktoranden auf der Pariser seite des Projekts, Herrn Cedric Bareille; dem Hersteller der Samples, Herrn Dr. Pascal Lejay; meiner Freundin Anna Reis und meiner Familie Anca, Maria und Stelian für die moralische Unterstützung und Korrekturlesen; meinen Kollegen Holger Schwab, Dr. Andreas Nuber, Dr. Markus Klein, Dr. Frank Forster und Dr. Chul-Hee Min, die direkt in diesem Projekt involviert sind, und an Experimenten, Datenanlysen oder Publikationen mitgewirkt haben und durch Diskussionen oder Korrekturlesen wertvolle Beiträge zu dieser Arbeit geleistet haben; den zahlreichen Kollegen, die zwar nicht direkt mitgewirkt haben, ohne denen jedoch die sowohl technische als auch moralische Infrastruktur, als wichtige Voraussetzung für die Arbeit, nicht gegeben gewesen wäre; Wissenschafltern, die durch Diskussionen, Hinweise und Tips unschätzbare Beiträge geleistet haben, z.B. Prof. Dr. Piers Coleman, Dr. Thomasz Durakiewicz, Prof. Dr. Premala Chandra und andere.

Über die moralische und fachliche Unterstützung hinaus, bedanke ich mich ebenfalls bei meiner Freundin Anna, sowie meiner Familie, für die nötige finanzielle Unterstützung nach der formalen Beendigung meines Beschäftigungsverhältnisses mit der Universität Würzburg in Juli 2012. Herrn Dr. Thomas Schmidt danke ich für seine Erlaubnis, die Infrastruktur (Büro, Drucker, Internetanschluss) seiner Arbeitsgruppe für die Dauer der Arbeit nutzen zu dürfen. Bei seinen Mitarbeitern bedanke ich mich für die sonstige Unterstützung, insbesondere bei Marcel Springer für mehr als nur den Kaffee.